ADVANCED CHARACTERIZATIONS OF AUSTENITIC OXIDE DISPERSION-STRENGTHENED (ODS) STEELS FOR HIGH-TEMPERATURE REACTOR APPLICATIONS

BY

YINBIN MIAO

DISSERTATION

Submitted in partial fulfillment of the requirements
for the degree of Doctor of Philosophy in Nuclear, Plasma and Radiological Engineering
in the Graduate College of the
University of Illinois at Urbana-Champaign, 2015

Urbana, Illinois

Doctoral Committee:

Professor James F. Stubbins, Chair
Professor Brent J. Heuser
Professor Rizwan Uddin
Professor Pascal Bellon

ABSTRACT

Future advanced nuclear systems involve higher operation temperatures, intenser neutron flux, and more aggressive coolants, calling for structural materials with excellent performances in multiple aspects. Embedded with densely and dispersedly distributed oxide nanoparticles that are capable of not only pinning dislocations but also trapping radiation-induced defects, oxide dispersion-strengthened (ODS) steels provide excellence in mechanical strength, creep resistance, and radiation tolerance. In order to develop ODS steels with qualifications required by advanced nuclear applications, it is important to understand the fundamental mechanisms of the enhancement of ODS steels in mechanical properties. In this dissertation, a series of austenitic ODS stainless steels were investigated by coordinated state-of-the-art techniques. A series of different precipitate phases, including multiple Y-Ti-O, Y-Al-O, and Y-Ti-Hf-O complex oxides, were observed to form during mechanical alloying. Small precipitates are likely to have coherent or cubic-on-cubic orientation relationships with the matrix, allowing the dislocation to shear through. The Orowan looping mechanism is the dominant particle-dislocation interaction mode as the temperature is low, whereas the shearing mechanism and the Hirsch mechanism are also observed. Interactions between the particles and the dislocations result in the load-partitioning phenomenon. Smaller particles were found to have the stronger loading-partitioning effect. More importantly, the load-partitioning of large size particles are marginal at elevated temperatures, while the small size particles remain sustaining higher load, explaining the excellent high temperature mechanical performance of ODS steels.

To my parents and my wife, for their love and support.

ACKNOWLEDGMENTS

The completion of this thesis work would be impossible without support and help from many people.

I would like to give special thanks to my advisor, Prof. James F. Stubbins, for his guidance, support and willingness to help at all times.

I would like to thank Dr. Yun Di at Argonne National Laboratory for his introduction of nuclear material field and his reference to join Dr. Stubbins's research group.

I would like to thank Dr. Kun Mo at Argonne National Laboratory for frequently enlightening discussion on the research projects.

I would like to thank Dr. Wei-Ying Chen and Dr. Bei Ye at Argonne National Laboratory for their patient instruction and demonstration when I was learning TEM operation and sample preparation.

I would like to thank Prof. Ian M. Robertson at University of Wisconsin-Madison, Prof. Bai Cui at University of Nebraska-Loncoln, and Dr. Marquis A. Kirk at Argonne National Laboratory for their generous help in the *in-situ* TEM deformation investigations.

I would like to thank Prof. Zhangjian Zhou and his research group at University of Science and Technology Beijing, and Prof. Somei Ohnuki and his research group at Hokkaido University for their generousness in providing austenite ODS steels of excellent quality.

I would like to thank Dr. Michael K. Miller at Oak Ridge National Laboratory for his support in atom probe tomography investigations through CNMS project.

I would like to thank Dr. Jonathan Almer and Dr. Jun-Sang Park for their

support in synchrotron WAXS/SAXS investigations at Advanced Photon Source.

I would like to thank my colleagues, Dr. Xiang Chen, Dr. Hsiao-Ming Tung, Carolyn Tomchik, Aaron Oaks, Kuan-Che Lan, Xiang Liu, and Guangming Zhang for their assistance in experiments, contribution of ideas and many enlightening discussions about this work.

I would also like to thank Prof. Brent Heuser, Prof. Rizwan Uddin, and Prof. Pascal Bellon for their kindness and patience in serving on my defense committee.

Specially, I would like to thank my wife, Dr. Na Zhang, for her continuous support.

This work was supported by 973 DOE INL 120293. The TEM experiments were carried out in part at the Frederick Seitz Materials Research Laboratory Central Facilities, University of Illinois, which is partially supported by the U.S. Department of Energy under grants DEFG02-07ER46453 and DE-FG02-07ER46471. The ANL IVEM/Tandem work was supported by the ANL Center for Electron Microscopy under DE-AC02-06CH11357. Atom probe tomography (APT) was conducted at the Center for Nanophase Materials Sciences, which is a DOE Office of Science User Facility.

TABLE OF CONTENTS

LIST OF TABLES

LIST OF FIGURES

CHAPTER 1

INTRODUCTION

Having a series of excellent properties, the oxide dispersion-strengthened (ODS) steels provide promising solutions for the challenges of structural materials in nuclear energy, especially the development of future advanced nuclear fission and even fusion reactors. The excellence of ODS steels originates from the dense and dispersed oxide nanoparticles that form during the mechanical alloying and following heat treatment/thermal precessing procedures. Therefore, understanding the elemental composition and morphology of these nanoparticles, their interaction mechanism with dislocations, and their contributions to strengthening the materials is crucial for the development of ODS steels that can eventually be applied in future nuclear facilities. Hence, a comprehensive combination of advanced characterization techniques were adopted to explore the properties of the oxide nanoparticles, reveal the nanoparticle-dislocation interactions, and examine the load-partitioning phenomenon as well as the strengthening mechanisms.

1.1 Structural Material Challenges in Nuclear Energy

To maintain the continuous growth and development of world economy, stable, sustainable and practical supplies of energy are crucial. Nuclear fission energy, since it was initiated by Dr. Enrico Fermi's pioneering innovation, has become an indispensable source of clean and affordable energy. Nowadays, nuclear power accounts for around 13% of the world electric energy generation[1]. As of 2015, there were 439 nuclear fission reactors distributed in 31 countries in operation around the world[2]. In the United States, 100 commercial nuclear reactors, including 65 pressured water reactors (PWRs)

and 35 boiling water reactors (BWRs), contributes to 19.4 % of the countries' electric energy generation[3]. Different from the fossil energy, nuclear power generates little carbon dioxide, and therefore is regarded as an important energy source to reduce the carbon emission and relieve the global warming.

The high power density feature of nuclear power inevitably results in the harsh environment within the nuclear reactors. Actually, the internal environment of a nuclear reactor are a complex coordination of various extreme conditions including elevated temperature, high pressure, intense neutron irradiation, and corrosive coolant. As a result, structural materials of nuclear reactors are supposed to adapt the harsh environment described before for practical and affordable industry applications (see Figs. 1.1 and 1.2 for the major materials elected to be used in PWRs and BWRs[4]). Exceptional properties in various aspects are required by the structural materials qualified for practical nuclear applications, including mechanical strength, mechanical toughness, creep resistance, thermal stability, corrosion resistance, and radiation tolerance.

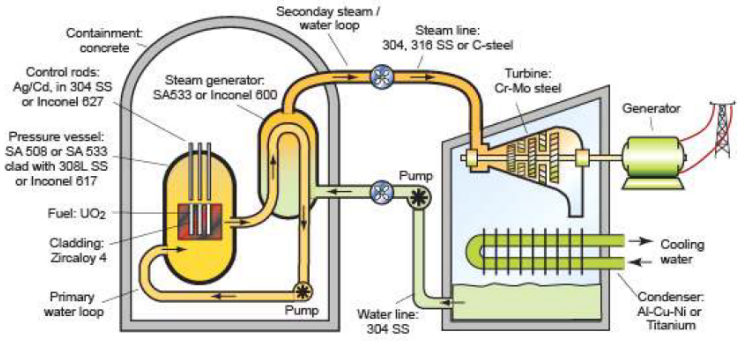

Figure 1.1: Major Materials Used in Pressured Water Reactors[4]

Recent efforts in nuclear engineering to enhance the accident tolerance of current reactors[5, 6], to extend the operation lifetime of existing commercial nuclear power plant[7], and to develop Generation IV nuclear reactors which are equipped with a variety of advanced concepts, make the selection of structural materials even more challenging[1]. For over a decade, concepts of Generation IV nuclear reactors have been comprehensively discussed[8, 9]. Six concepts that were finally selected include three thermal reactor concepts: the very high temperature reactor (VHTR), the molten-salt reactor (MSR),

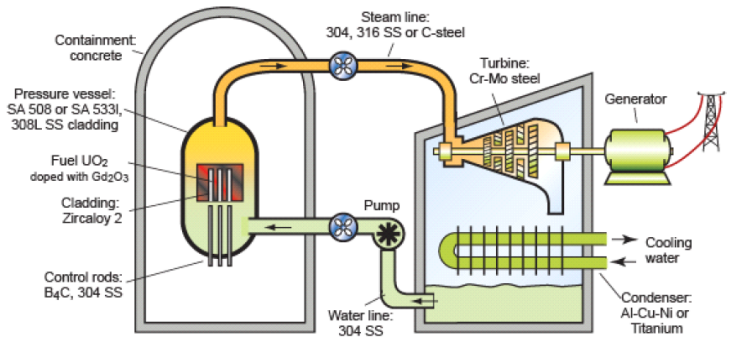

Figure 1.2: Major Materials Used in Boiling Water Reactors[4]

and the supercritical-water-cooled reactor (SWCR), and three fast reactor concepts: the gas-cooled fast reactor (GFR), the sodium-cooled fast reactor (SFR), and the lead-cooled fast reactor (LFR). For all those six advanced concepts mentioned previously, the structural materials are supposed to be exposed to higher operation temperatures, more aggressive coolants, and severer irradiation doses (see Fig. 1.3), increasing the challenges for the structural materials to overcome.

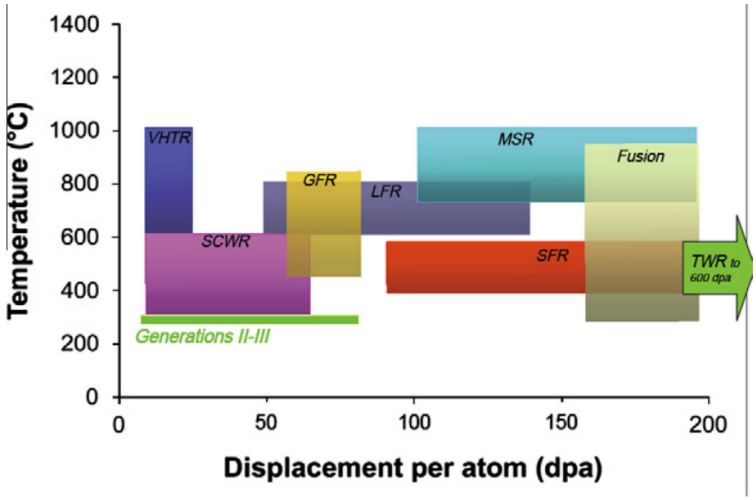

Figure 1.3: Temperature and Dose Requirements for In-core Structural Materials for Generation IV Reactor Concepts[1]

In order to find structural materials with promising qualification and therefore to realize those six innovative concepts of Generation IV reactors, a series of advanced materials have been developed and evaluated for their performance in reactor environments. Those efforts can be categorized into two

groups. One is based on the the existing materials and precessing procedures, only including the composition/processing optimization or surface treatment. This type of efforts include the reduced activation ferritic/martensitic steels (RAFM) and thermo-mechanical treated(TMT) alloys[10, 11]. The other, however, is dependent on the novel techniques that have never been applied in nuclear industry before. Examples of this type of effort are oxide dispersion-strengthened (ODS) alloys[12, 13] and nickel-based superalloys[14, 15, 16, 17]. Although ODS steels are new for the nuclear energy industry and therefore require careful examination for their qualification, the significant advantages coupled with this technique making them promising candidates for the structural materials applied in Generation IV reactors.

1.2 Oxide Dispersion-Strengthened Alloys

Precipitate-strengthening mechanism has been utilized by human beings to enhance the mechanical properties of metals and alloys for millenniums. A wide range of precipitates have been selected to strengthen the matrix, including carbides ($M_{23}C_6$, M_7C_3, MC_6, MC, e.g.)[18, 19, 20], nitrides (MN)[13, 21], intermetallics (Ni_3Al, $Zr(Fe,Cr)_2$, e.g.)[22], and refractory metals (W, e.g.)[23]. However, precipitates within conventional alloys still have significant size, which limits their contributions to the enhancement of the mechanical strength. Meanwhile, those precipitates are usually unstable under high temperature or high irradiation conditions, resulting in the degradation of performance as applied in nuclear reactors. Therefore, the advanced development of precipitate-strengthened steels calls for ultra-fine precipitates that have excellent thermal stability and radiation tolerances.

Mechanically alloying of steel and oxide powders along with the following thermal processing and heat treatment introduces a dense distribution of nano-scale oxygen-enriched particles that are resistant to coarsening at elevated temperatures[24] and high irradiation conditions[25] into the steel matrices and therefore produces the oxide dispersion-strengthened (ODS) steels. The size of these oxygen-enriched nanoparticles is around 10 nm and sometimes can be smaller than 3 nm as the manufacture conditions are well-designed and precisely-controlled. Those ultra-fine dispersed precipitates are

capable of effectively pinning the dislocations during plastic deformation or dislocation creep procedures. As a result, ODS steels hold outstanding mechanical strength and creep resistance compared to conventional steels[26]. More importantly, the existence of those densely and dispersedly distributed nanoparticles creates a great number of extra interfaces within the materials. Since those extra interfaces can act as sinks of the point defects generated by neutrons or secondary ions, and helium atoms produced by (n, α) reactions, the nanoparticle-matrix interfaces provide huge amounts of annihilation centers for irradiation-induced defects as well as nucleation centers for helium bubbles[27, 28, 29, 30]. Consequently, ODS steels are supposed to have better radiation tolerance, especially swelling resistance, than those steels without dispersed oxide nanoparticles.

Ferritic or martensitic (F/M) stainless steels intrinsically have outstanding mechanical strength and swelling resistance, and their performance has been validated by the successful applications as in-core and out-of-core structural materials of current commercial nuclear reactors. Based on these advantages, F/M ODS steels are regarded as competitive candidates for the structural materials in future advanced nuclear reactor designs[31]. ODS alloys was first innovated in 1960s by NASA for aerospace applications[32]. However, they were not considered for nuclear applications until 30 years later. In early 1990s, the excellent creep resistance of F/M ODS steels started to catch the attentions from the nuclear industry. The early F/M ODS steels were expected to replace the austenitic steels such as PNC316 and PNC1520 as structural materials for high-dose applications in nuclear reactors[33]. Actually, F/M ODS steels have always been the concentration of ODS steel studies. However, F/M phase of iron-based alloys usually has poor creep resistance compared to austenitic phase. In addition, as F/M is only a low-temperature stable phase, its stability at high temperature is problematic. More importantly, F/M steels suffer with corrosion, especially when the Cr content is low. Higher Cr content (7w% to 12w%) tends to improve this disadvantage in corrosion resistance, but carries with $\alpha - \alpha'$ phase separation, which significantly degrades the mechanical properties (especially the ductile-brittle transition temperature, DBTT), after thermal aging or irradiation[34].

Austenitic phase is a high-temperature stable phase of Fe-Cr alloys. However, addition of nickel can prominently lower the temperature of phase tran-

sition. In fact, sufficient nickel content is capable of making austenitic phase stable or metastable at ambient temperature[35]. The Fe-Cr-Ni austenitic stainless steels have properties that are quite different from those of F/M steels[36]. Austenitic steels usually have superior creep performance and corrosion resistance, making them competitive as structural materials of nuclear reactors. In fact, because of these advantages mentioned above, austenitic stainless steels has been employed as the pressure vessel cladding and core structures in current commercial reactors[1]. Unfortunately, austenitic steels have relatively low mechanical strength and severe radiation swelling compared to F/M steels. In particular, the austenitic phase stabilizer Ni has a high (n, α) cross section, contributing a lot to the growth of helium bubbles. All of these limit their applications in nuclear industry. As mentioned previously, the introduction of dense and dispersed ultra-fine oxygen-enriched nanoparticles are able to enhance the mechanical strength as well as radiation tolerance with maintenance in the intrinsic advantages of austenitic steels in creep and corrosion performance . Therefore, austenitic ODS stainless steels are a group of competitive candidates for the selection of structural materials of advanced nuclear reactors[26, 37, 38, 39, 40, 41].

1.3 Formation, Composition, and Crystallography of Oxide Nanoparticles

The fundamental mechanism that explains the formation procedures of the densely and dispersed distribution of ultra-fine oxygen-enriched nanoparticles within ODS steels is the origin to improve the morphology of the precipitates within steel matrices, and thus perfect the performance of ODS steels so that they can finally be deployed into the design of future nuclear power systems.

The formation procedure of those ultra-fine oxygen-enriched nanoparticles are still unclear in spite of the continuous efforts that have been made to reveal it. The ball milling of alloy powders or mixture of elemental metal powders with oxide powders, such as Y_2O_3, is the initial step of mechanical alloying. X-ray and electron diffraction results of the powders that have been ball milled for different periods of time show that the crystalline Y_2O_3 grad-

ually disappears during the ball milling. After consolidation and following heat treatment, the fine oxygen-enriched precipitates form[42, 43, 44, 45, 46]. The newly precipitated particles are no longer simply Y_2O_3, but complex oxide phases. For instance, in the absence of Al, Y-Ti-O oxides such as pyrochlore $Y_2Ti_2O_7$ and orthorhombic Y_2TiO_5 are the most commonly reported phases[13]. While Al is present, Y-Al-O oxides, including yttrium aluminum garnet (YAG), yttrium aluminum monoclinic (YAM), and yttrium aluminum perovskite (YAP) are found precipitating in the steel matrices[47]. The addition of Group IV elements, such as Ti, Zr, and Hf, proved to help reduce the precipitate size and therefore achieve the dispersive distribution[48]. When more complex recipes are employed in the ball milling procedure, other elements such as chromium[49] are also likely to be enriched during the precipitation of the oxygen-enriched nanoparticles.

Two hypotheses were established to explain the formation of these oxide nanoparticles. In the first theory, the Y_2O_3 powders are thought to dissemble during ball milling and then form nano-scale amorphous regions that are dispersedly distributed within the steel matrices. Meanwhile, the other metal elements of high affinity for oxygen, such as Ti and Al, diffuse into these amorphous regions. After consolidation and annealing, those amorphous regions with adequate size have sufficient thermal energy to recrystallize and then form the oxide nanoparticles, whereas those very small amorphous regions remain uncrystallized as entropy is dominant. In addition, those amorphous regions with significant size form core/shell structures during crystallization due to the off-stoichiometry effect. A schematic illustration showing this mechanism can be found in Figure 1.4[42].

The second theory includes more complex procedures. Both the yttrium and oxygen atoms dissolve into the matrix during the ball milling. Due to the existence of dissolved oxygen atoms inside the steel system, oxygen-vacancy couples, which have lower energy compared with separate oxygen interstitials and metal vacancies, are formed. As these oxygen-vacancy couples can combine with those metal atoms of high affinity for oxygen, such as Y, Al, and Ti, to further lower the energy, the oxide nanoparticles are hence nucleated during annealing. In this theory, even the size of the nanoparticle is controlled by the thermodynamics and can be predicted[50].

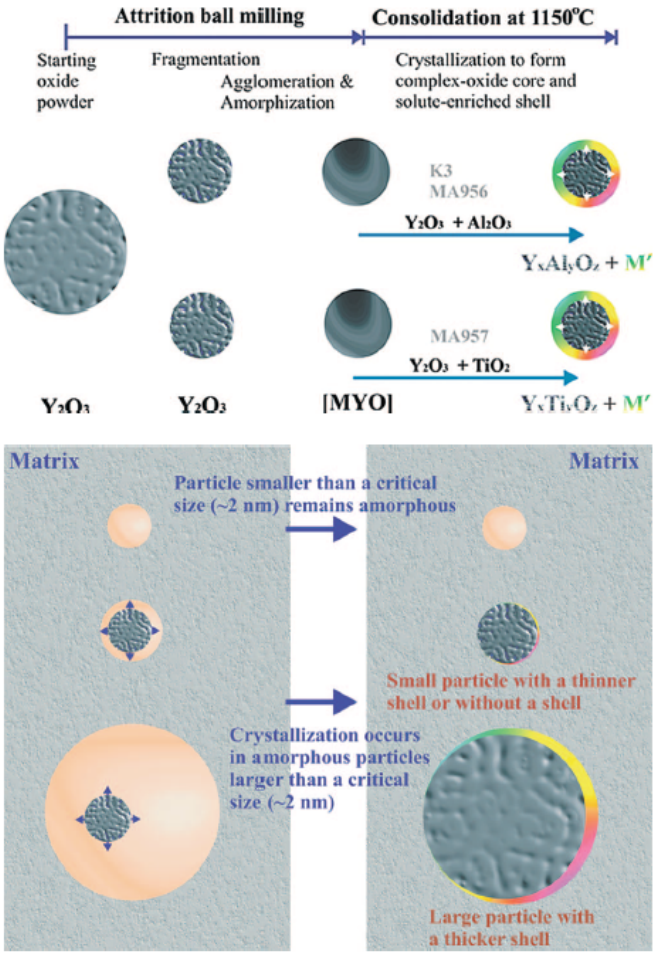

Figure 1.4: Nanoparticle Formation Mechanism I[42].

1.4 Orientation Relationship

The extra interfaces provided by the dense and dispersed ultra-fine nanoparticles are the origin of the excellence of ODS steels. The properties of these interfaces not only influence the strain field due to the nanoparticles and then the sink strength for the point defects and helium atoms[51, 52], but also affect the particle-dislocation interaction mechanism during plastic deformation and dislocation creep[53]. When two crystalline phases are divided by an interfaces, the most important property of the interface is the orientation relationship. The orientation relationship describes how the atomic lattice in one phase evolves into another phase.

As no atomic planes in one phase are parallel to any atomic planes in the other phase, the orientation relationship of the interface is incoherent. In that case, the interface includes great difference in atomic configurations, whereas the strain field due to the interface is week. On the other hand, if a certain atomic plane in one phase is parallel to an atomic plane in another phase, the difference between the spacings of these two planes is a relevant quantity influencing the properties of the interfaces. This difference can be measured by misfit, Δ, with the definition as follows:

$$\Delta = \frac{d_\alpha - d_\beta}{d_\alpha}, \tag{1.1}$$

where d_α and d_β are the d-spacings of the specific atomic planes in phases α and β, respectively. The accumulation of the misfit in space results in the formation of misfit dislocations to release the strain energy. In fact, the reciprocal number of misfit indicates the spatial frequency that a misfit dislocation can be observed. As the misfit is small ($\Delta < 0.04$), the misfit dislocations are sparse on the interface (<1 dislocation per 25 atomic layers). In that case, the criteria of coherent orientation relationship is satisfied (see Fig. 1.5). As the misfit is intermediate ($0.04 < \Delta < 0.25$), there exist dense distribution of misfit dislocations. Therefore, the orientation relationship is categorized as semi-coherent according to these dislocations (see Fig. 1.6). When the misfit exceeds 0.25, namely, more than 1 misfit dislocation can be found for each successive 4 atomic layers, the high dislocation density disqualify this orientation relationship for coherent or semi-coherent orientation

relationship. As a result, this situation has to be categorized as incoherent relationship in spite of the existence of parallel atomic planes[54].

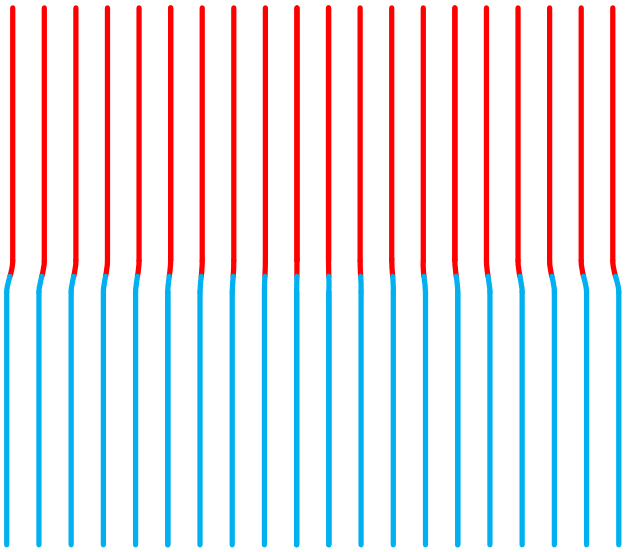

Figure 1.5: Coherent Orientation Relationship: Δ=0.02, few dislocations on the interface.

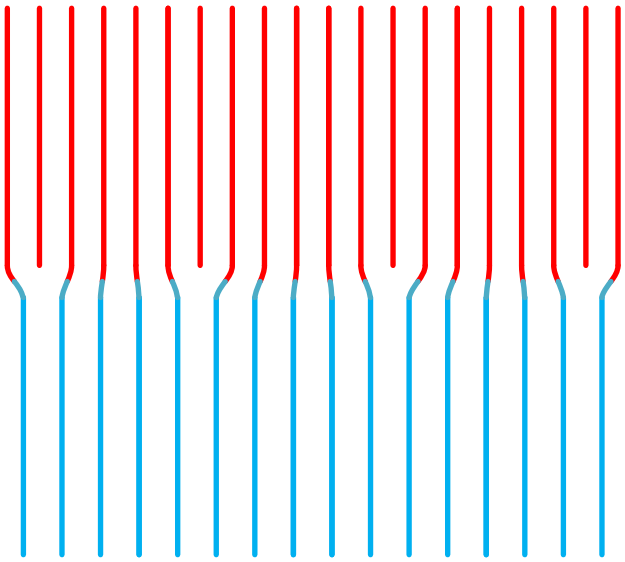

Figure 1.6: Semi-coherent Orientation Relationship: Δ=0.2, dense misfit dislocations on the interface.

When the both phases involved have cubic structures, a special orientation relationship can be defined. Cubic-on-cubic orientation relationship, as the

name implies, require all the corresponding axes in the two cubic systems to be parallel to each other. Depending on the difference between the lattice constant of the two phases, the cubic-on-cubic relationship is likely to be coherent, semi-coherent, or incoherent.

The orientation relationship of the interface significantly influences the energy of the interface. The interface energy has two different origins: the chemical difference (γ_{ch}) and the structural configuration (γ_{st}). γ_{ch} is mainly dependent on the chemical compositions of the two involved phases, and therefore less related to the orientation relationship. γ_{st} is directly determined by the orientation relationship. To be specific, coherent orientation relationship usually corresponds to near zero γ_{st}, whereas incoherent orientation relationship normally corresponds to significant values of γ_{st}.

1.5 Particle-dislocation Interaction Mechanism

Dislocation movement is the major mechanism of plastic deformation as well as dislocation creep. As a result, any factors that can effectively interfere the dislocation movement, such as grain boundary, solvent impurity, precipitates, and even dislocations themselves, contribute to the enhancement of mechanical strength and creep performance. In ODS steels, ultrafine oxygen-enriched nanoparticles of dense and dispersed distribution were introduced into steel matrices to pin dislocations. Therefore, knowledge of the fundamental mechanism of the interactions between the dislocations and those nanoparticles is crucial in understanding the outstanding mechanical strength and creep performance of ODS steels.

There exist multiple particle-dislocation interaction mechanisms. The most important physical quantity coupled with a particle-dislocation interaction mechanism is the critical resolved shear stress (CRSS), which is the lowest resolved shear stress needed for a dislocation to bypass a particle via a specified interaction mechanism. In fact, as a dislocation meets with a particle standing in its slip plane, the particle-dislocation interaction mechanism that has the lowest CRSS takes place. In another word, the selection of interaction mechanisms is a competition of CRSS.

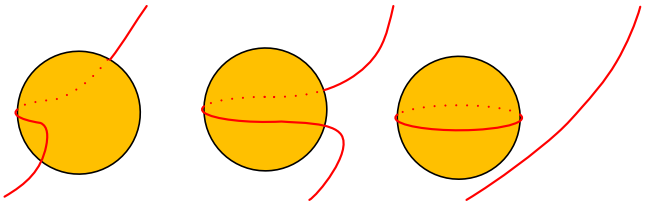

Figure 1.7: The Orowan Looping Mechanism

The most common particle-dislocation interaction mechanism is the Orowan mechanism[55]. In the Orowan mechanism, the dislocation bypasses the particle by leaving a dislocation loop circulating the particle. Therefore, this mechanism is also call the Orowan looping mechanism, as shown in Fig. 1.7. The CRSS of the Orowan mechanism was described by the classic Bacon-Kocks-Scattergood (BKS) model[56], which has the following expression for an edge dislocation[57]:

$$\tau_{Orowan} = \frac{Gb}{2\pi L}[ln(\frac{dL}{d+L}\frac{1}{b})], \tag{1.2}$$

where, G is the sheer modulus of matrix, b is the dislocation's Burgers vector, d is the diameter of the particle, and L is the spatial separation between the centers of the particles. The equation for a screw dislocation only differs from Equation 1.2 by a constant factor.

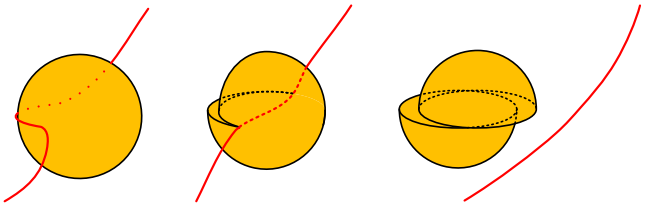

Figure 1.8: The Shearing Mechanism

Another particle-dislocation interaction mechanism involves a dislocation cutting through a "soft" particle. In this case, the orientation of the particle is required to be parallel to the matrix so that the dislocation can slip through. Due to the nature of dislocations, the particle is sheared by a length of the Burgers vector once a dislocation cuts through. Therefore, this interaction mechanism is referred to as the shearing mechanism (see Fig. 1.8). The CRSS of the shearing mechanism, unlike that of the Orowan looping

mechanism, is dependent not only on the properties of the matrix, but also on the properties of the precipitate phase. The analytic expression of the CRSS of shearing mechanism is therefore complex, and has the following form for FCC materials[57]:

$$\tau_{shearing} = \frac{\sigma_m}{2L\delta}B, \tag{1.3}$$

where, σ_m is the resolve shear stress for a straight dislocation to penetrate a semi-infinite media of particle phase, $r = d/2$ is the particle radius, L is the spatial separation between the centers of the particles, δ is the distance between two Shockley partials, and B is the area of the particle between two partials as the tailing partial just enters the particle. The dissociation of a perfect dislocation into two Shockley partials is a common phenomenon in FCC materials with low stacking fault energy (SFE), which will be discussed in detail later in this dissertation. When a dislocation interacts with a particle, the particle-dislocation interaction mechanism that has the lowest CRSS occurs. Hence, there is competition between Orowan looping and shearing, the details of which will be analyzed later.

In factor, the Orowan and shearing mechanisms described above, as shown in Figures 1.7 and 1.8, are just the ideal situations that take place as the slip plane of the dislocation is near the center of the particle. When the slip plane of the dislocation is off the center of the particle, according to computer simulation, the Orowan mechanism is likely to end up with the Orowan loop collapsing into two loops, and meanwhile, the shearing mechanism may also involve the formation of a dislocation loop around the particle[58]. These special situations can be thought of as the variants of the Orowan or shearing mechanism.

In addition to these two fundamental mechanisms, a dislocation can also bypass a particle by cross slipping into other planes and leaving prismatic dislocation loops. This phenomenon is called the Hirsch mechanism[59]. Due to the nature of cross slip, the Hirsch mechanism is complicated, and may sometimes mix with Orowan looping to form several variants[60, 61, 62, 63]. Typically, the Hirsch mechanism has a CRSS that is only slightly different from that of Orowan looping[60, 64, 65, 66], complicating the competition between Orowan looping and the Hirsch mechanism.

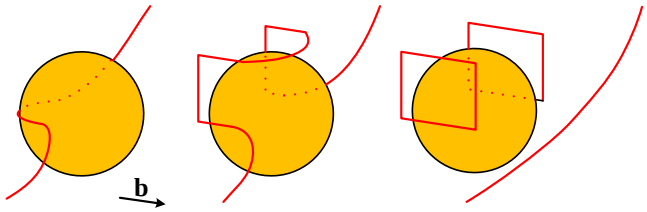

Figure 1.9: The Hirsch Mechanism Involving an Edge Dislocation

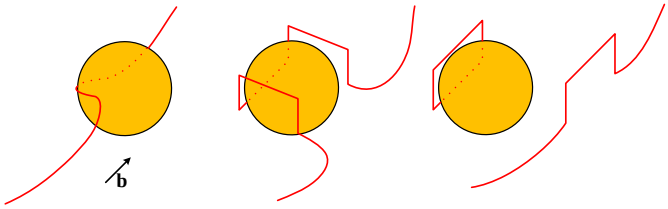

Figure 1.10: The Hirsch Mechanism Involving a Screw Dislocation

At elevated temperatures, the rise of atomic kinetic energy causes a number of complexities in the particle-dislocation mechanisms. First, the high atomic kinetic energy activates the diffusion of point defects, and therefore enables the climb of dislocations. Hence, a dislocation is likely to climb over a particle at high temperature[67]. Second, the repulsive particle-dislocation interaction at ambient temperature transits to the attractive particle-dislocation interaction nature as the temperature is high enough, making the dislocation attached on the departure size of the particle after bypassing[68, 69]. In addition, cross-slip is also prominent as the temperature rises, helping dislocations circumvent the particles. As a result, elevated temperatures complicate the particle-dislocation interactions.

In order to characterize these particle-dislocation interaction mechanisms, it is crucial to investigate the detailed process and microstructure formed during the particle-dislocation interactions. The diffraction contrast image of a transmission electron microscope (TEM) provides a unique method to directly observe dislocations. Precipitate particles, which usually have different diffraction conditions from the matrix, can also be prominent in diffraction contrast if the diffraction condition is reasonably adjusted. In particular, the *in-situ* TEM deformation investigations enables direct observation of the particle-dislocation interactions. Using a TEM stage with tensile function, this technique is capable of providing real-time particle-dislocation interac-

tion information. *In-situ* TEM deformation technique has been adopted to investigate the particle-dislocation interaction mechanisms in intermetallic precipitate strengthened alloys[70, 71, 72]. Although some pioneering *in-situ* TEM deformation efforts, which mainly focused on the Orowan mechanism involving large particles (around 30 nm), have been made to investigate the particle-dislocation interaction in ODS steels[73, 74], no systematic and comprehensive investigations have been accomplished yet to cover a wide range of nanoparticle size and spacing, as well as all the three major interaction mechanisms.

1.6 Load-Partitioning Phenomenon

As mentioned in the previous sections, precipitates within the alloy matrix interact with the dislocations, and therefore suppress dislocation movement, enhancing the mechanical strength as well as creep resistance. During plastic deformation or dislocation creep, dislocations are pinned by those precipitates. As a result, the precipitates take higher stress than the matrix does, which is called the load-partitioning phenomenon. This extra stress borne by precipitates account for the majority of the outstanding mechanical strength of the precipitate-strengthened alloys. Hence, the load-partitioning phenomenon is highly relevant to the efficiency of the precipitates in strengthening the materials. More importantly, measuring the load-partitioning of the precipitates with different properties such as size distribution and spatial density helps reveal how these characteristics influence the precipitate-strengthening effect. For complex advanced alloy systems such as ODS steels, the matrices commonly contain multiple types of precipitates. Consequently, understanding the load-partitioning phenomenon, especially the contribution of each precipitate, is crucial to clarify the origin of the exceptional mechanical strength of ODS steels, and then guide the development of advanced ODS steels that are practical for the applications in prospective nuclear systems.

Due to the limited size and volume fraction, it is challenging to quantitatively measure the extra load taken by the oxygen-enriched nanoparticles in ODS steels. Reflecting the atomic spacing within the crystalline mate-

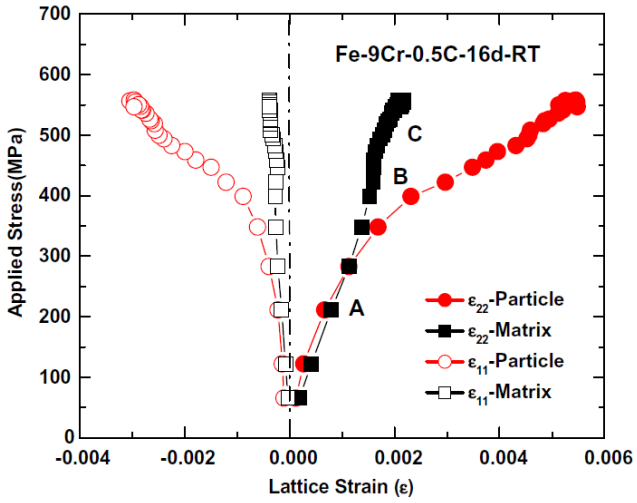

Figure 1.11: Load-Partitioning Phenomenon within a Fe-9Cr-0.1C Model Alloy[18]

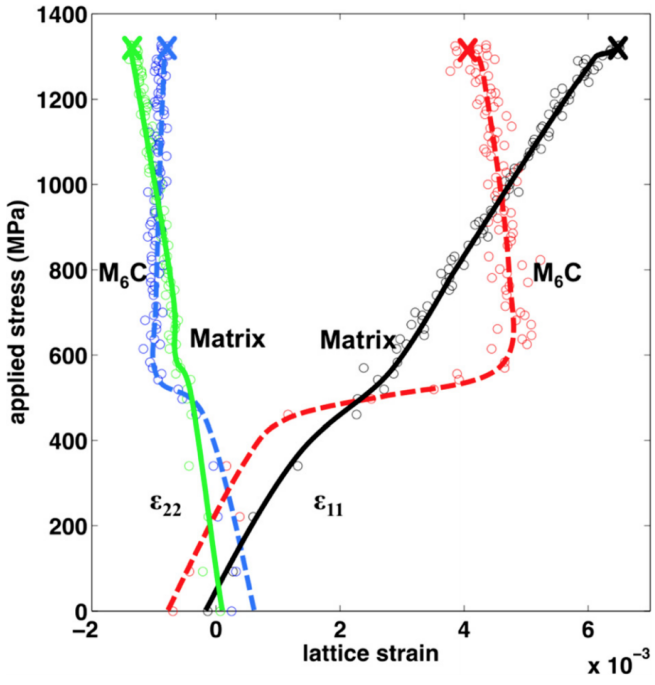

Figure 1.12: Load-Partitioning Phenomenon within Alloy 617 and Alloy 230[20]

rials, diffraction is a technique that is likely to be adopted to monitor the strain evolution of various phases within ODS steels during plastic deformation. However, the energies and intensities of conventional X-ray sources are too low to transmit the tensile specimen and accumulate enough signals on the detector for analyzing the precipitate phases, whereas the electron diffraction in TEM lacks accuracy due to the limitation of electron detector and precise measurement of the external load. Fortunately, synchrotron X-ray source is capable of producing X-ray beams with extremely high energy and intensity, which is sufficient to project distinguishable scattering signals of precipitate phases onto the detector panels. Therefore, with the *in-situ* tensile stage, synchrotron X-ray source is a powerful mean to monitor the dynamic properties of the load-partitioning phenomenon in precipitate-strengthened alloys. In fact, *in-situ* synchrotron tensile investigation has already been employed to explore the load-partitioning phenomenon in a couple of conventional precipitate-strengthened steels (see Figs. 1.11 and 1.12)[18, 19, 75, 76, 20]. For example, Pan et al., found that the $M_{23}C_6$ carbides take more load than the matrix does during the entire plastic deformation, as shown in Figure. 1.11. On the other hand, the load on the M_6C carbides in Ni-based alloys drops in the late stage of plasticity due to the formation of voids and the fracture of carbides as illustrated in Fig. 1.12. Hence, applying the *in-situ* synchrotron tensile investigation to the examination of the load-partitioning phenomenon of austenitic ODS steels is promising, and will undoubtedly expand our understanding on the excellent mechanical properties of ODS steels.

CHAPTER 2

METHODS

This study was focused on the microstructure characterizations on a series of austenitic ODS alloys. The investigated ODS steels were developed by Prof. Somei Ohnuki's research group at Hokkaido University in Japan[39] and Prof. Zhangjian Zhou's research group at University of Science and Technology Beijing in China[26, 77]. A systematic combination of advanced material characterization techniques, including various electron microscopies, atom probe tomography and synchrotron scattering, were utilized to perform a coordinated investigation on the crucial properties of the oxide nanoparticles and their contribution to the enhancement of material performance.

2.1 Investigated Materials

Three different austenitic ODS stainless steels were examined in this study. They were all manufactured by mechanical alloying and following heat treatment and thermal processing procedures. The details of the investigated materials are listed as follows.

2.1.1 Hafnium-containing ODS 316 Steel

The SUS316 stainless steel (see Table 2.1 for composition) was ball milled with 0.35wt% Y_2O_3, 0.1wt% Ti and 0.6wt% Hf for 24 hours. The product was annealed at 1150 °C for 2 hours before hot extrusion, and was finally annealed at 1100 °C for 1 hour. The material was manufactured by Prof. Somei Ohnuki's research group at Hokkaido University[39]. The grain size of the ODS alloy 316 is approximately 0.5 µm, and the oxide particle density is

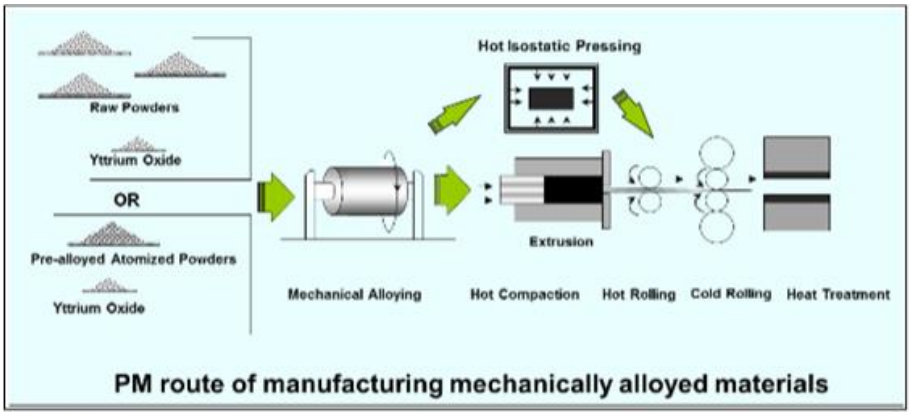

Figure 2.1: Manufacture procedures of ODS steels

6.6×10^{21} m^{-3} with an average size of 9.4 nm according to the manufacturer, as shown in Figure 2.2.

Table 2.1: Chemical composition (wt%) of the Hf-containing ODS 316 investigated in this study

Fe	Cr	Ni	Mo	Mn	Ti	Si	Nb+Ta	C	Y_2O_3
bal.	16.16	13.66	2.33	1.82	0.08	0.75	0.08	0.05	0.35

According to the test results provided by the manufacturer, the 316 stainless steel gains magnificent enhancement in tensile strengths at both room and elevated temperatures after the introduction of dispersed oxide nanoparticles (see Figure 2.3). The oxide nanoparticles, along with the reduced grain size, also help suppress the growth of bubbles under helium ion irradiation compared with ordinary 316 stainless steels, as shown in Figure 2.4[38].

2.1.2 ODS 304 (LN) Steel

The ODS stainless steel 304 (LN) investigated in this study has the composition listed in Table 2.2. The base material powders were mechanically alloyed in an argon atmosphere using a planetary ball mill at 300 rpm with a ball-to-powder ratio of 5:1 for 30 hours. The milled powders were then degassed, sealed, and consolidated by hot isostatic pressing (HIP) under a pressure of 100 MPa at 1100 °C for 2 hours and then at 1150 °C for another one hour. The as-HIPed sample was then forged at 1150°C with a forging ratio of 3:1. Additional hot rolling was performed three times with a reduction

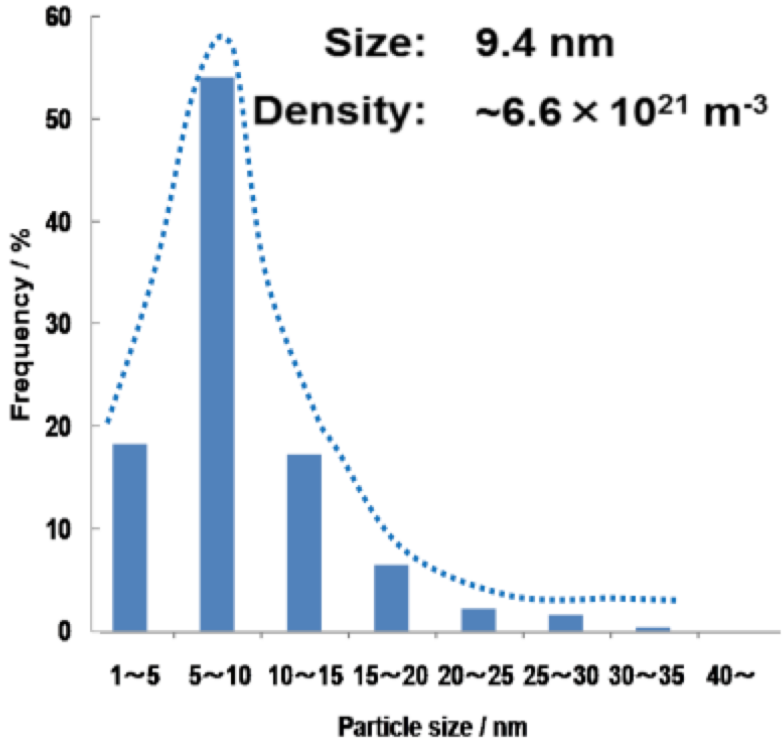

Figure 2.2: Size distribution of the oxide nanoparticles in the hafnium-containing ODS 316 steel

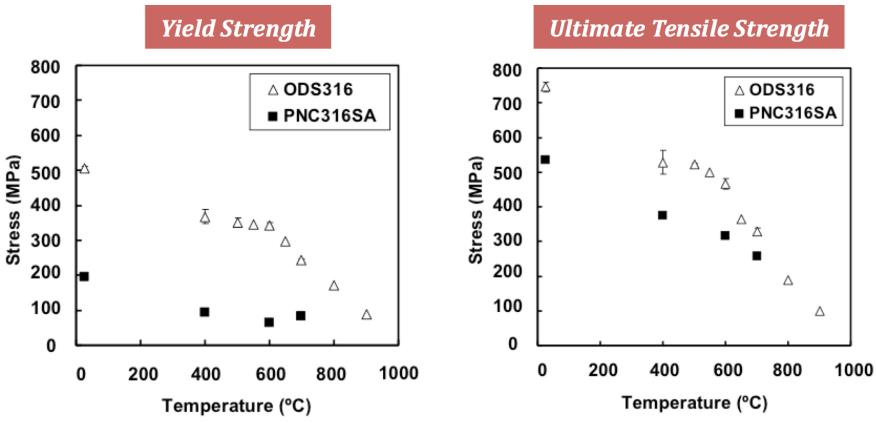

Figure 2.3: Tensile strength of the Hafnium-containing ODS 316 Steel at Various Temperatures

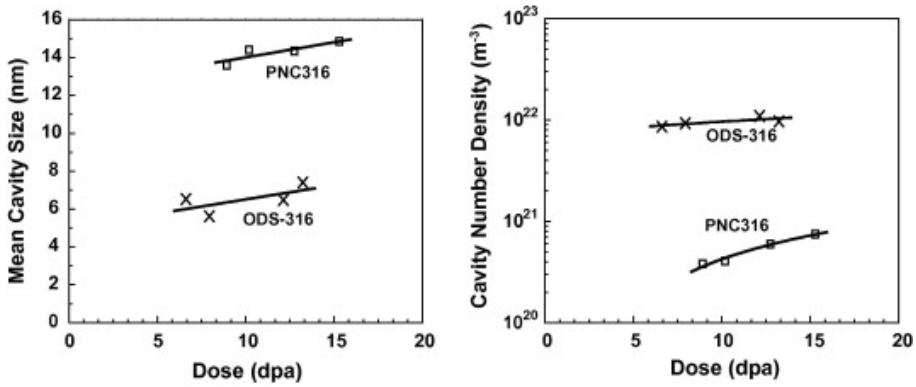

Figure 2.4: Comparison of helium bubble evolution between the Hf-containing ODS 316 steel and oridinary 316 stee[38]

ratio of approximately 20% for each stage. These post-milling heat treatment and processing procedures ensure the great tensile elongation property of the specimen. The material was manufactured by Prof. Zhangjian Zhou's research group at University of Science and Technology Beijing. The manufacturer reported that the ODS 304 steel has an average grain size around 250 nm and a dense distribution of oxide nanoparticles[26].

Table 2.2: Chemical composition (wt%) of the ODS 304 investigated in this study[37]

Fe	Cr	Ni	Mo	Ti	Si	Y_2O_3
bal.	18	8	1	0.5	0.15	0.35

2.1.3 ODS 316 (LN) Steel

The ODS stainless steel 316 (LN) investigated in this study has the composition listed in Table 2.3. The base material powders were mechanically alloyed in an argon atmosphere using a planetary ball mill at 300 rpm with a ball-to-powder ratio of 5:1 for 30 hours. The milled powders were then degassed, sealed, and consolidated by HIP under a pressure of 100 MPa at 1150 °C for 3 hours. The material was manufactured by Prof. Zhangjian Zhou's research group at University of Science and Technology Beijing. The manufacturer reported that the ODS 316 steel has an average grain size around 250 nm and a dense distribution of oxide nanoparticles[77].

Table 2.3: Chemical composition (wt%) of the ODS 316 investigated in this study

Fe	Cr	Ni	Mo	Mn	Si	C	P	S	N	Ti	Y_2O_3
bal.	16.82	13.23	2.48	0.40	0.72	0.008	0.005	0.007	0.2	0.3	0.35

2.2 Transmission Electron Microscopy

2.2.1 Conventional Transmission Electron Microscopy

Transmission electron microscope (TEM) was invented in 1920s to overcome the wavelength limitation of optical microscopes, and was then widely used in the microstructure characterization of materials. Conventional TEM utilizes the wave nature of electrons to image the reciprocal space of the crystal structures of materials, namely, diffraction patterns on the focal plane of the objective lens. For a single crystal region, the multiple scattering of electron form Kikuchi lines on the focal plane of the objective lens, and then can be used as a "map" for the orientation of that single crystal. Using Kikuchi map, the orientation of the single crystal can be carefully tuned to satisfy some specific conditions. For example, as the orientation of the single crystal is adjust to exactly match the Bragg's law:

$$2dsin\theta = n\lambda, \tag{2.1}$$

where, d is the atomic spacing of a specific reflection, θ is the diffraction angle, n is a natural number, and λ is the wavelength of the election; or another equivalent form:

$$\mathbf{k} - \mathbf{k_0} = \mathbf{g} \tag{2.2}$$

where, $\mathbf{k}$ is the wave vector of diffracted electrons, $\mathbf{k_0}$ is the wave vector of incidental electrons, and $\mathbf{g}$ is a lattice vector in the reciprocal space of the atomic lattice, the diffraction condition is called two-beam condition, where the $\mathbf{g}$ diffracted beam and the transmitted beam are the two brightest beam spots. Diffraction contrast images can be formed by choosing transmitted or diffracted spot using the objective aperture. The image generated merely by

the transmitted beam is called bright field (BF) diffraction contrast, whereas the image from the diffracted beam is named dark field (DF) diffraction contrast. Diffraction contrast indicated the microstructural features that involve the diversion of lattice positions, such as dislocations and stacking faults, within the specimens. The two-beam condition usually yields strong diffraction contrast that might not be appropriate to microstructure characterization. Thus, the right hand side (RHS) of Equation 2.2 can be adjusted to multiplicities of **g**, for example, 3**g** and 5**g**. Considering the intrinsic difference of 2**g** between the bright field and dark field diffraction condition, 3**g**-5**g** or 5**g**-7**g** diffraction conditions can be obtained. These diffraction conditions are slightly off the Bragg's law, and provide diffraction contrast weaker than the two-beam condition (also called **g**-3**g**) does. In particular, the dark field images, which only include the information from a single diffraction, can clearly image dislocations and stacking faults as the diffraction condition is weak enough. This is therefore defined as the weak beam dark field (WBDF) image.

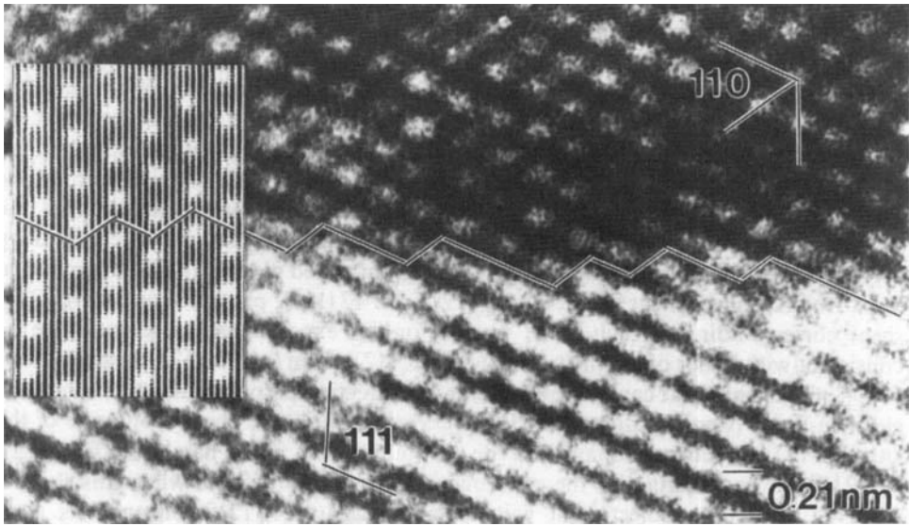

Figure 2.5: An HRTEM image showing the coherent orientation relationship of a martensite-austenite interface[78]

When the objective aperture is absent or sufficiently large, the scattered electrons along with the transmitted ones contribute to form the image of the specimen on the image plane of the objective lens. As image plane is the Fourier transformation of the focal plane, the diffraction spots of crystalline specimens form fringes with lattice spacing on the image plan, which

correspond to the atom columns of the specimens. This imaging technique with the atomic resolution is call high resolution transmission electron microscopy (HRTEM). In spite of the fact that an HRTEM image contains identical information as the diffraction pattern does, HRTEM is capable of providing detailed diffraction information of very localized structures that are way smaller than the lower limit of the selected area aperture. In that case, HRTEM is ideal to investigate the orientation relationship between the particles and the matrix in matrix-inclusion systems (see Figure 2.5 for an example). Although the C_s-corrected STEM, which will be introduced later in this section, is also able to provide atomic-resolution images of oxide nanoparticles. The interpretation of these image is complex and requires extra image simulation. Hence, HRTEM was selected to help determine the orientation relationships in this study.

All the conventional TEM efforts included in this dissertation were carried out on a JEOL 2000 LaB_6 TEM and a JEOL 2010 Cryo LaB_6 TEM.

2.2.2 Scanning Transmission Electron Microscopy

As convergent beam is utilized in TEM instead of parallel beam, the electron beam can be focused on a narrow spot of the specimen. Thus, the transmitted and scattered electrons only contain information of a very localized region of the sample. Therefore, the focused spot, which is called the electron probe, can scan over the sample in a raster, while the transmitted or scattered electrons can be captured by various types of detectors to form different mappings of the specimen. This feature distinguishes the technique, scanning transmission electron microscopy (STEM) from conventional TEM (see Figure 2.6). The most commonly used detector is the annular dark field (ADF) or high angle annular dark field (HAADF) detectors. Locating at high scattering angle, ADF/HAADF detector can minimize the influence of the Bragg diffracted electron, and only capture those Rutherford scattered electrons. As the differential cross section of Rutherford scattering is proportional to the square of the atomic number, Z^2, the contrast provided by the HAADF detector is call Z-contrast. Z-contrast image is very sensitive to the element composition of the specimen, making it a strong tool to

examine the chemical information. More importantly, STEM can be combine with some powerful spectroscopies, such as the energy dispersive X-ray spectroscopy (EDS) and the electron energy loss spectroscopy (EELS), to provide semi-quantitative chemical information. Hence, STEM-EDS and/or STEM-EELS, also called analytic STEM, are great tools to investigate the chemical composition of the precipitates within the matrix, such as the ODS steel systems studied in this dissertation.

The early version of STEM was just equipped by the conversional LaB_6 filament, which has relatively low brightness and large probe size, limiting the resolution and performance of the technique. The innovation of the field emission gun (FEG) significantly enhances the brightness of the electron source and reduces the probe size of the convergent beam, and therefore makes the STEM really practical. However, even with the powerful FEG source, STEM still suffers with severe spherical aberration (C_s) so that the electron quality of the probe is not good enough to form atomic resolution STEM image. Most recently, a pair of hexapole magnets were introduced to cancel the third-order spherical aberration of the condenser lenses to form a C_s-corrected probe on the specimen. Thus, atomic resolution is realized in STEM. In this study, all the STEM investigations were performed on a JEOL 2010F EF-FEG STEM.

2.2.3 *In-situ* TEM Deformation Investigation

Although the diffraction contrast of TEM can image dislocation and nanoparticles simultaneously, the ordinary setups of TEM investigations, which usually employ a single-tilt, double-tilt, or rotation-tilt stage, are unable to introduce real-time strain into the specimens and therefore are incapable of producing any dynamic information of nanoparticle-dislocation interaction mechanisms within ODS steels. An *in-situ* TEM deformation holder was developed by Gatan to provide feasibility of observing microscopic dynamic processes within TEM specimens. A TEM tensile specimen that is mounted on a Gatan 645 single-tilt straining holder is shown in Fig. 2.7.

The holder was designed to be able to compress or tensile a specimen via displacement control mode so that the microstructure responses of the

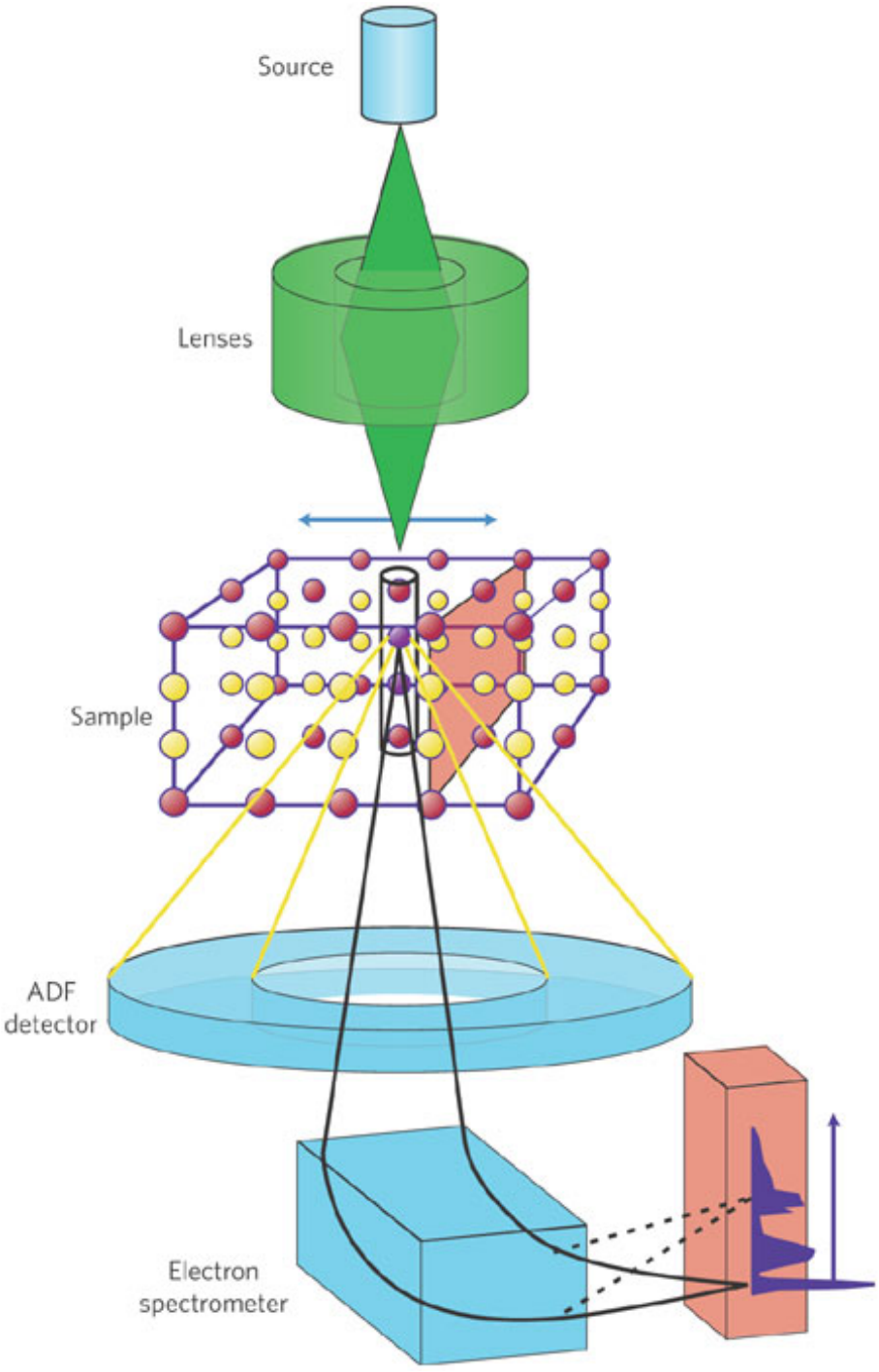

Figure 2.6: Major elements of a STEM[79]

Figure 2.7: An *in-situ* TEM deformation holder with a sample loaded

specimen, such as dislocation glide and crack propagation, can be real-time monitored and recorded by the TEM. For the ODS steel specimens studied in this dissertation, tensile mode of the straining holder was employed to activate the slip systems inside the samples so that the nanoparticle-dislocation interactions can be examined, as shown in Fig. 2.8. The *in-situ* TEM deformation investigation was performed on a JEOL 2010 LaB_6 TEM at the Fredrick Seitz Material Research Laboratory at the University of Illinois at Urbana-Champaign and on the IVEM-Tandem facility at Argonne National Laboratory. Both TEM machines are equipped with a Gatan 645 single-tilt straining holder.

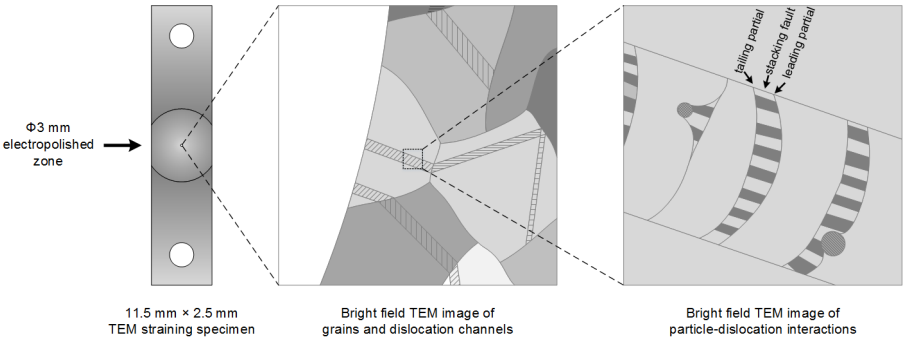

Figure 2.8: Setup of the *in-situ* TEM deformation investigation

2.2.4 Sample Preparation

Samples of good quality are the foundation of excellent TEM images. The TEM imaging requires the specimens to be thinned to electron transparency. A series of sample preparation methods, including focused ion beam (FIB),

electropolishing, and ion milling, are commonly utilized to prepare the TEM samples. In this study, electropolishing was employed to prepare ordinary samples and *in-situ* TEM straining samples, whereas FIB was used when the interests were focused on some specific regions.

For the ordinary TEM specimens, the sample was first mechanically thinned down to 100 μm. The sample surface is as smooth as 1200 Grit to avert any heterogeneous corrosion during electroplating. Then the discs were electropolished by a Struer TenuPol-5 twin-jet polisher using a solution containing 5 vol.% perchloric acid and 95 vol.% methanol at -14°C till penetrated.

For the *in-situ* TEM straining samples, 11.5 mm (length) $\times$ 2.5 mm (width) $\times$ 150 μm (thickness) stripes were cut and mechanically polished to 1200 Grit. Two holes were drilled for each sample to mount it on to the TEM stage. Then the central areas of the samples were electropolished using the same device and recipe as used for the ordinary TEM discs.

When a specific region of the a bulk sample needs to be investigated by TEM, the gauge area of the tensile specimen, for instance, FIB was utilized to lift-out the TEM specimens. The surface of the bulk sample was first polished down to 0.05 μm in order to provide a smooth surface for FIB fabrication. A 20 μm $\times$ 10 μm $\times$ 1.5 μm slice was lifted out of the bulk material and mounted to a 3 mm semicircle OmniProbe TEM grid. The central region of the slice was then be polished by 30 keV Ga ion beam and then cleaned by 2 keV Ga ion beam. All the FIB sample preparations were performed on an FEI HELIOS 600i FIB and an FEI DB235 FIB at Fredrick Seitz Material Research Laboratory, University of Illinois at Urbana-Champaign.

2.3 Atom Probe Tomography

Atom probe tomography (APT) has been developed in the past decades based on the success of field ion microscopy (FIM)[80]. The fundamental principle of APT is shown in Fig. 2.9[81]. A high voltage pulser is employed to create a strong electric field in order to ionize the atoms on the specimen surface and then pull the ions out. For those samples of poor thermal

or electric conduction, laser pulses are adopted to illuminate the specimen to facilitate the ion emission. The specimen is made as a sharp needle to maximize the electric field near its tip. The pulled ions are collected by a position-sensitive time-of-flight (ToF) detector. The types of ions are determined by the charge-mass ratios derived from the flight time, whereas the original positions of the ions are reconstructed assuming that the specimen has a perfectly hemispherical surface. With the development of the detector technology, a state-of-the-art local electrode atom probe (LEAP) is capable of collecting over half of the ions from the specimen and reconstructing their original positions with their element information. With advanced reconstruction algorithm such as 3-D Hough transformation, even the crystalline lattice can be restored[82]. Intrinsically, APT has atomic resolution and theoretically is able to distinguish all types of isotopes. However, the dimensions APT samples are limited to hundreds of nanometers. Therefore, APT is a powerful tool to characterize nano-scale features of high spatial density, such as the oxygen-enriched nanoparticles in ODS steels[83].

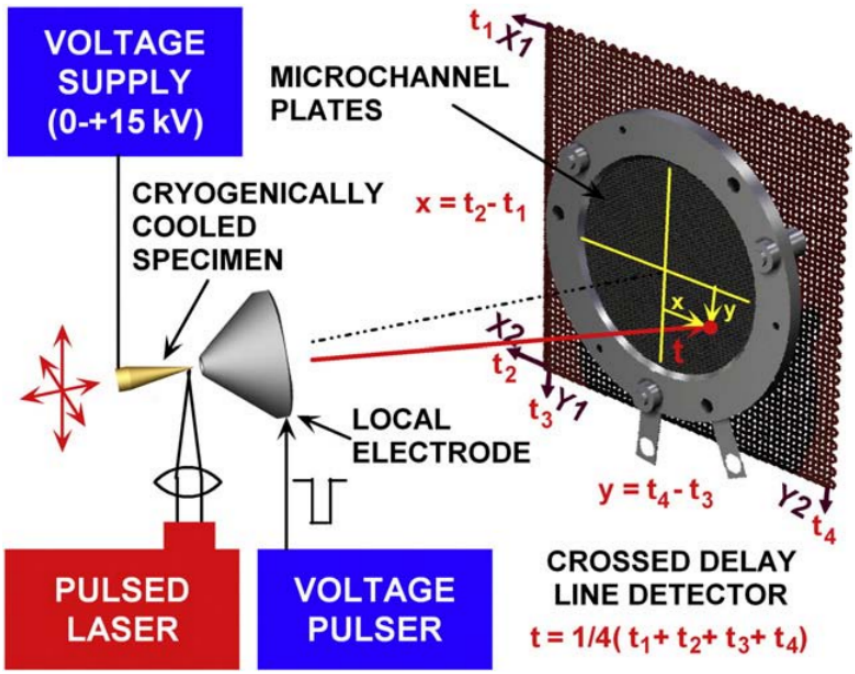

Figure 2.9: The Fundamental principle of APT

Specimens for atom probe tomography (APT) were fabricated from small blanks (0.25mm ×0.25mm ×10mm) that were cut from the bulk mate-

rial. The blanks were electropolished into needle-shaped specimens with the use of a standard loop method in a Simplex Electropointer and standard electrolytes[84]. The needle-shaped specimens were annular milled in a Dualbeam FEI Nova 200 Nanolab focused ion beam/scanning electron microscope (FIB/SEM) to ensure a circular cross section, as well as a suitable end radius and taper angle[85]. APT characterizations were performed in an energy-compensated CAMECA Instruments Inc. local electrode atom probe (LEAP® 4000X HR). Due to the relatively poor electrical and thermal conduction of these materials, the specimens were analyzed in laser-mode at a specimen temperature of 30 K, a pulse repetition rate of 200 kHz, a focused laser beam energy of either 50 or 100 pJ, and a data collection rate between 0.5% and 4% ions per field evaporation pulse depending on the standing voltage applied to the specimen. The position of the laser beam on the apex of the specimen was adjusted automatically during the experiment to account for the field evaporation of material from the apex of the specimen and specimen drift. These conditions resulted in individual LEAP® datasets containing up to 600 million atoms. Surface regions that contained damage from the gallium ion beam were not used for analysis. Data analysis was performed with the use of CAMECA Instruments Inc. Integrated Visualization and Analysis Software (IVAS 3.6.6). The proxigrams[86] were calculated according to the isosurfaces defined by 6% decomposed oxygen concentration. Thus, the size of the oxygen-enriched nanoclusters are determined by the effective diameters (d_{effe}) based on the volumes (V) defined by the oxygen isosurfaces, $d_{eff} = (6V/\pi)^{1/3}$.

2.4 Synchrotron X-ray Scattering

Since it was discovered in late 19th century, X-ray has been playing an indispensable role in the characterization of materials. A variety of techniques have been developed based on the application of X-ray, including X-ray diffraction or wide-angle X-ray scattering (XRD or WAXS), small-angle X-ray scattering (SAXS), X-ray absorption spectroscopy (XAS, including X-ray absorption near edge structure, XANES, and X-ray absorption fine structure, XAFS), X-ray photoelectron spectroscopy (XPS). However, conventional X-

ray sources have relatively low energy and low intensity, limiting their application in advanced characterizations. Fortunately, the development of high-energy accelerator technology makes it possible to form synchrotron X-ray with up to 100 keV energy and high intensity. The high-energy X-ray is able to transmit steel specimens with millimeter-level thickness, while the high intensity of X-ray improve the signal-to-noise ratio (SNR) so that the scattering contributed by phases of marginal volume fractions can be distinguished. Neither of the advantages of synchrotron X-ray can be realized by any conventional X-ray sources. Hence, synchrotron X-ray provides unique capabilities of examining the material properties and was employed in this study to investigate the characteristic and behaviors of both the matrices and precipitates in ODS steels.

2.4.1 Synchrotron Experiment Setup

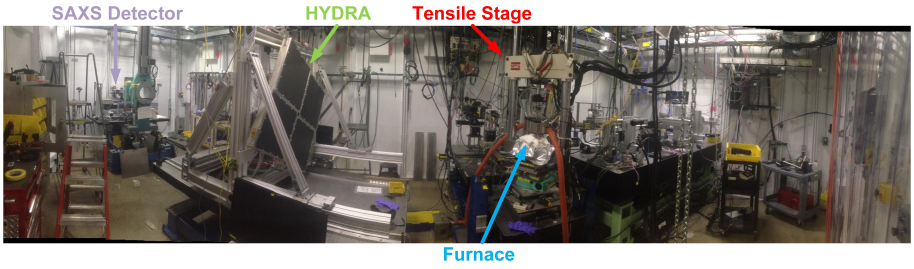

Figure 2.10: Synchrotron experiment setup

All the synchrotron related experiments in this study were carried out at Sector 1-ID-E, Advanced Photon Source (APS), Argonne National Laboratory (ANL). In this sector, a well-designed experimental setup was arranged to conduct *in-situ* synchrotron tensile investigations on the miniature ODS tensile specimens, as shown in Fig. 2.10. The synchrotron X-ray was first filtered by a Si(111) monochromator so that only 70 keV monochromic X-ray hits the specimens. Multiple ion chambers were set up to record the X-ray intensities at different stages. An MTS tensile machine was used to perform the uniaxial tensile tests. The tensile specimens were sieged with a lamps furnace that can heat the specimen up to 1000 °C. Then the scattered X-ray was respectively collected by SAXS and WAXS detectors.

A more detailed setup diagram can be found as Fig. 2.11. The WAXS signal was collected by a detector array composed of four identical GE angio type 41 cm × 41 cm 2D detectors, which is named "Hydra" detector array. Meanwhile, the SAXS signal was captured by a 25 cm × 20 cm 2D detector after blocking the transmitted beam using a beamstop.

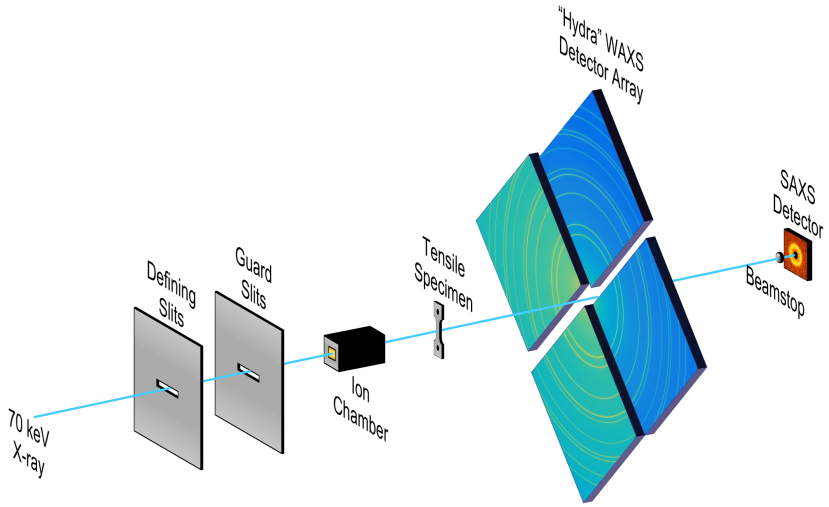

Figure 2.11: Synchrotron experiment setup

The tensile specimens were loaded and strained on the MTS tensile machine equipped with a furnace. Synchrotron exposures were taken during straining. Two different exposure strategies were used for different specimens. In one case, the specimens were strained by step mode. That is, load control mode was used for elastic regime whereas the displacement control mode was used for plastic region. The load/displacement was hold for each step so that 9 evenly distributed spots on the gauge area alongside the uniaxial tensile direction were hit by synchrotron for exposures successively. Thus, 9 independent data sets were collected for each strain-stress point. As a result, the necking area can always be captured and there exist sufficient data for better statistics. However, the discontinuity of straining make the testing lack of a well-defined strain rate, and all the properties dependent on the strain rate were influenced. In the other case, a constant strain rate was set up and the specimens were continuously strained as the synchron exposures were made on a single point. This method solved all the problem coupled with the step mode, but can not capture the necking and non-necking area simultaneously.

2.4.2 Analyses on the Texture, Lattice Strain and Volume Fracton

The 10° region of the Debye-Scherrer rings near the uniaxial tensile direction was integrated to give the lattice strain of that direction, $\varepsilon_{11} = (d - d_0)/d_0$. For the austenite matrix, the average bulk lattice strain was calculated from the lattice strains of (111), (200), (220), and (311) reflections using the weighted averaging algorithm developed by Daymond[87]:

$$\bar{\varepsilon} = \frac{\sum_{hkl} \alpha_{hkl} \varepsilon_{hkl}}{\sum_{hkl} \alpha_{hkl}}, \tag{2.3}$$

where, $\bar{\varepsilon}$ is the average bulk lattice strain of the matrix, ε_{hkl} is the lattice strain of the (hkl) reflection, and α_{hkl} is the weight coefficient with the following definition:

$$\alpha_{hkl} = T_{hkl} p_{hkl} E_{hkl} / \bar{E}. \tag{2.4}$$

Here, p_{hkl} is the multiplicity of the (hkl) reflection, E_{hkl} is the Young's modulus of the (hkl) orientation, $\bar{E}$ is the average Young's modulus of the bulk austenite matrix, and T_{hkl} is the Harris texture index[88]:

$$T_{hkl_i} = \frac{I_{hkl_i}/R_{hkl_i}}{\frac{1}{n}\sum_{j=1}^{n} I_{hkl_j}/R_{hkl_j}}, \tag{2.5}$$

where, I_{hkl} is the integrated intensity of the (hkl) reflection, and R_{hkl} is the theoretical integrated intensity of the (hkl) reflection produced by an untextured sample:

$$R_{hkl} = \frac{1}{V^2}[|F|^2 p(\frac{1 + cos^2 2\theta}{sin^2\theta cos\theta})]e^{-2M}, \tag{2.6}$$

where, V is the volume of the unit cell; F is the structure factor; p is the multiplicity of the reflection; $\frac{1+cos^2 2\theta}{sin^2\theta cos\theta}$ is the Lorentz-polorization factor as a function of diffraction angle θ; and e^{-2M} is the Debye-Waller temperature factor, which has the following expressions:

$$e^{-2M} = exp[-\frac{B sin^2\theta}{\lambda^2}], \tag{2.7}$$

and

$$B = \frac{6h^2}{m_a k\Theta}[\frac{\phi(x)}{x} + \frac{1}{4}], \tag{2.8}$$

where, h is Plank constant, m_a is the mass of atom, k is Boltzmann constant, Θ is Debye temperature, and the rest of Equation 2.8 is Debye function.

The integrated intensities can also be used to calculate the volume fractions of corresponding phases[89]:

$$V_i = \frac{\frac{1}{n_i}\sum_{j=1}^{n_i}\frac{I_i^j}{R_i^j}}{\frac{1}{n_a}\sum_{j=1}^{n_a}\frac{I_a^j}{R_a^j} + \frac{1}{n_{p_1}}\sum_{j=1}^{n_{p_1}}\frac{I_{p_1}^j}{R_{p_1}^j} + \frac{1}{n_{p_2}}\sum_{j=1}^{n_{p_2}}\frac{I_{p_2}^j}{R_{p_2}^j} + ...}, \tag{2.9}$$

where, V_i is the volume fraction of phase i; i represents austenite (subscription $_a$) and various precipitate phases (subscriptions $_{p_1}$, $_{p_2}$...); I_i^j is the integrated intensity of the reflection of j (for a specific hkl) for phase i; n_i is the number of the reflections analyzed for a certain phases; and R_i^j is the material scattering factor for a specific phase (i) and reflection (j), which has the same expression as Equation 2.6.

2.4.3 The Modified Williamson-Hall Analysis

Other information was obtained by analyzing the breadth of WAXS peaks according to the modified Williamson-Hall (W-H) method. The modified W-H analysis usually gives grain size and dislocation density of each phase. However, in the case of FCC alloys with low stacking fault energies (SFE), such as 304 and 316 steel, the evolution of stacking and twinning faults, which significantly contributes to the peak broadening, sometimes also plays a role in plastic deformation. Therefore, a modified W-H method that considers stacking and twinning faults was employed for the austenite phase[90]:

$$\Delta K = (\frac{1.5\alpha + \beta}{a})W(g) + \frac{0.9}{D} + (\frac{\pi A^2 b^2}{2})^{\frac{1}{2}}\rho^{\frac{1}{2}}(K\overline{C}^{\frac{1}{2}}), \tag{2.10}$$

where α is the stacking fault portion, β is the twinning fault portion, a is the lattice parameter, $W(g)$ is a reflection-dependent parameter given in Ref. [90], D is the grain size, A is an adjustable parameter that was chosen to

be 1 for compatibility with a dislocation density of approximately 10^{14} m^{-2}, $\overline{C}$ is the averaged contrast factor, which will be discussed in detail later, $K = 2sin\theta/\lambda$, $\Delta K = 2cos\theta\Delta\theta/\lambda$, θ is the diffraction angle, and $\Delta\theta$ is the breadth of the peak. A pseudo-Voigt function was used for peak fitting. The pseudo-Voigt peak has two components:

$$pV(2\theta) = I_0[\eta L(2\theta) + (1-\eta)G(2\theta)], \tag{2.11}$$

where I_0 is the peak intensity, $L(2\theta)$ is the Lorentzian component, $G(2\theta)$ is the Gaussian component, and η is the portion of the Lorentzian component. The breadth of the peak then has the following form:

$$\Delta\theta = \omega[\pi\eta + (1-\eta)(\pi/ln2)^{1/2}], \tag{2.12}$$

where ω is the half of the peak's FWHM. The values of $\overline{C}$ for edge ($\overline{C}_e$) and screw ($\overline{C}_s$) dislocation are different. This difference was utilized to quantify the fraction of the screw dislocation, ν_s. To do this, two parameters that determine $\overline{C}$ need to be averaged separately according to Ungár et al.'s report[91]:

$$\overline{C} = \overline{C}_{h00}(1 - qH^2), \tag{2.13}$$

where $\overline{C}_{h00}$ is the average contrast factor of $(h00)$ reflections, q is a material characteristic parameter, and $H^2 = (h^2k^2 + h^2l^2 + k^2l^2)/(h^2 + k^2 + l^2)^2$ is a reflection parameter. Both $\overline{C}_{h00}$ and q are dependent on the elastic constants of the crystal[92], and can be calculated according to the method introduced by Ungár et al[91]. As both edge and screw dislocation exist in the crystal, the $\overline{C}$ has the following expression:

$$\overline{C} = [\nu_s\overline{C}_{h00,s} + (1-\nu_s)\overline{C}_{h00,e}]\{1 - [\nu_s q_s + (1-\nu_s)q_e]H^2\}, \tag{2.14}$$

where ν_s is the fraction of screw dislocations, subscriptions $_s$ and $_e$ represent screw and edge dislocations, respectively. The ν_s that maximizes the coefficient of determination (R^2) when fitting Equation 2.10, was regarded as the fraction of screw dislocations in the specimen. Fig. 2.12 provides two

typical examples of the modified W-H fitting of the real data collected from a strained ODS 316 specimen.

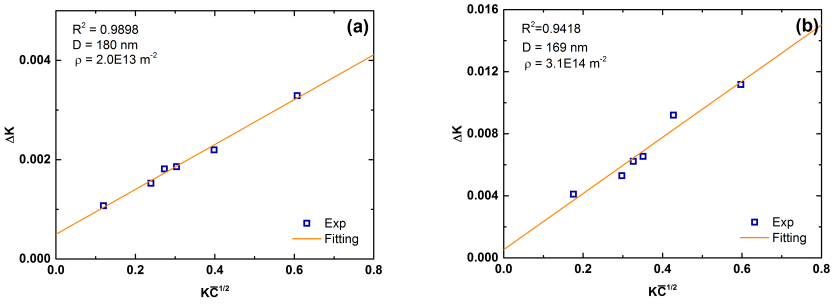

Figure 2.12: Examples of the modified W-H fitting

2.4.4 Small-Angle X-ray Scattering

Aside from WAXS analyses, small angle X-ray scattering (SAXS) is also capable of revealing some properties of the precipitates. From the SAXS data, the size distribution of the nanoparticles can be retrieved. In this study, IRENA package[93] was utilized to perform the SAXS data analyses. The nanoparticles were assumed to have unified sphere shape[94]. Namely, these nanoparticles have the form factor as follows:

$$F^2 = exp\{-\frac{q^2 {R_g}^2}{3}\} + \frac{1.62}{{R_g}^4}\left[\frac{erf^3(qR_g/\sqrt{6})}{q}\right]^4, \tag{2.15}$$

where, $q = 4\pi sin\theta/\lambda$ is the scattering vector; R_g is the radius of gyration, which equals $\sqrt{3/5}r$ for spherical precipitates. The fitting of SAXS data was based on the maximum entropy algorithm[95, 96] so that the size distribution of nanoparticles could be assessed.

2.4.5 Scanning Electron Microscopy

Unlike the TEM, a scanning electron microscope does not form images using the transmitted or diffracted electron. Instead, an SEM utilizes a focused low energy electron probe to produce secondary electrons (SE) and backscattering electrons (BSE). SE images reflect the surface geometry information

while the BSE images indicate the element information near the surface. In this study, SEM was utilized to image the fracture surfaces of the strained miniature tensile specimens. The SEM efforts were carried out on a JEOL 7000F SEM.

CHAPTER 3

CHARACTERIZATIONS OF THE OXIDE NANOPARTICLES

The intrinsic properties of the oxide nanoparticles within all the three austenitic ODS steels involved in this study, including the chemical composition, crystallography, and morphology, are discussed in this chapter. The results provide comprehensive information of the oxide nanoparticles, which is the origin of the excellent performance of austenitic ODS steels.

3.1 Hafnium-containing ODS 316 Stainless Steel

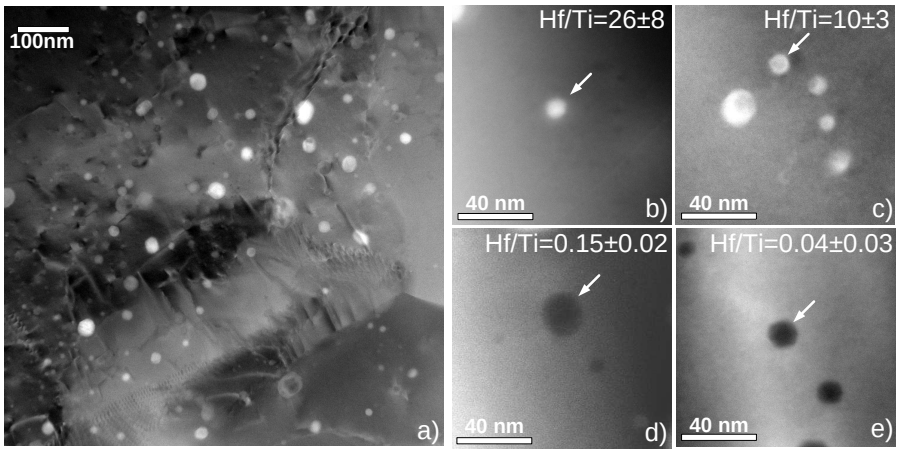

Figure 3.1: STEM HAADF images: (a) typical microstructure of ODS 316 stainless steel; (b) through (e) $Y_2(Ti,Hf)_{2-x}O_{7-2x}$ nanoparticles with various Hf/Ti ratios. The discrete Hf/Ti ratios were selected only to show the significant variation of this quantity.

The STEM HAADF image, Fig. 3.1(a), illustrated the prominent Z-contrast of the oxide nanoparticles. EDS indicates that the particles are complex oxides containing Y, Ti, and Hf (see Fig. 3.2). Due to the existence of the heavy element Hf, the contrast of the nanoparticles appears brighter than

those of Y-Ti-O nanoparticles observed in other ODS alloys. APT data reconstruction also indicated that the oxygen-enriched dispersed nanoparticles smaller than 5 nm (also called nanoclusters) contain Y, Ti and Hf (Fig. **??**). The quantitative analysis results of the oxygen-enriched nanoparticles by both STEM-EDS and APT are illustrated in a ternary coordinate system so that the contents of all three major metal elements (Y, Ti, and Hf) can be shown in Fig. 3.4. The color of the data points indicates the size of the oxygen-enriched nanoparticles obtained by measuring STEM images or APT isosurface data. According to these chemical composition data, the Y-Ti-Hf-O inclusions can be divided into three discrete groups: Y_2O_3, Y_2O_3-HfO_2 solid solution, and $Y_2(Ti,Hf)_{2-x}O_{7-2x}$. Y_2O_3, which has a bixbyite structure, was present in the original oxide powders added before ball milling. It is well known that the Y_2O_3 and HfO_2 can form solid solution with fluorite structure[97], and that the Y_2O_3-HfO_2 solid solution has a minimum enthalpy near $Y/Hf = 1$, namely, $Y_2Hf_2O_7$[98]. It had been believed until recently that $Y_2Ti_2O_7$ was the only cubic phase Y-Ti-O compound, whereas another common Y-Ti-O compound, Y_2TiO_5 had an orthorhombic structure. According to recent reports[99], Ti atoms in $Y_2Ti_2O_7$ could be replaced by Y through vacancy compensation mechanism[40] so that pyrochlore $Y_2Ti_{2-x}O_{7-2x}$, including Y_2TiO_5, could form[100]. As Ti and Hf belong to the same group on the periodic table, it is plausible that Hf can replace Ti in $Y_2Ti_{2-x}O_{7-2x}$. Thus, $Y_2(Ti,Hf)_{2-x}O_{7-2x}$ whould have a pyrochlore or fluorite structure, depending on the Hf/Ti ratio. For example, the boundary ratio of Hf/Ti between fluorite and pyrochlore structures for $Y_2(Ti,Hf)_2O_7$ is Hf/Ti = 7.71 according to the averaged ion radius[101] and the judging criteria in Ref. [39]. An interesting phenomenon involving $Y_2(Ti,Hf)_{2-x}O_{7-2x}$ nanoparticles is that the Z-contrast of these particles actually reflects their Hf/Ti ratio. The HAADF-STEM images of $Y_2(Ti,Hf)_{2-x}O_{7-2x}$ nanoparticles, Fig. 3.1(b) through (e), illustrate the variation in the Hf/Ti ratios measured by quantitative EDS analyses.

Because both bixbyite and pyrochlore structures are variants of the fluorite structure, all have similar major diffraction peaks. Therefore, synchrotron XRD data can only show the oxide peaks ({222} and {400}) to which all three inclusion phases mentioned above contribute (see Fig. 3.5). Due to the existence of extra oxygen vacancies in both bixbyite and pyrochlore structures,

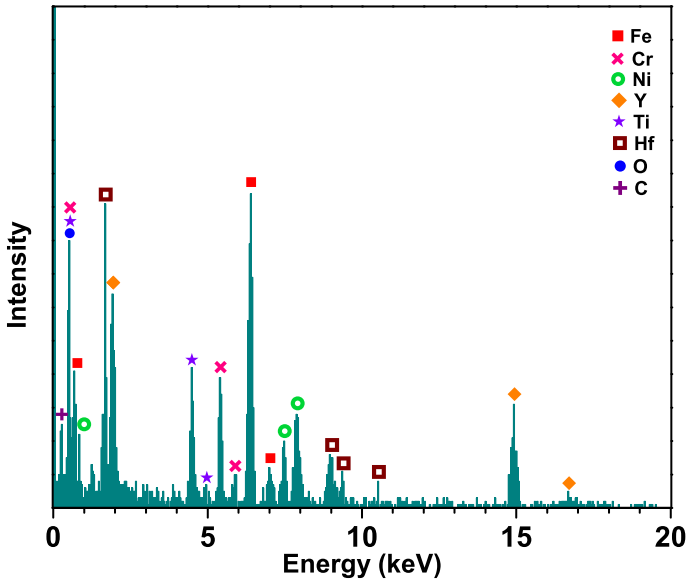

Figure 3.2: A typical EDS result of an oxide nanoparticle showing the enrichment of Y, Ti, Hf, and O.

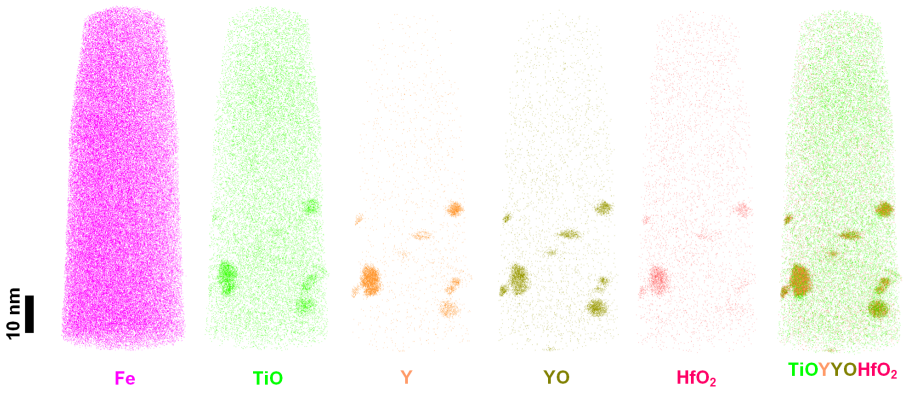

Figure 3.3: Atom probe tomography data showing the enrichment of Y, Ti, Hf, and O in nanoclusters: Y, Ti, and Hf are enriched in these nanoclusters due to their strong affinity for oxygen.

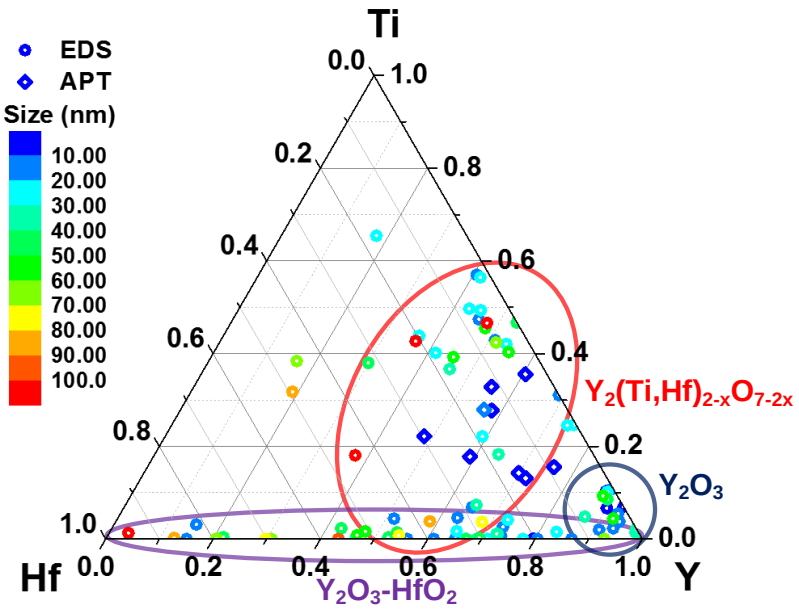

Figure 3.4: Chemical composition distribution of oxide particles with various dimensions and compositions in ODS 316 steel (circles from STEM-EDS and diamonds from APT).

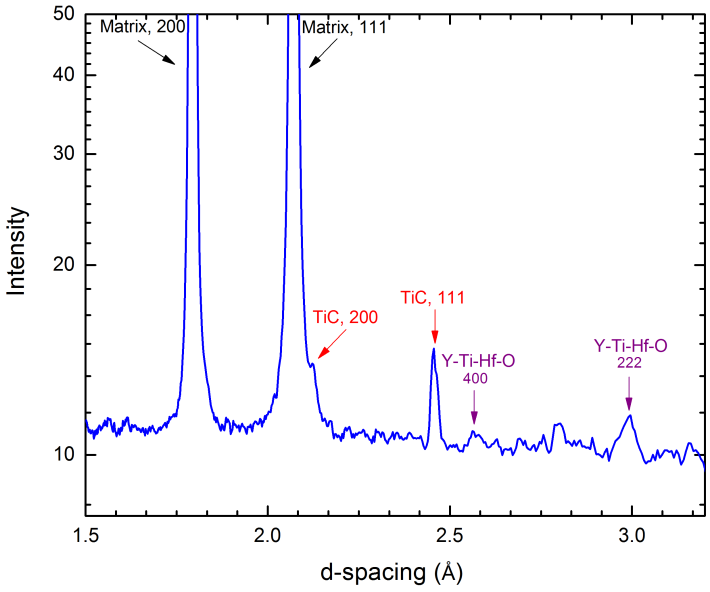

Figure 3.5: Synchrotron X-ray diffraction of ODS 316.

the atoms in these two structures are displaced from the reference fluorite lattice positions, making the spatial periods twice that of the fluorite structure. Therefore, the Miller indices of these two variants are different by a factor of 2 from their equivalents of the fluorite structure. In this manuscript, all these values are expressed according to the pyrochlore or bixbyite structure regardless of the actual structure of the nanoparticle for uniformity. The lattice parameter of the austenite matrix was determined to be 3.595 $\mathring{A}$.

3.2 ODS 304 Stainless Steel

A typical STEM Z-contrast image of the pre-strained ODS 304 specimen is shown in Fig. 3.6. Three types of precipitates with various morphologies can be distinguished. One is the polyhedral particles with large scale (around 100 nm), the second is the nearly spherical particles with intermediate scale (around 20 nm), and the third is particles with extremely small scale ($<$ 5 nm). EDS analyses indicated that the polygonal particles are enriched in Ti and N; while the intermediate phases are enriched in Y, Al and O. Aluminum was not added into the system intentionally. However, it is a common impurity in raw metal powders. The Y/Al ratio measured by EDS showed the existence of both yttrium aluminum monoclinic (YAM), $Y_4Al_2O_9$, and yttrium aluminum garnet (YAG), $Y_5Al_3O_{12}$. The portion of YAM is much larger than that of YAG. STEM-EDS is incapable of analyzing the chemical composition of the extremely small precipitates due to the limitation of resolution and the contributions from the matrix. APT has atom-level resolution, and therefore was used to characterize these extremely small dispersive nanoclusters. APT succeeded in capturing these small nanoclusters and showed that they mainly contain Y, Ti and O. Those Y-Ti-O nanoclusters also contain low but non-negligible content of Al (see Fig. 3.7), which is consistent with Sakasegawa et al.'s findings in the ferritic ODS steel, MA957[102]. The volume fraction of these Y-Ti-O nanoclusters is 0.23% as determined by the APT data.

Synchrotron XRD results of the pre-strained sample are shown in Fig. 3.8. Based on the chemical composition information obtained by STEM-EDS and APT, two precipitate phases can be identified: TiN and YAM. TiN has a

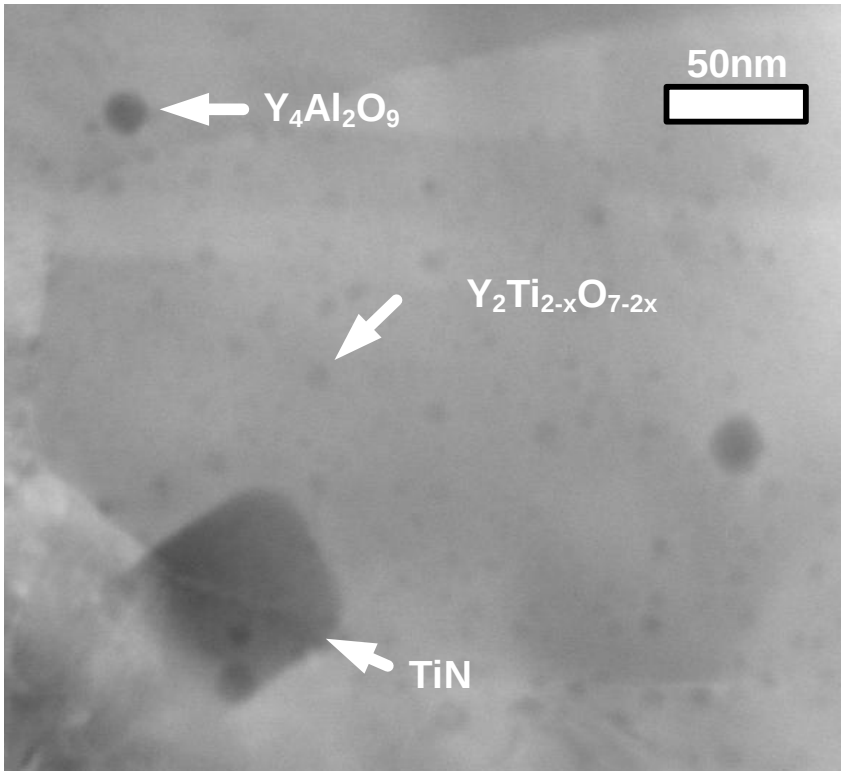

Figure 3.6: STEM HAADF images showing the existence of three precipitate phases: large scale TiN, intermediate scale Y-Al-O, and small scale Y-Ti-O

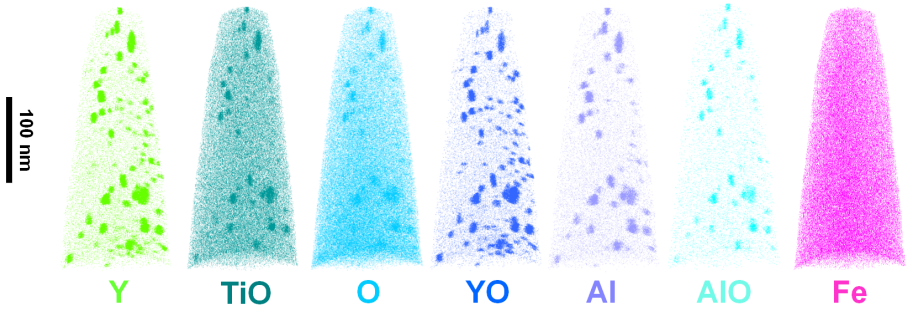

Figure 3.7: APT data showing the enrichment of Y, Ti, and O in small nanoclusters. Low but non-negligible content of Al was also found in these nanoclusters.

trivial sodium chloride structure, and its strongest reflection was found to be {111}; in the contrast, the strongest reflections of YAM are {023}/032} reflection and {22$\bar{1}$} reflection, both of which show similar intensity (Fig. 3.8). According to previous studies, Y-Ti-O nanoclusters smaller than 2 nm lack a crystal structure, but large Y-Ti-O particles have a stoichiometry of $Y_2Ti_{2-x}O_{7-2x}$, which has a pyrochlore structure[103, 100]. Therefore, Y-Ti-O nanoparticles contribute either no peaks or peaks of the pyrochlore structure. Due to the low volume fraction of Y-Ti-O, it is common that only the strongest peak, {222}, is distinguishable. Unfortunately, the d-spacing of {222} reflection is approximately 2.95 $\mathring{A}$, close to the d-spacings of the dual reflections of YAM. Since the intensity of YAM reflections is higher, the {22$\bar{1}$} reflection of Y-Ti-O cannot be identified. Therefore, in this synchrotron study, only two precipitate phases, TiN and YAM, were analyzed and discussed. The volume fractions of TiN and YAM are 0.65±0.03% and 0.66±0.03%, respectively, according to the calculation based on Equation 2.9. In addition, minor peaks from the martensitic phase were also identified in the pre-strained sample. This was the consequence of the deformation-induced martensitic transformation during the processing process.

3.3 ODS 316 Stainless Steel

Multiple phases are expected to precipitate in the ODS 316 stainless steel during the heat treatment that follows the mechanical alloying. These precipitates were first examined by the synchrotron WAXS technique. The 360° integrated intensity vs. d-spacing is shown by Fig. 3.9. Aside from the strongest peaks that undoubtedly belong to the austenitic matrix of the ODS 316 steel, a variety of minor peaks are distinguishable. In fact, five different phases of precipitates were identified in this ODS 316 steel by synchrotron WAXS: TiN, hexagonal $YAlO_3$ (yttrium aluminum hexagonal, YAH), orthorhombic $YAlO_3$ (yttrium aluminum perovskite, YAP), pyrochlore $Y_2Ti_2O_7$, and orthorhombic Y_2TiO_5. The volume fraction of each distinguishable precipitate phase was calculated based on Equation 2.9, and is listed in Table 3.1. These values were averaged from synchrotron WAXS data collected at seven different points on the gauge area of the miniature

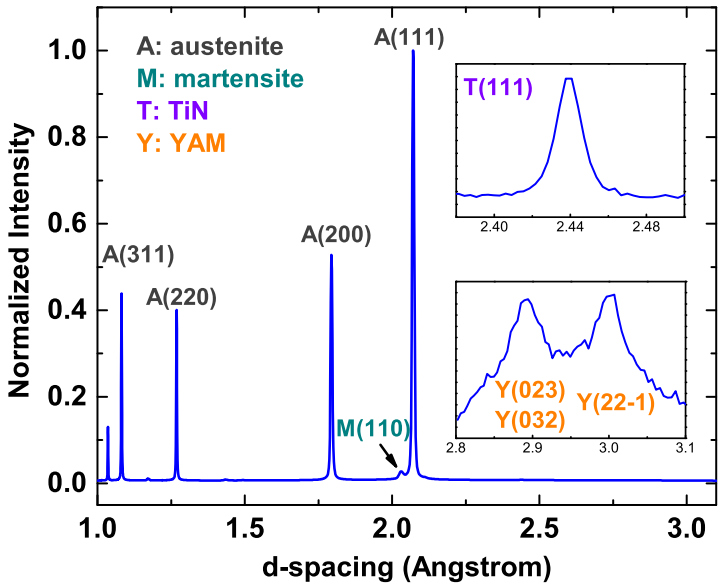

Figure 3.8: Synchrotron X-ray diffraction line profile of the pre-strained ODS 304 specimen: two matrix phases, austenite and martensite, along with two precipitate phases, TiN and YAM, can be recognized

tensile specimen.

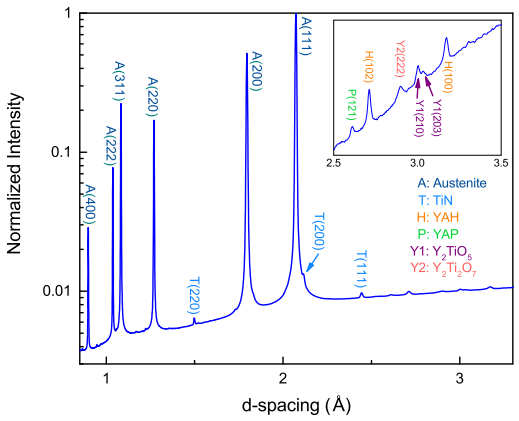

Figure 3.9: Phases identified using synchrotron X-ray WAXS: aside from the austenite matrix, TiN, hexagonal-$YAlO_3$ (YAH), orthorhombic-$YAlO_3$ (YAP), $Y_2Ti_2O_7$, and Y_2TiO_5 were distinguished. However, only the intensities of TiN, YAH, and $Y_2Ti_2O_7$ are sufficient for lattice strain analysis.

Table 3.1: Volume fractions of all the synchrotron-distinguishable precipitate phases in ODS 316 steel

Formula	Structure	Volume Fraction
TiN	sodium chloride	0.41±0.02%
$YAlO_3$	hexagonal	0.40±0.03%
$YAlO_3$	pervoskite	0.29±0.11%
Y_2TiO_5	orthorhombic	0.10±0.02%
$Y_2Ti_2O_7$	pyrochlore	0.05±0.01%

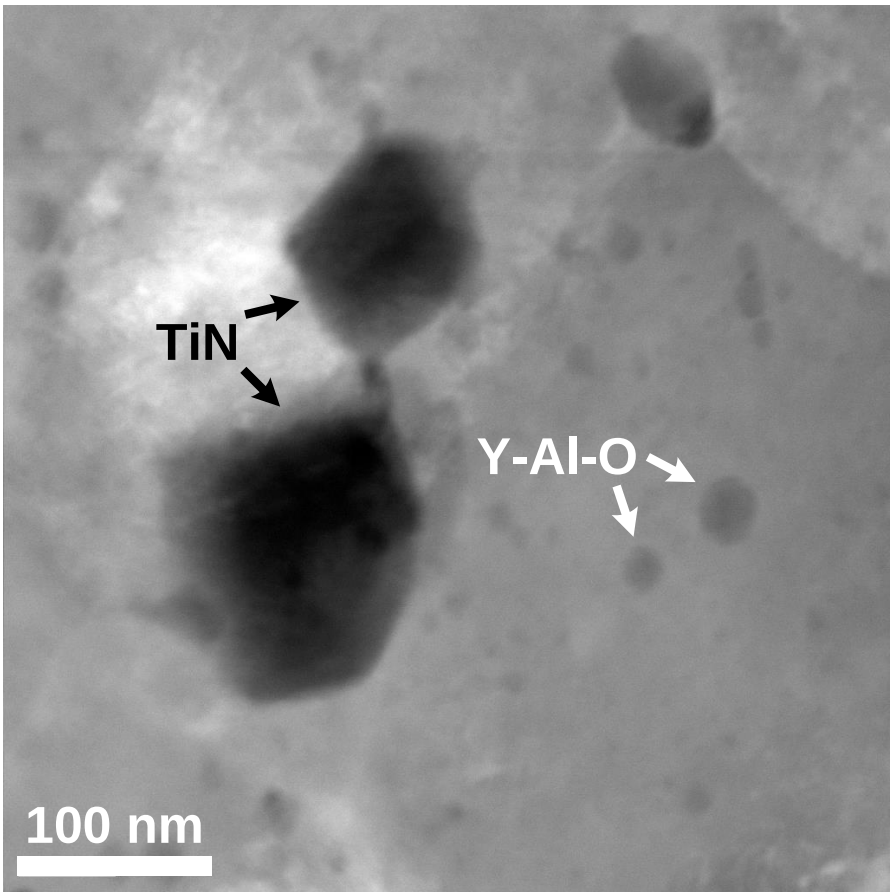

Figure 3.10: STEM Z-contrast image showing the TiN and Y-Al-O precipitates

The STEM Z-contrast image in Fig. 3.10 shows the existence of two different types of precipitates. One has a polyhedral shape with a size usually larger than 100 nm, whereas the other has a spherical shape with a size ranging from 20 to 80 nm. EDS results show that the polyhedral precipitates are TiN, while the spherical ones are YAH and YAP. The Y-Ti-O nanoparticles, which have size smaller than 10 nm, cannot be distinguished in Fig. 3.10.

Synchrotron SAXS analysis was also employed to analyze the size distribution of the precipitates. A unified sphere model was used to fit the SAXS data, which yields the size distribution shown in Figs. 3.11 and 3.12. The polymodal size distribution implies that at least two groups of nanoparticles contribute to the SAXS signal, one with an average size around 7.5 nm, and the other with a broader size distribution ranging from 20 to 70 nm. Y-Al-O nanoparticles have size on the order of tens of nm, whereas Y-Ti-O nanoparticles have a finer particle size that is usually smaller than 10 nm. The large Y-Al-O nanoparticles account for the YAH and YAP phases identified by synchrotron WAXS and STEM-EDS, while the fine Y-Ti-O nanoparticles are identified to be $Y_2Ti_2O_7$ and Y_2TiO_5, as they still have adequate size to maintain stoichiometry. The ultra-fine Y-Ti-O nanoparticles (or nanoclusters, $< 3nm$), which can be examined by APT as shown in Fig. **??**, do not have a well-defined stoichiometry or crystal structure, and therefore do not make contributions to WAXS signals. Therefore, the Y-Al-O to Y-Ti-O nanoparticle volume fraction ratio of 1.43 estimated by SAXS is much smaller than the ratio of 4.60 determined by WAXS, implying that over half of the Y-Ti-O phase has no well-defined crystalline structure. TiN precipitates, which usually exceed 100 nm in size, are too large for SAXS to capture. According to APT mass spectrum analysis, the Y-Ti-O nanoparticles still contain low, but non-negligible, Al content. However, the synchrotron WAXS results, along with the HREM results, which will be discussed shortly, indicate that the crystalline structures remain with the Al impurity. In the APT reconstruction shown in Fig. 3.13, there exists one nanoparticle-free zone and two nanoparticle-rich zones, indicating the heterogeneous distribution of the ultra-fine Y-Ti-O nanoparticles. In this case, the volume fraction of the Y-Ti-O nanoparticles of 0.08% determined by the APT data might not be representative due to the limited specimen volume.

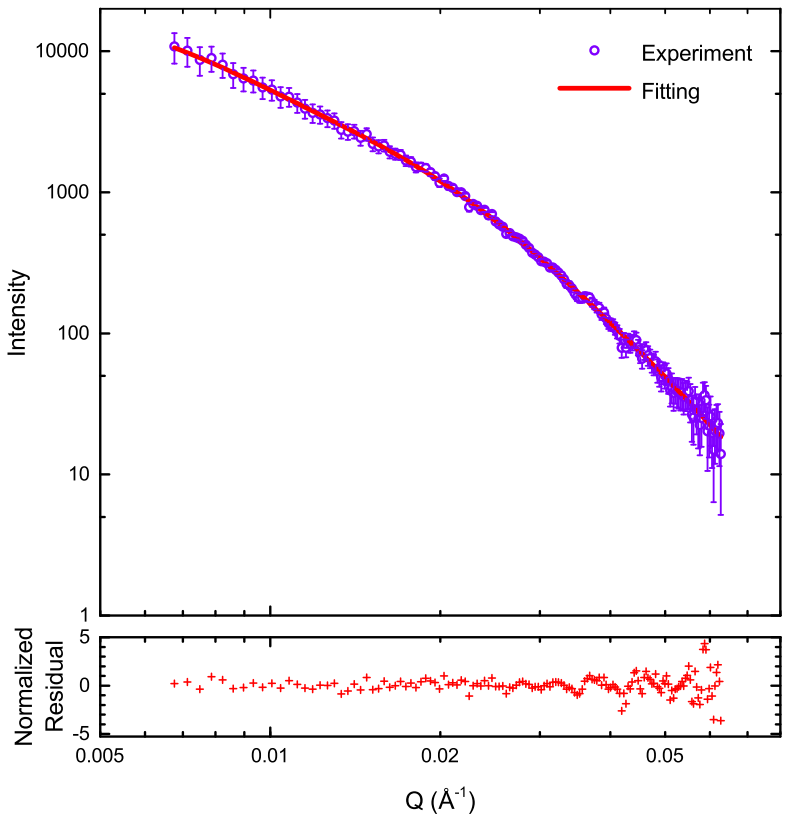

Figure 3.11: SAXS fitting

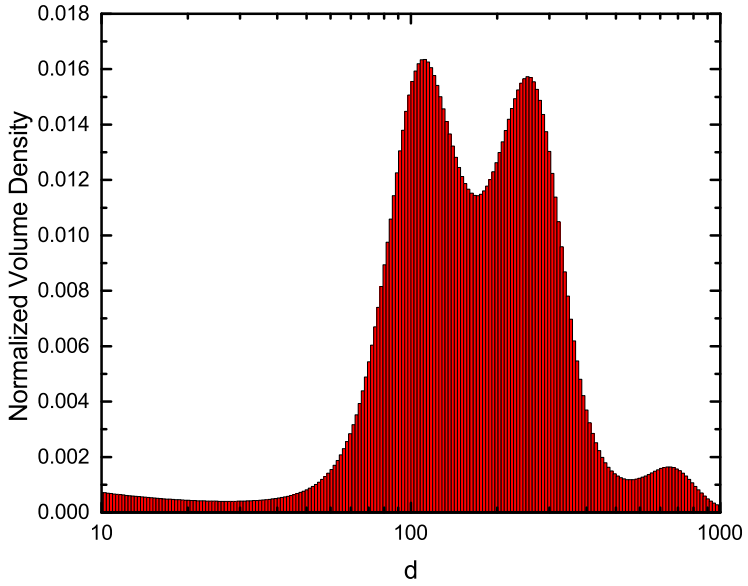

Figure 3.12: Size distribution of nanoparticles obtained by SAXS fitting. The prominent polymodal size distribution of the nanoparticles implies the existence of at least two groups of different precipitate phases

The existence of Al, the known impurity in the raw metal powders, introduces the Y-Al-O nanoparticles. The precipitation mechanisms of Y-Al-O and Y-Ti-O nanoparticles differ. A recent first principle study[50] claims that the precipitation of the oxygen-enriched nanoparticles is initiated by the formation of O-vacancy pairs, and that the relative magnitude of the oxygen-binding energies in the matrix (E_0), interface(E_s), and bulk (E_b) determine whether the precipitation of oxygen-enriched nanoparticles is favored and how large the nanoparticles are likely to grow, given a specific oxygen concentration. This thermodynamic theory predicts that Y-Al-O nanoparticles always form prior to the Y-Ti-O nanoparticles as Y, Ti, and Al are all present with O-vacancy pairs. More importantly, Y-Al-O nanoparticles are larger in size than the to Y-Ti-O nanoparticles. Therefore, with the existence of Al, the precipitation of Y-Ti-O is highly suppressed, as the Y-Al-O precipitate is thermodynamically preferred. As a result, few ultra-fine (< 10 nm) nanoparticles can form with the presence of adequate Al[104]. In the ODS 316 steel investigated in this study, the content of the impurity Al is limited, and hence Y-Al-O and Y-Ti-O nanoparticles coexist.

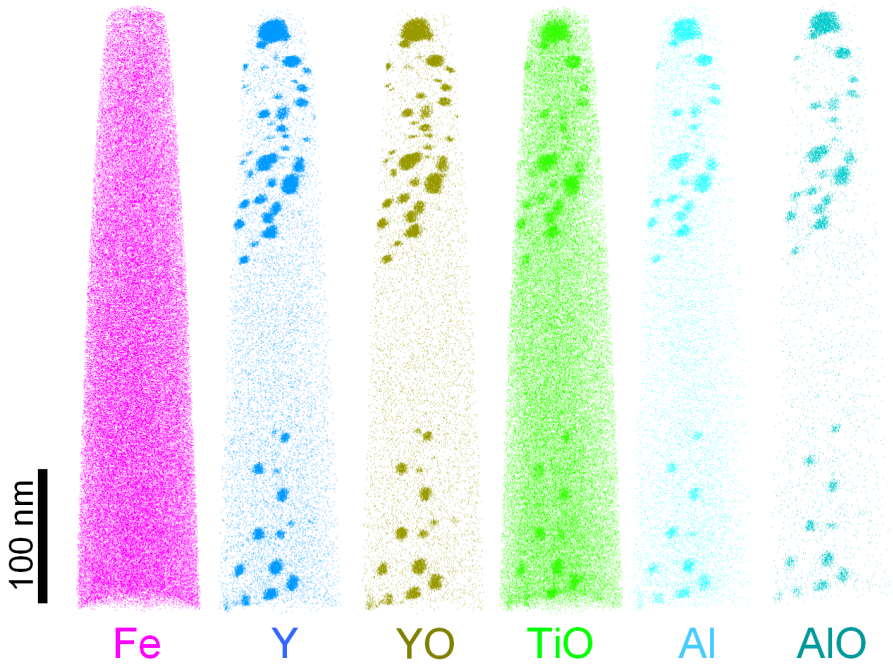

Figure 3.13: APT results of the ODS 316 steel. All the nanoparticles examined by APT are Y-Ti-O enriched nanoparticles with a non-negligible Al content. Even in this small specimen, there exist two particle-rich zones and one particle-free zone, showing the heterogeneous distribution of the ultra-fine oxide nanoparticles.

CHAPTER 4

ORIENTATION RELATIONSHIP OF OXIDE NANOPARTICLES

In this chapter, the orientation relationship of the ultra-fine oxide nanoparticles within all the three austenitic ODS stainless steels involved in this dissertation are determined by analyzing the HRTEM images with atomic resolution.

4.1 Hafnium-containing ODS 316 Stainless Steel

4.1.1 Orientation Relationship

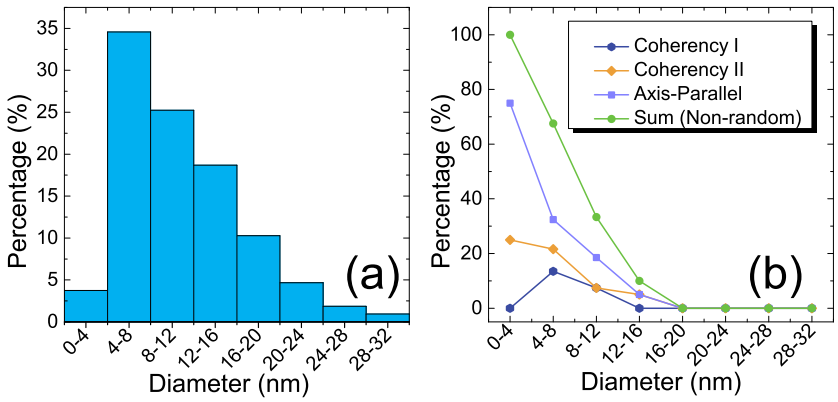

Figure 4.1: Nanoparticle size and orientation relationship: (a) normalized size distribution of oxide nanoparticles; (b) size dependency of the orientation relationship of nanoparticles.

Electron diffraction information from HRTEM of both the matrix and the nanoparticles indicated the existence of two coherency mechanisms of the nanoparticles. The HRTEM image along with its FFT diffraction pattern, Fig. 4.2, illustrates one type of coherency mechanisms (labeled as Coherency

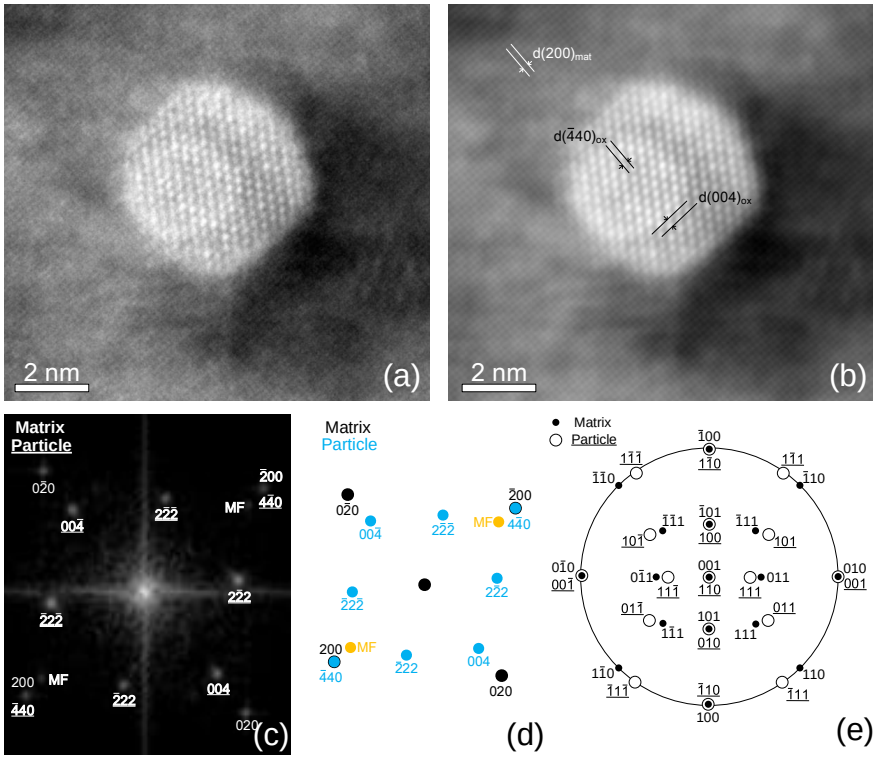

Figure 4.2: Coherency I: $(200)_{mat} \parallel (\bar{4}40)_{ox}$, $[001]_{mat} \parallel [110]_{ox}$: (a) HR-TEM image; (b) contrast enhanced FFT-IFFT image of (a); (c) FFT of HR-TEM image; (d) simulated FFT diffraction pattern of Coherency I; (e) stereogram of Coherency I.

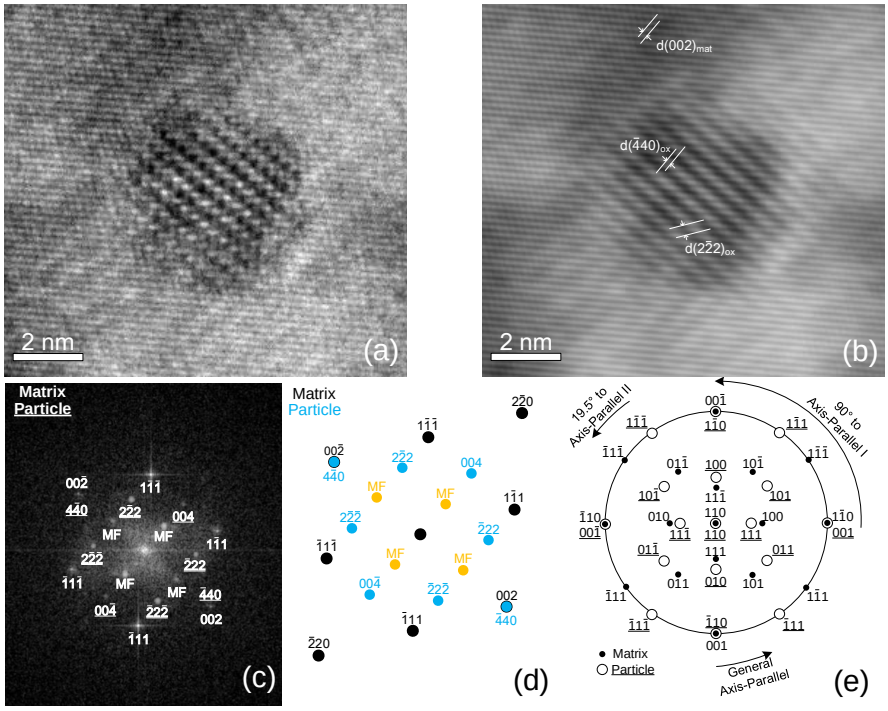

Figure 4.3: Coherency II: $(002)_{mat} \parallel (\bar{4}40)_{ox}$, $[110]_{mat} \parallel [110]_{ox}$: (a) HR-TEM image; (b) contrast enhanced FFT-IFFT image of (a); (c) FFT of HR-TEM image; (d) simulated FFT diffraction pattern of Coherency II; (e) stereogram of Coherency II.

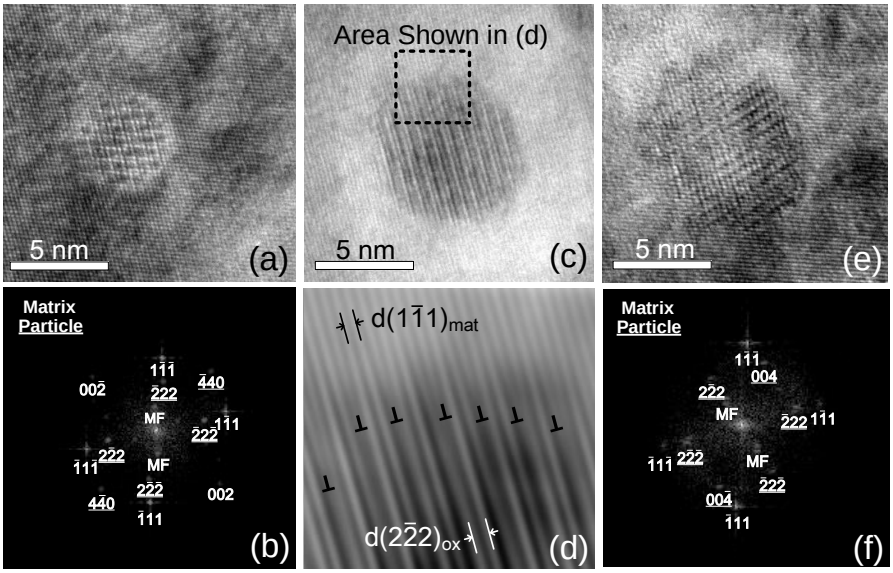

Figure 4.4: Axis-Parallel: $[110]_{mat} \parallel [110]_{ox}$: (a) HR-TEM image of the cubic-on-cubic relation (labeled as Axis-parallel I); (b) FFT of (a); (c) another HR-TEM image of the cubic-on-cubic relation; (d) contrast enhanced FFT-IFFT image of (c) showing misfit dislocations; (e) special axis-parallel relation with only one $\langle 111 \rangle_{mat} \parallel \langle 111 \rangle_{ox}$ (labeled as Axis-parallel II); (f) FFT of (e).

I). Here, the $[110]_{ox}$ axis and the $[001]_{mat}$ axis, which are the zone axes in Fig. 4.2, are parallel. Also, the $(\bar{4}40)_{ox}$ planes are parallel to the $(200)_{mat}$ planes, according to the overlapped diffraction spots in the FFT pattern (Fig. 4.2(c)). The other type of coherency mechanism (labeled as Coherency II) is shown in Fig. 4.3. Here, the zone axes of both the particle and the matrix are [110] with overlapping $(\bar{4}40)_{ox}$ and $(002)_{mat}$ spots. The spots in Fig. 4.2(c) and (d) labeled by "MF" correspond to the Moiré fringes formed by the $\{020\}_{mat}$ and $\{222\}_{ox}$ reflections. Likewise, the Moiré fringes shown in Fig. 4.3(c) and (d) (labeled by "MF") are due to the $\{111\}_{mat}$ and $\{222\}_{ox}$ reflections. The orientation and spacing of these Moiré fringes can be predicted precisely by the following equations: $D = d_1 d_2 / \sqrt{d_1^2 + d_2^2 - 2 d_1 d_2 cos\alpha}$ and $\Theta = arcsin\left(d_1 sin\alpha \Big/ \sqrt{d_1^2 + d_2^2 - 2 d_1 d_2 cos\alpha}\right)$; where d_1 and d_2 are the d-spacings of the two atomic fringes; α is the angle between them; D is the spacing of the double diffraction fringes; and Θ is the angle between d_1 and D.

For the condition $[110]_{mat} \parallel [110]_{ox}$, the $(00\bar{2})_{mat}$ and $(\bar{4}40)_{ox}$ are not always

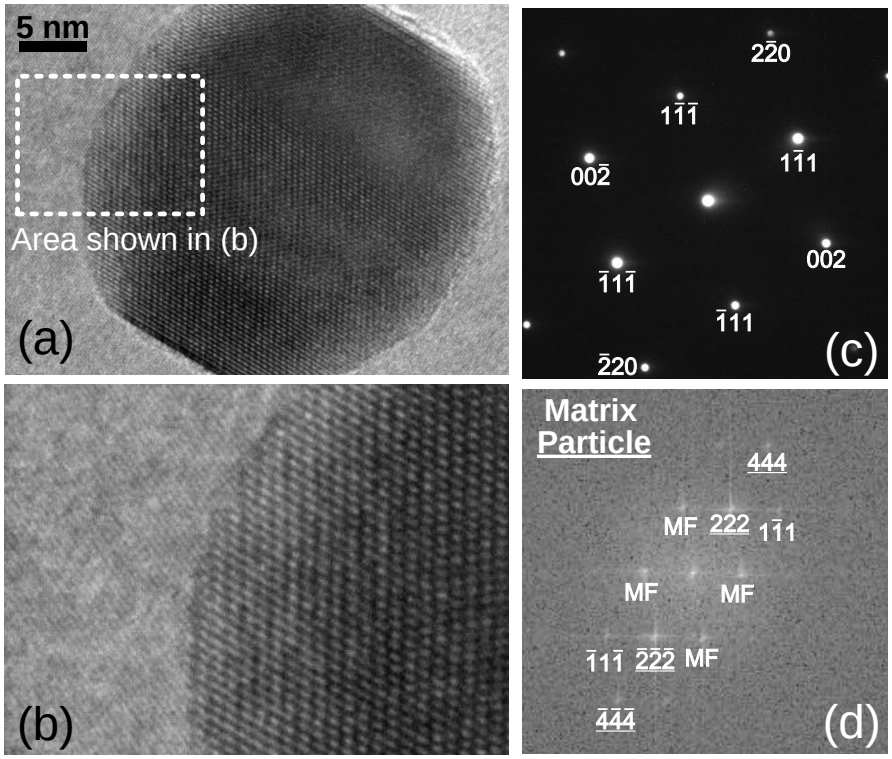

Figure 4.5: A large nanoparticle with random orientation: (a) HR-TEM image of a large nanoparticle (32nm); (b) magnification of the interface shown in (a); (c) electron diffraction pattern of the matrix in (a) showing the [110] zone; (d) FFT of the nanoparticle part of (a) showing diffraction spots from the matrix, the nanoparticle and Moiré fringes.

necessarily parallel. In the case that they are not, the nanoparticle and the matrix lack a pair of parallel planes with similar d-spacings, which makes this orientation relationship unqualified for a coherency mechanism. In fact, this orientation relationship is semi-coherent considering the fact that the lattice parameter of the pyrochlore-related structure oxide is approximately three times as that of the austenitic matrix. Typically, the $[110]_{mat} \| [110]_{ox}$ axis-parallel also prefers to have one or two pairs of extra $\langle 111 \rangle_{mat} \parallel \langle 111 \rangle_{ox}$ parallel axes, which are shown in Fig. 4.4(a), (b) (labeled as Axis-Parallel I) and (e), (f) (labeled as Axis-Parallel II). When two pairs of $\langle 111 \rangle$ axes are parallel, the cubic-on-cubic relation is formed. For all the axis-parallel cases, there exist no parallel planes with close d-spacings. In addition, all the Moiré fringe spots (labeled "MF") can be predicted by the equations given above.

4.1.2 Size Dependence on Orientation Relationship

One hundred and ten randomly-selected oxide nanoparticles were categorized into four groups: Coherency I, Coherency II, axis-parallel, and random orientation versus their sizes. Statistical results are shown in Fig. 4.1(b). The smaller the oxide particles, the larger proportion that have a non-random orientation relationship with the matrix. When the particles are smaller than 4 nm, all exhibit a specific orientation relationship with the matrix. As the particle size increases to 20 nm, the probability of coherency or the axis-parallel relation becomes marginal. A typical large nanoparticle (32 nm) with random orientation is illustrated in Fig. 4.5. Among the three non-random orientation relationships, the axis-parallel relation always has the highest probability of existence, whereas Coherency I has the lowest.

The lattice constant of the strain-free Y-Ti-Hf-O nanoparticles, $Y_2Hf_2O_7$, $Y_2Ti_2O_7$, Y_2O_3, HfO_2, and Y_2TiO_5, are shown in Table 4.1. The information of more complex oxide phases, such as Y_2O_3-HfO_2 solid solution and $Y_2(Ti,Hf)_{2-x}O_{7-2x}$, can also be assessed referring to Table 4.1. Due to the different chemical composition groups and various Hf/Ti values, the (equivalent pyrochlore) lattice constants could vary from 10.090 Å to 10.600 Å, which explains the abnormal broadening of the Y-Ti-Hf-O peaks in Fig. 3.5,

Table 4.1: Lattice parameters of the complex oxides related to Y-Ti-Hf-O inclusion phases

Phase	Structure	a_0 (Å)	equivalent pyrochlore a_0 (Å)	Reference
$Y_2Hf_2O_7$	fluorite	5.202	10.404	[39]
$Y_2Ti_2O_7$	pyrochlore	10.090	10.090	[103]
Y_2O_3	bixbyite	10.600	10.600	[105]
HfO_2	fluorite	5.120	10.240	[106]
Y_2TiO_5	pyrochlore	10.256	10.256	[100]

which can not be explained merely by the size broadening. Several similar d-spacings were found between the oxide nanoparticle and the steel matrix. d^{mat}_{200}=1.798 Å is close to d^{ox}_{440}=1.784∼1.874 Å, whereas d^{mat}_{110}=2.542 Å is similar to d^{ox}_{400}=2.523∼2.650 Å. Thus, Coherency I actually includes four sets of parallel planes ($(200)_{mat} \parallel (\bar{4}40)_{ox}$; $(101)_{mat} \parallel (040)_{ox}$; $(\bar{1}01)_{mat} \parallel (400)_{ox}$; $(002)_{mat} \parallel (440)_{ox}$) whereas Coherency II includes two sets of parallel planes ($(002)_{mat} \parallel (\bar{4}40)_{ox}$; $(1\bar{1}0)_{mat} \parallel (004)_{ox}$). The axis-parallel relation does not involve any parallel planes with close d-spacings. For the special cases of axis-parallel, Axis-Parallel I is a cubic-on-cubic relation which has been reported by Oka et al. [39]. However, the misfits (δ) in all parallel d-spacings are as large as 0.4, which implies the incoherent orientation relation and the dense misfit dislocations as shown in Fig. 4.4 (d). When only one $\langle 111\rangle_{mat} \parallel \langle 111\rangle_{ox}$ relation exists (Axis-Parallel II), the particles may suffer a large asymmetric strain field due to the large misfit, showing distorted FFT diffraction patterns, Fig. 4.4(f).

Assuming identical elastic moduli for the matrix and the inclusion, the free energy of a randomly-oriented spherical nanoparticle only contains the interface energy, $4\pi r^2\gamma_r$. The formation of coherent orientation relationships reduce the areal interface energy to $4\pi r^2\gamma_c$ by introducing an additional volumetric strain energy, $(4\pi r^3/3)\cdot 4\mu\delta^2$ [54]. Here, r is the nanoparticle radius; γ_r and γ_c are the unit areal energies of randomly-oriented and coherent interfaces, respectively, $\gamma_r > \gamma_c$; μ is the shear modulus and δ is the misfit. A similar phenomenon occurs in the axis-parallel relation when misfit dislocations form on the interface, lowering the interface energy by accommodating the strain energy. Actually, the elastic moduli of the matrix and the nanoparticles usually differ a lot, but the fundamental physics of the competition between the interface energy and the strain energy remains the

same. Hence, thermodynamically, the coherency and the axis-parallel relations are only favored for small nanoparticles, whereas random orientations are preferred for large nanoparticles.

The formation mechanism of oxygen-enriched precipitates in ODS steels has been studied for years. It is widely believed that the originally added Y_2O_3 powders are dissolved during ball milling and that the oxygen-enriched nanoparticles precipitate during the post-milling annealing procedure[42, 43, 44, 45]. According to Ref. [42], the precipitation initiates from the amorphous oxygen-enriched regions formed during ball milling. The formation of these amorphous regions is actually a consequence of the diffusion of dissolved Y_2O_3 as well as those metal elements that have high affinity for oxygen such as Ti and Hf. In bcc ferrite, these amorphous regions may simply be a disordered structure formed due to the energy preference of O_i-vacancy pairs in the presence of Ti[81]. The size and chemical composition evolution of the amorphous regions is therefore driven by the chemical potential and also kinetically limited by local distribution of Y, Ti, Hf ,and O atoms. The properties of these amorphous regions then determine the size and chemical composition of nanoparticles crystalized during annealing. The addition of Hf may increase the complexity of the formation of amorphous regions, which results in the existence of three separate oxygen-enriched phases. The chemical compositions of extremely small nanoclusters are frequently deviated from stoichimetric, causing the difficulties in crystallization[107]. Otherwise, for small amorphous regions, the coherent or axis-parallel orientation relation is selected during the crystallization process due to the preference in energy. Meanwhile, large randomly-orientated nanoparticles are formed to avoid the high strain energy due to strong interfacial coupling. No prominent shell structure was found in these nanoparticles.

Although Coherency I involves four pairs of parallel planes and Coherency II involves only two pairs, they should have the same elastic energy if both the matrix and the inclusion phases have isotropic elastic properties. However, both austenite and complex Y-Ti-Hf-O phases have anisotropic elastic properties (e.g., Zener's elastic anisotropy constant $A_{Y_2Ti_2O_7}$=2.11, A_{SS316}=3.78)[108, 109]. Therefore, Coherencies I and II have different strain energies, which can explain why Coherency II was observed more frequently than Coherency I. In addition, the variation of the nanoparticles' lattice constants due to

the diverse chemical compositions influences the strain field of the coherent nanoparticles. This factor should also be considered in the explanation of the relative ratio of different orientation relations.

The small oxide nanoparticles in the hafnium-containing ODS 316 stainless steel were observed to have a significant probability of holding coherency or axis-parallel orientation relations with the matrix. Hence, the stress fields of these nanoparticles could enhance the mechanical strength and the radiation resistance performance[51, 52]. As the nanoparticles are the consequences of crystallization of the amorphous oxygen-enriched regions that were formed during ball milling, the properties of these nanoparticles, including size, chemical composition and orientation, are believed to be quite stable at elevated temperature. Differences in thermal expansion properties between the nanoparticles and the matrix could cause the stress field as well as the strain energy of the coherent/axis-parallel interfaces to vary with temperature. Therefore, the radiation resistance and the mechanical strengthening properties of ODS steels would depend highly on their operating temperature, which is worth further investigation.

4.2 ODS 304 Stainless Steel

As electropolishing tends to preferentially corrode the fine precipitates in the ODS 304 steel, probably due to the low nickel content, only a limited number of oxide nanoparticles are capable of surviving the electropolishing at the thin areas of the TEM specimens that qualify for HRTEM observation. Still, the cubic-on-cubic orientation relationship was found to be common, as shown in Fig. 4.6. Although no coherent relationships were directly observed in ODS 304, they might still exist considering the limited amount of nanoparticles that have been investigated.

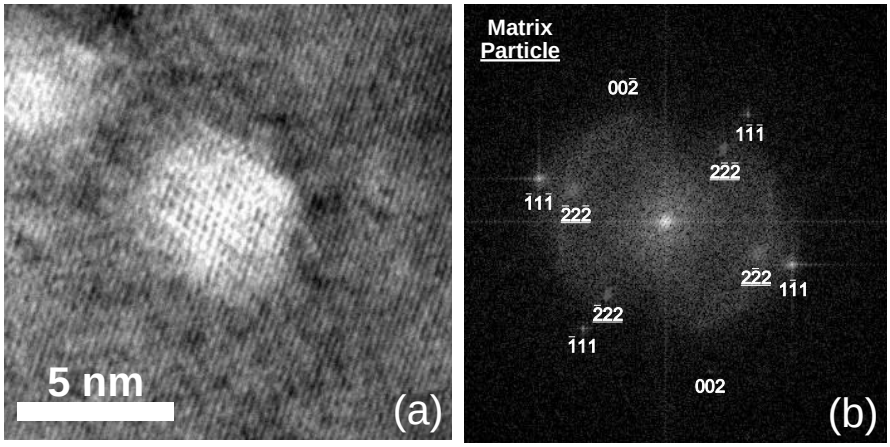

Figure 4.6: Cubic-on-cubic orientation relationship; (a) an HRTEM image of a $Y_2Ti_2O_7$ nanoparticles with cubic-on-cubic relationship; (b) FFT of (a) showing the diffractions due to both matrix and the particle.

4.3 ODS 316 Stainless Steel

The orientation relationship of the nanoparticles not only determines the magnitude of the strain field due to the nanoparticles, but also influences their interactions with dislocations[53]. The orientation relationship is governed by the competition between the areal interface energy and volumetric strain energy. Therefore, large nanoparticles usually have random orientation relationship, whereas small nanoparticles tend to maintain a coherent or cubic-on-cubic orientation relationship with the matrix.Since $YAlO_3$ precipitates (YAP and YAH) are relatively large, their orientation relationship is random. Two orientation relationships were observed for $Y_2Ti_2O_7$, one of which is the $(002)_{mat} \parallel (\bar{4}40)_{ox}$, $[110]_{mat} \parallel [110]_{ox}$ coherent relationship shown in Fig. 4.7, while the other is the cubic-on-cubic relationship shown in Fig. 4.8. Both of these orientation relationships have been reported in the hafnium-containing ODS 316 steel with pyrochlore/fluorite Y-Ti-Hf-O precipitates[40], implying that they are common orientation relationships in austenitic ODS steels. However, another coherent relationship that was reported in the Hf-containing ODS 316, $(200)_{mat} \parallel (\bar{4}40)_{ox}$, $[001]_{mat} \parallel [110]_{ox}$, was not observed in this materials. The existence of these orientation relationships causes the interfaces between nanoparticles and the matrix to be strong sinks for point defects, enhancing the radiation tolerance of the ODS material. In addition, these orientation relationships allow the disloca-

tions to cut through the nanoparticles when the nanoparticle is sufficiently small.

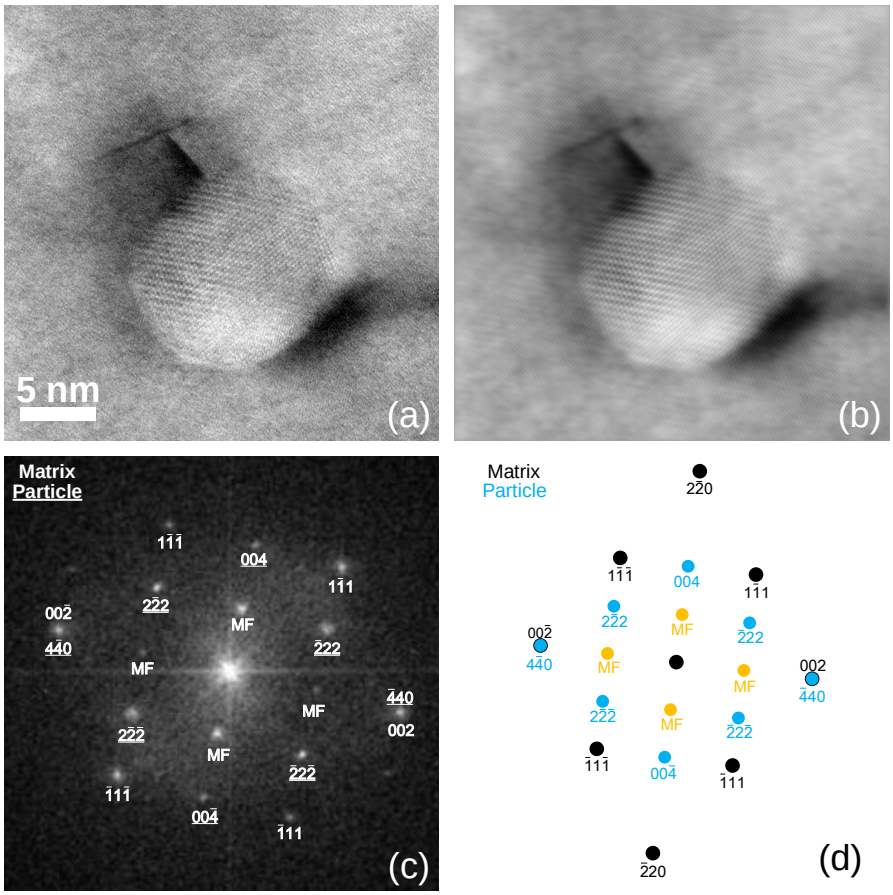

Figure 4.7: Coherent orientation relationship:
$(002)_{mat} \parallel (\bar{4}40)_{ox}$, $[110]_{mat} \parallel [110]_{ox}$; (a) an HRTEM image of a $Y_2Ti_2O_7$ nanoparticle with coherent orientation relationship; (b) an FFT-IFFT enhanced contrast image of (a); (c) FFT of (a) showing the diffractions due to both the matrix and the particle; and (d) theoretically predicted FFT diffraction pattern. The spots labelled by "MF" correspond to the Moiré fringes formed due to the overlap of the matrix and the nanoparticle.

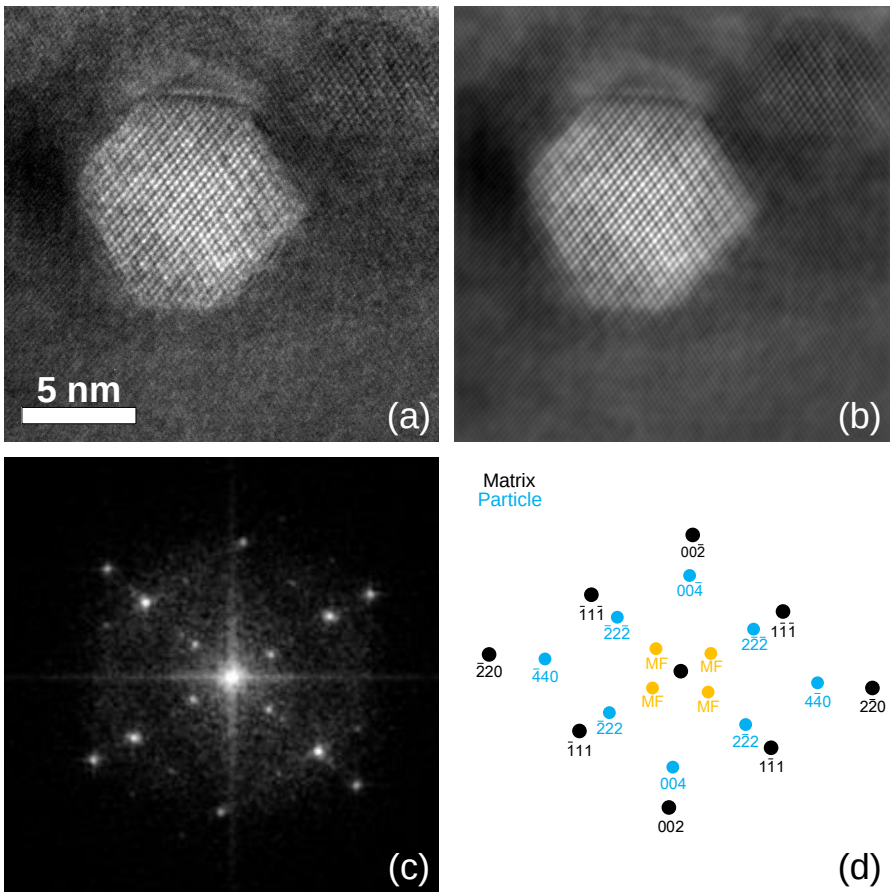

Figure 4.8: Cubic-on-cubic orientation relationship; (a) an HRTEM image of two $Y_2Ti_2O_7$ nanoparticles with cubic-on-cubic relationship; (b) an FFT-IFFT enhanced contrast image of (a); (c) FFT of (a) showing the diffractions due to both matrix and the particle; and (d) FFT diffraction pattern from theoretical prediction. The spots labelled by "MF" correspond to the Moiré fringes formed due to the overlap of the matrix and the nanoparticles.

CHAPTER 5

NANOPARTICLE-DISLOCATION INTERACTION MECHANISMS

With the knowledge of the nanoparticle morphology, including their size distribution, density and orientation relationship, the nanoparticle-dislocation interaction mechanisms can then be analyzed. Hence, *in-situ* TEM deformation investigations were performed to experimentally explore the nanoparticle-dislocation interactions. The hafinium-containing ODS 316 steel was selected to be the representative of austenitic ODS steels for the nanoparticle-dislocation interaction examinations. The consistence between the theoretical deduction and experimental observation was then examined to help understand the enhancement of the mechanical strength due to the nanoparticles.

5.1 The Orowan-Shearing Competition

Equations 1.2 and 1.3 provide the analytic expressions of the CRSSs of the Orowan looping and shearing mechanisms. The Orowan looping occurs as its CRSS is lower than that of the shearing mechanism, namely,

$$\tau_{Orowan} < \tau_{shearing}, \tag{5.1}$$

which yields the following inequality according to Equations 1.2 and 1.3:

$$\frac{1}{L} > \frac{1}{b} e^{-\frac{2\pi\sigma_m B}{Gb\delta}} - \frac{1}{d}. \tag{5.2}$$

In FCC metals, the primary slip system is $\{111\}\langle\bar{1}10\rangle$. Therefore, perfect dislocations in austenitic stainless steel have Burgers vectors $\mathbf{b}=1/2\langle\bar{1}10\rangle$. In some FCC materials such as 304 and 316 stainless steels, the SFE is so low

(around 20 mJ/m^2 and 30 mJ/m^2, respectively)[110] that the dissociation of perfect dislocations into partial dislocations is common. In this case, the dislocation reaction takes place as follows:

$$\frac{1}{2}\langle\bar{1}10\rangle \rightarrow \frac{1}{6}\langle\bar{1}2\bar{1}\rangle + \frac{1}{6}\langle\bar{2}11\rangle. \tag{5.3}$$

Namely, a perfect dislocation dissociates into two Shockley partials with a stacking fault region between them (see Fig. 2.11). In austenitic stainless steel such as 316 steel, the separation between two partials δ can be calculated according to Byun's equation[111]:

$$\delta = \frac{1}{8\pi}\frac{(2-3\nu)}{(1-\nu)}\frac{Gb_p^2}{[\gamma_{SF} - \tau b_p/2]}. \tag{5.4}$$

Given the shear modulus G=78.8 GPa[112], Poisson ratio ν=0.294[113], stacking fault energy γ_{SF}=30 mJ/m^2[110], the length of the Shockley partial dislocation's Burgers vector b_p=1.468$\mathring{A}$, and resolved shear stress τ=σ_y/T=163 MPa at yielding (σ_y is the yield stress, and T=3.06 is the Taylor factor[114]), the calculated value of δ is 5.9 nm. Therefore, the B parameter in Equation 1.3 has the following form:[57]

$$B = \begin{cases} \frac{1}{4}\pi d^2 & d \leq \delta \\ \frac{1}{8}[2\pi - 2\omega + sin(2\omega)]d^2 & d > \delta, \end{cases} \tag{5.5}$$

with

$$\omega = arccos(\frac{2\delta}{d} - 1). \tag{5.6}$$

Using all the involved parameters and equations mentioned above, numerical calculation shows that the right-hand side (RHS) of Inequlity 5.2 is negative regardless to the value of d as σ_m is larger than 68.6 GPa. That is, the shearing mechanism is unlikely to occur once the particle phase is hard enough. For the oxide nanoparticles in the ODS 316 steel that is investigated in this study, a good reference for the σ_m value is the CRSS in Y_2O_3, which is 8 GPa[115]. Assume σ_m=8 GPa, the Inequality 5.2 gives the boundary between the Orowan domain and the shearing domain (orange curve) in Fig.

5.1.

The L-d space can then be divided into four regimes, as shown in Fig. 5.1. When the nanoparticle is large enough ($d \geq$2.7 nm), the Orowan mechanism is always dominant since the RHS of Inequlity 5.2 is negative. This part of the Orowan domain, which involves large nanoparticle size, is defined as Regime I. On the other hand, when the nanoparticle is small enough ($d \leq$2.1 nm), the shearing mechanism is always favored as Inequality 5.2 requires the unphysical condition $L < d$. This part of the shearing domain, which involves small nanoparticle size, is defined as Regime IV. As the nanoparticle size is intermediate (2.1 nm$< d <$2.7 nm), there exists a critical particle spacing L_c. When the particle separation is sufficient ($L > L_c$), the shearing mechanism is dominant (Regime III). Otherwise the Orowan mechanism is preferred, which accounts for the rest part of the Orowan domain (Regime II). The areas of interest in the *in-situ* TEM deformation investigations were carefully selected to cover those L-d regimes mentioned above so that a comprehensive understanding of the nanoparticle-dislocation interaction can be established.

5.2 The Orowan Looping Mechanism

5.2.1 Large Nanoparticles

When the nanoparticles are large ($d \geq$ 2.7 nm), Orowan looping is preferred (Regime I). As the CRSS of Orowan looping, τ_{Orowan}, is high when the nanoparticle spacing L is limited, it is easier to observe the Orowan looping mechanism when the nanoparticle distribution is sparse. Therefore, once the dislocation channel is activated in a region with a sparse distribution of large nanoparticles, as shown in Fig. 5.2, there are chances that a nanoparticle will be on the slip plane. As a result, the dislocations bypass the nanoparticle through the Orowan looping mechanism. When a dislocation is dissociated, the Orowan bypassing mechanism depends on the nature of the dislocation according to atomistic simulations[57]. When the dislocation is a pure screw dislocation, the two Shockley partials rejoin before

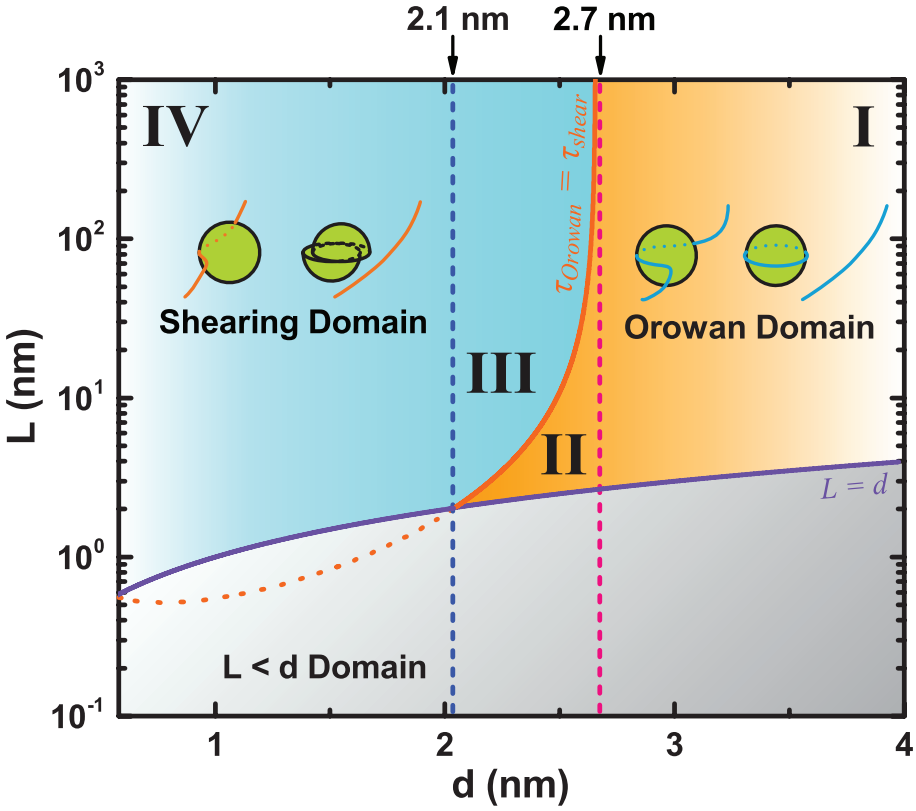

Figure 5.1: Competition between the Orowan looping and the shearing mechanisms: the orange $\tau_{Orowan} = \tau_{shearing}$ curve indicates the boundary between the Orowan domain and the shearing domain.

bypassing the nanoparticle. On the other hand, when the dislocation is a pure edge dislocation, the leading and tailing partial dislocations successively bypass the nanoparticle separately. In Fig. 5.2, it is clear that the leading partial first bypasses the nanoparticle (P1), and then the tailing partial circumvents the P1 nanoparticle after 22 seconds, implying that the dislocations involved are edge dislocations. More importantly, after the dislocation bypasses the P1 nanoparticle, a dislocation loop can be observed circling the nanoparticle (50 seconds), which is direct evidence of the occurrence of Orowan looping. There is another large nanoparticle (P2) in the same slip channel. The dislocation also bypasses the P2 nanoparticle through Orowan looping, leaving another dislocation loop (334 seconds). Afterwards, the bypassed nanoparticles are circulated by dislocation loops. In the Orowan looping mechanism, a nanoparticle circulated by one or several dislocation loops is equivalent in obstacle strength to a nanoparticle of larger size. Because the larger nanoparticle has a higher CRSS value, bypassing of successive dislocation becomes more difficult. In this case, the dislocation channel, due to the build-up of Orowan loops, was finally deactivated once the dislocations were no longer capable of bypassing the nanoparticle. Although the nanoparticle-loop(s) complex acts as a nanoparticle of larger size in the Orowan looping mechanism, the nanoparticle-dislocation interaction is different when the nanoparticle is surrounded by one or several Orowan loops. A dislocation stopped by a nanoparticle with a preexisting Orowan loop has an asymmetric shape, as shown in Fig. 5.2 (334 seconds), implying the interaction between the dislocation and the Orowan loop. As predicted by Proville and Bakó's simulation[57], two jogs are formed in the course of the bypassing of the second edge dislocation. The asymmetry in Fig. 5.2 is due to the dislocation-Orowan loop interaction that forms the first jog, and has a shape exactly identical to that described in Ref. [57], as shown in Fig. 5.4.

5.2.2 Dense Distribution of Small Nanoparticle

When the nanoparticles are intermediate in size (2.1 nm $< d <$ 2.7 nm), and the spacing between them is also small (around tens of nm), Orowan looping is again favored (Regime II). Hence, the Orowan looping mechanism

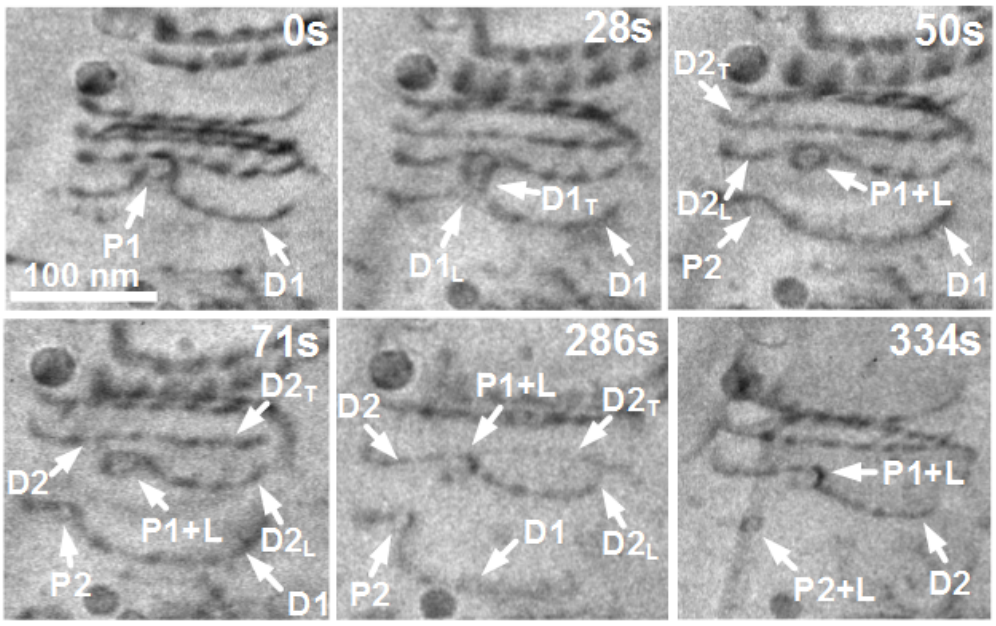

Figure 5.2: Orowan looping of large and sparse nanoparticles (Regime I): 0 s) a dislocation (D1) is anchored by a nanoparticle (P1); 28 s) D1 dissociates, and the leading partial ($D1_L$) bypassed P1 while the tailing partial ($D1_T$) continues to be stopped; 50 s) $D1_T$ bypasses P1, leaving an Orowan loop (L), and then re-associates with $D1_L$ to recover D1. D1 is stopped by another nanoparticle (P2) while a dissociated dislocation, $D2_L$ and $D2_T$, is stopped by P1+L; 71 s) Half of the dissociated dislocation ($D2_L$ and $D2_T$) re-associates to D2, while the rest continues to be separate; 286 s) the P2-D1 interaction continues as the bowing of D1 increases; 344 s) the entire perfect dislocation D2 is recovered due to the existent of P1, forming a unique shape with P1+L, while D1 bypasses P2 through Orowan looping, leaving a dislocation loop around P2 (P2+L).

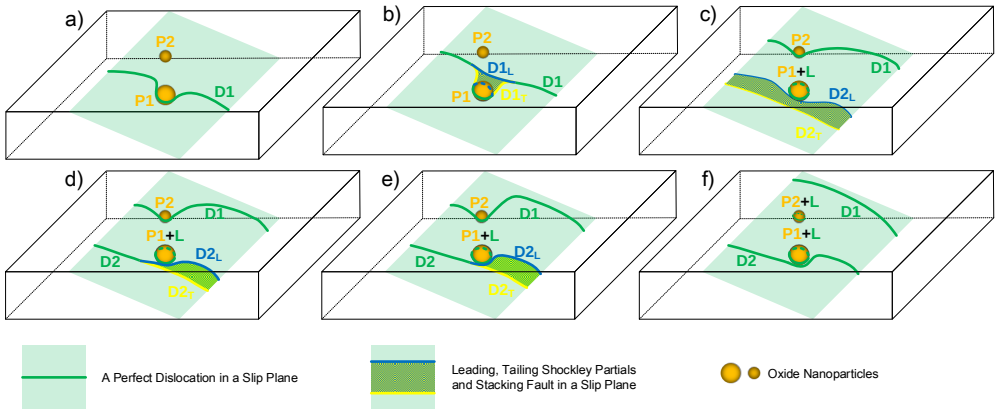

Figure 5.3: Demonstration of Orowan looping of large and sparse nanoparticles (Regime I): the description of each stage is exactly corresponding to that in the caption of Fig. 5.2

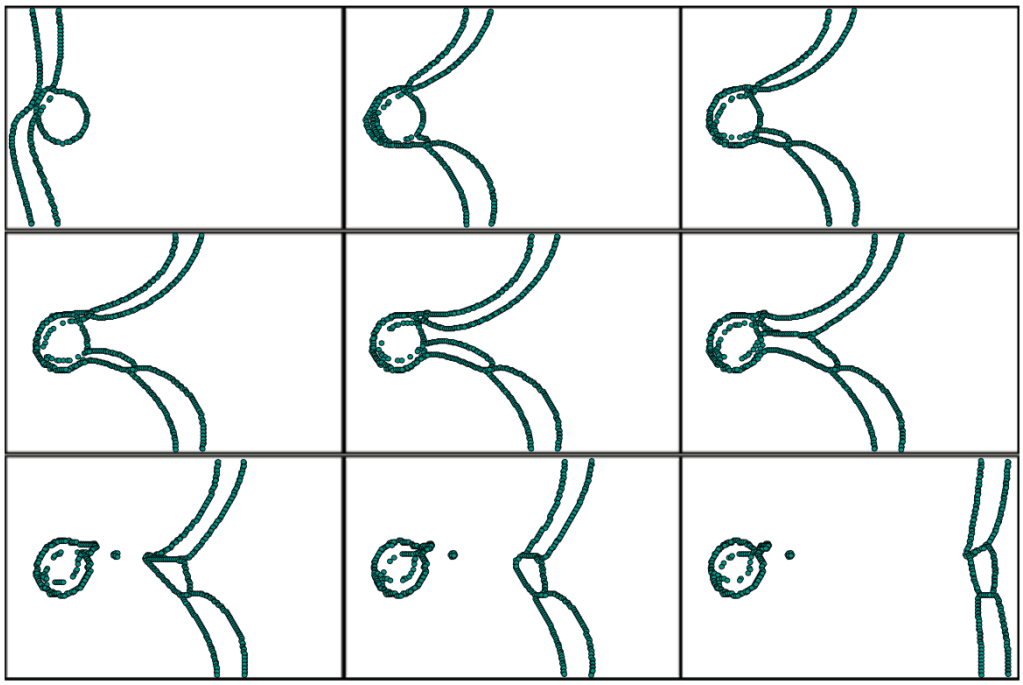

Figure 5.4: Simulation results of an edge dislocation interacting with a particle-loop complex[57].

also dominates the region with dense distributions of intermediate nanoparticles, as illustrated in Fig. 5.5. The absolute size of the "intermediate" nanoparticles is already too small to be distinguished in TEM diffraction contrast due to their limited size. Instead, indirect observation methods must be used to locate these nanoparticles. A relatively straight dislocation bows when it encounters a nanoparticle. The bowing-shaped dislocations can be used to determine the position of those nanoparticles that are difficult to distinguish in TEM bright field images. Therefore, tracking the shape of the dislocations is an efficient mean of monitoring nanoparticle-dislocation interactions. Fig. 5.5 illustrates the interaction between dislocations and multiple intermediate nanoparticles. The circles in the figure indicate the positions of the nanoparticles as identified by indirect observation. As shown in Fig. 5.5, when the spatial number density of intermediate nanoparticles is high, a dislocation is stopped by a series of obstacles simultaneously, even in thin electron transparent regions of TEM samples. This indicates the collective strength of a field of obstacles. The activated dislocation slip channel is also suppressed towards the end of the experiment (402.5 seconds), which implies that Orowan looping is the interaction mechanism.

5.3 The Shearing Mechanism

Given the fact that the nanoparticles smaller than 4 nm are assured to have have coherence or cubic-on-cubic relationships with the matrix, the shearing mechanism dominates the nanoparticle-dislocation interaction when the intermediate nanoparticles (2.1 nm $< d <$ 2.7 nm) have an adequate spacing (Regime III), or the nanoparticle size is sufficiently small ($d \leq$2.1 nm, Regime IV). As mentioned previously, intermediate and small nanoparticles ($d <$ 2.7 nm) are very difficult to directly distinguish in TEM diffraction contrast images. This resolution limitation also makes it impossible to distinguish Regimes III and IV. So the two regimes in the shearing domain were investigated and discussed together. Even for Regime IV, where shearing is dominant no matter how large the particle spacing L is, large L still yields lower $\tau_{shearing}$, providing greater opportunity of observing the shearing mechanism. Therefore, we focused on the areas with sparse distribution of

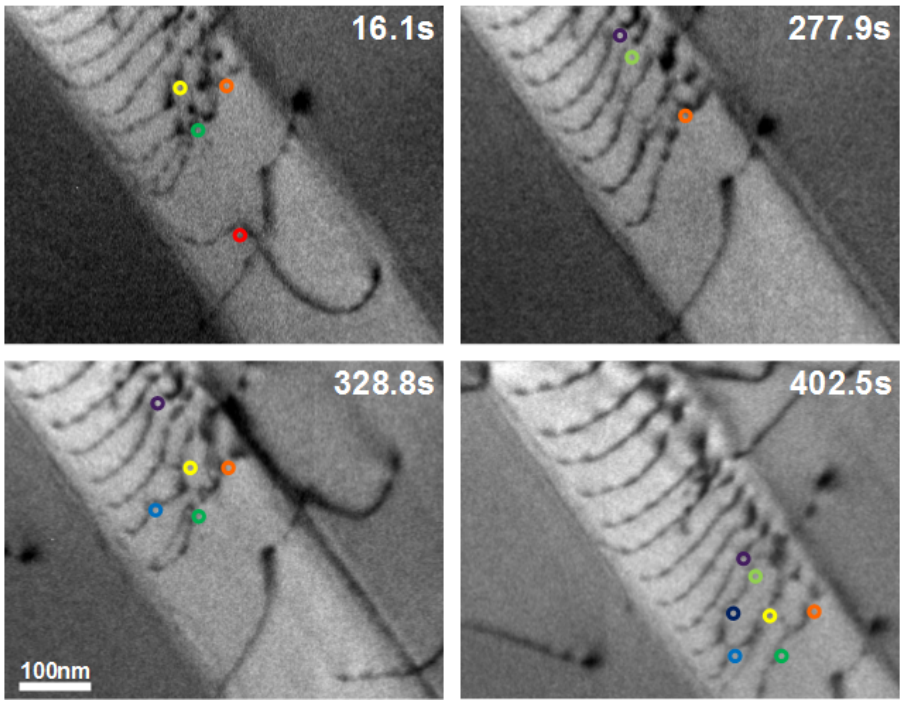

Figure 5.5: Orowan looping of intermediate and dense nanoparticles (Regime II): the positions of the intermediate nanoparticles were determined according to the bowing of dislocations and are marked by chromatic circles. The same nanoparticles are marked by the same colors.

intermediate or small nanoparticles to investigate the shearing mechanism. Although the bowing of dislocations can reveal the position of the small nanoparticles, the characterization of the nanoparticle-dislocation interaction mechanism requires more advanced methodologies. Using the *in-situ* TEM deformation technique, it is feasible to record the real-time evolution of the dislocation positions during the nanoparticle-dislocation interaction. The position changes of successive dislocations help reflect the nature of the nanoparticle-dislocation interaction. When four small nanoparticles exist in an active slip channel, as shown in Fig. 5.6, dislocations bypass the nanoparticles one after another. The positions of the four nanoparticles, which were determined by the bowing of dislocations, are marked by circles with different colors, whereas the active slip channel is marked by two yellow dashed lines that correspond to the edges of the slip plane as defined by the upper and lower surfaces of the TEM specimen . The s-axis of the diagram in Fig. 5.6 is defined by the positions of the dislocations on the left edge of the slip channel. The starting point of the s-axis is another slip channel (blue straight dashed line), while the end point corresponds to a grain boundary (blue curve). The position changes of three successive dislocations were recorded and is shown in Fig. 5.6. The regions that demonstrate the dislocations being stopped by nanoparticles are highlighted by blocks with different colors. It is clear that each nanoparticle is capable of stopping the dislocations for some period of time. For all the four nanoparticles involved, the time duration of the stopping ability continued to decrease. This implies that the nanoparticle-dislocation interaction mechanism in this case is shearing, since shearing lowers the CRSS of a nanoparticle each time when a dislocation cuts through the particle[116] (see Fig. 5.8).

A more reliable way to prove the existence of the shearing mechanism is the escape speed measurement of a dislocation immediately after it bypasses a nanoparticle. The velocity of a dislocation is positively dependent on the resolve shear stress. The relationship is expressed as, $v = (\tau/\tau_0)^m$, where v is the velocity, τ is the resolved shear stress, and τ_0 and m are characteristic parameters of material[117]. Therefore, the escape speed of a dislocation bypassing a nanoparticle is positively correlated to the CRSS of the nanoparticle. Thus, measuring the escape speed of the dislocations can directly reveal the changes in the CRSS of a nanoparticle before and after it is sheared by

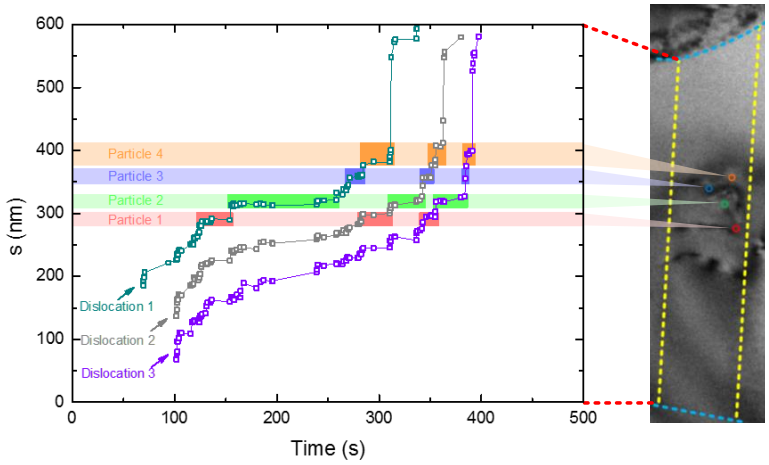

Figure 5.6: Shearing mechanism (Regimes III and IV)

a dislocation bypass event. Unfortunately, if a dislocation is stopped by another nanoparticle immediately after it bypasses a certain nanoparticle, it is impossible to measure the accurate escape speed of the dislocation due to this interference. For this reason, only the escape speed of the dislocation that interacted with the last nanoparticle (particle 4 in Fig. 5.6) in the slip channel can be precisely measured for quantitative analysis, as shown in Fig. 5.7. The continued decrease of escape speed of dislocation undoubtedly indicates that the CRSS of the nanoparticle decreases as a dislocation cuts through it. Therefore, the nanoparticle-dislocation interaction is confirmed to be shearing.

5.4 The Hirsch Mechanism

Aside from the two common nanoparticle-dislocation interaction mechanisms, Orowan looping and shearing, the Hirsch mechanism has also been reported in metals and alloys. In the Hirsch mechanism, the dislocation bypasses the nanoparticle through a series of cross slips and leaves one or two prismatic dislocation loops around the nanoparticle. Fig. 5.9 shows a dislocation bypassing a large nanoparticle involving cross slip. After the dislocation was stopped by the nanoparticle (58.9 seconds), the upper part of

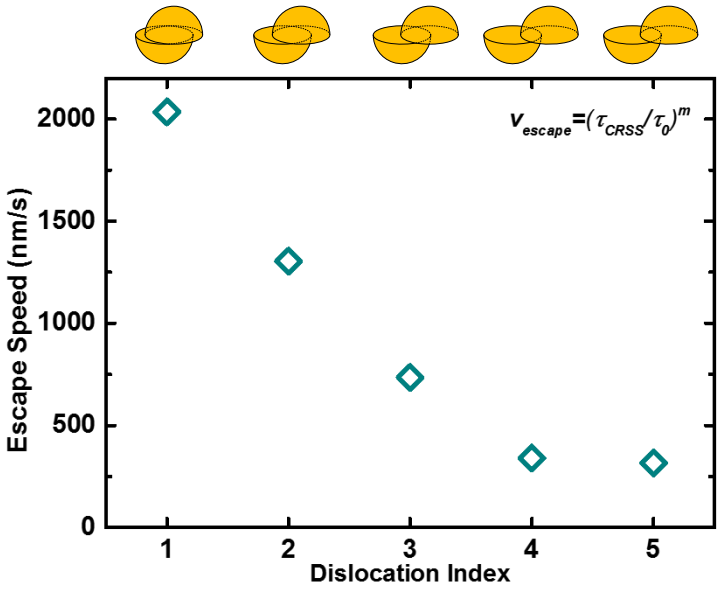

Figure 5.7: Escape speed of shearing dislocations: the escape speed decreases every time a dislocation bypassed the nanoparticle, implying that the CRSS of that nanoparticle continues to decrease.

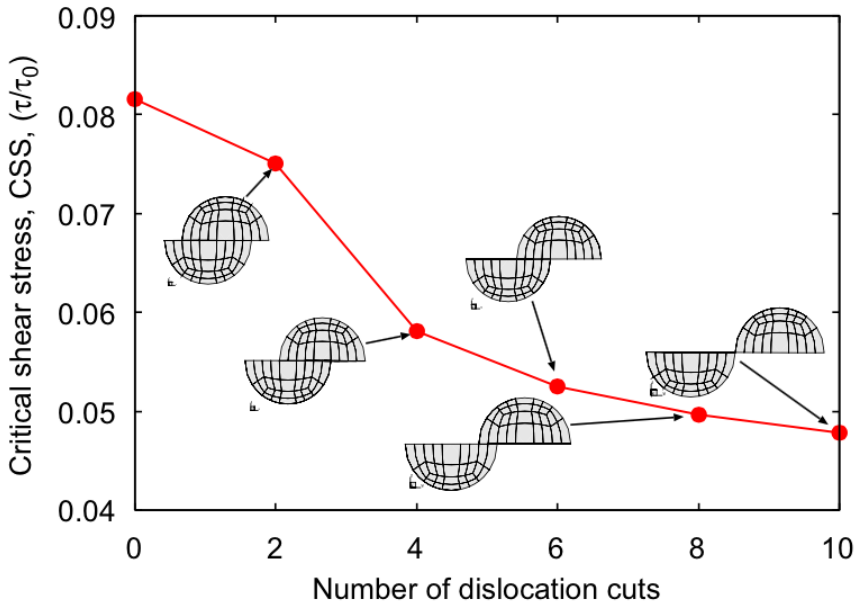

Figure 5.8: Simulation results of the CRSS of a sheared particle[116].

the dislocation changed its slip plane (120.5 seconds). Then the lower part of the original dislocation continued to bypass the nanoparticle (128.4 seconds and 131.7 seconds). Immediately after the bypassing, the lower dislocation actually remained in two different slip planes for a short while (131.7 seconds) and then returned to the slip plane of the original dislocation (131.8 seconds). The details are illustrated in Fig. 5.10. It is obvious that the conventional Hirsch mechanism of a screw dislocation is interrupted by the surface. Therefore, only half a prismatic dislocation loop is left around the nanoparticle. Hence, the Hirsch mechanism has been proven to exist in ODS 316 steel. However, due to the significant surface effect coupled with the ultra thin TEM sample (around 100 nm), the observation of the Hirsch interaction mechanism may be limited.

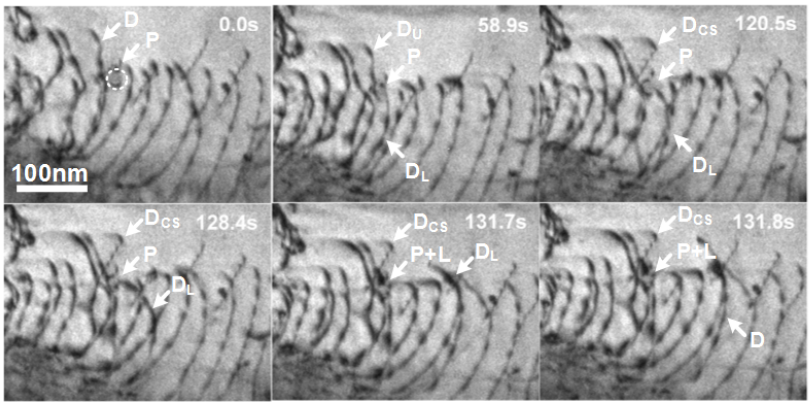

Figure 5.9: The Hirsch mechanism of large and sparse nanoparticles: 0.0 s) a dislocation (D) is approaching a large nanoparticle (P); 58.9 s) D is anchored by P and can be divided into the upper (D_U) and lower (D_L) parts; 120.5 s) D_U cross slips to another slip plane and becomes D_{CS}, while D_L continues to be stopped by P; 128.4 s) D_L moves forward but still anchored by P; 131.7 s) D_L bypasses P, leaves some dislocation/dislocation loop structure (L) on P. Part of D_L is still in another slip plane according to the position of its upper end; 131.8 s) D_L cross slips back to the original slip plane, and recovers to D.

5.5 Consequences of the Orowan Mechanism

As previously mentioned, shearing lowers the CRSS of a nanoparticle each time a dislocation cuts through the nanoparticle. As a result, the obstacle

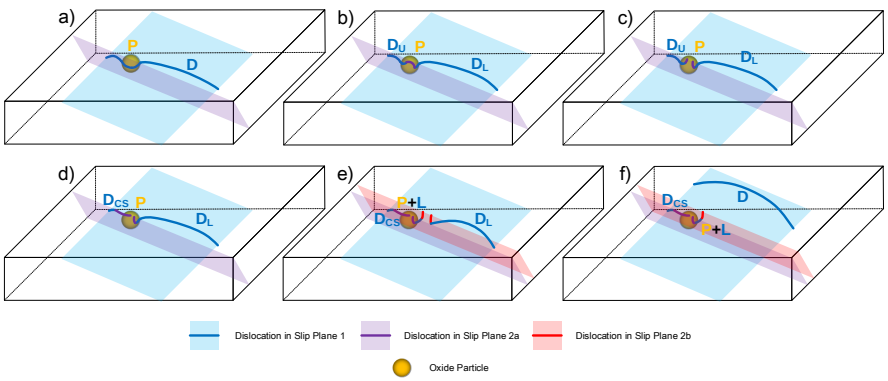

Figure 5.10: Demonstration of the cross slip that occurs in the Hirsch mechanism: a) a dislocation (D) is anchored by a nanoparticle (P); b) some part of D cross slips to another slip plane to bypass P, and D is divide into the upper (D_U) and lower (D_L) parts; c) the cross slipping part of D touches the surface due to the limited thickness of TEM samples; d) the majority of D_U cross slips into another slip plane, and becomes D_{CS}; e) D_L bypasses P through a series of cross slipping. A part of D_L still stay in another slip plane; f) the entire D_L comes back to the original slip plane, and D is then recovered.

strength of a nanoparticle continues to attenuate and the slip channel remains activated. On the contrary, the source shortening effect of Orowan looping increases the CRSS of the nanoparticle each time when a dislocation bypasses it, and as a result, the nanoparticle becomes more and more difficult to circumvent[118]. Therefore, the CRSS of a nanoparticle eventually exceeds the local resolved shear stress so that the successive dislocations can no longer bypass it. In this case, the grain boundary source will activate one or more new slip channels on the slip planes parallel to that of the original channel. This phenomenon was observed in the two cases that include the Orowan mechanism (see Figs. 5.11 and 5.12).

5.6 Prediction of the Enhancement of Yield Strength

The nanoparticle-dislocation interactions account for the strengthening of the materials. A series of models were established to quantitatively predict the enhancement in yield strength[119, 120, 121]. Assuming that the

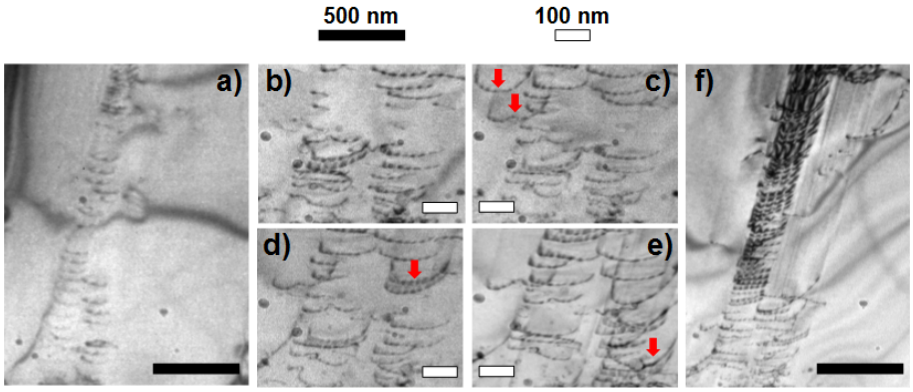

Figure 5.11: Consequence of Orowan looping, case one. Red arrows mark the newly activated slip channels: a) in the beginning of observation, only one slip channel is active; b) to e) multiple new slip channels are activated by the grain boundary source as the original active slip channel is suppressed by nanoparticles; f) in the end of observation, the original active slip channel is suppressed and filled with dislocation pile-ups, while the dislocation movement in new activated slip channels is significant.

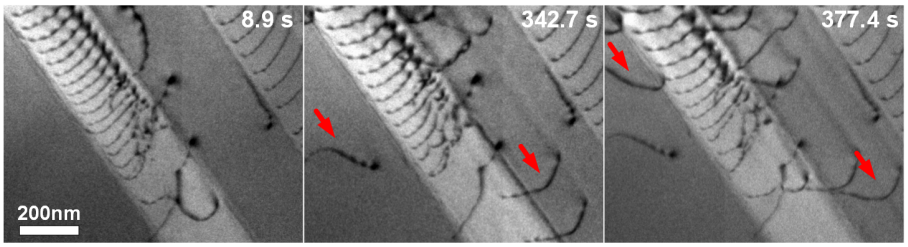

Figure 5.12: Consequence of Orowan looping, case two. Red arrows mark the newly activated slip channels: a) in the beginning of observation, only one slip channel is active; b) and c) multiple new slip channels are activated by the grain boundary source as the original active slip channel is suppressed by nanoparticles and filled with dislocation pile-ups.

nanoparticle-dislocation interaction is dominated by Orowan looping, the contribution of the nanoparticles to the yield strength, $\Delta\sigma_{Orowan}$, can be calculated using the equation developed by Kelly[122]:

$$\Delta\sigma_{Orowan} = \frac{0.83TGb}{(Nd)^{-1/2} - d} \frac{ln(d/b)}{2\pi(1-\nu)^{1/2}}, \tag{5.7}$$

where, T is the Taylor factor, which is 3.06 for polycrystalline materials[114], G is the shear modulus of the matrix, b is the length of the Burgers factor, N is the spatial density of the nanoparticles, d is the average diameter of the nanoparticles, and ν is the Poisson ratio of the matrix.

In addition to the nanoparticle strengthening, the ultra-fine grain size that was produced during the fabrication of ODS steels is another factor that influences the mechanical strength. As grain boundaries are effective obstacles to dislocation motion, the reduction of the grain size due to the mechanical alloying also helps strengthen ODS steels. This grain boundary strengthening effect, $\Delta\sigma_{HP}$, can be precisely described by Hall-Petch relationship[123, 124]:

$$\Delta\sigma_{HP} = kD^{-1/2} \tag{5.8}$$

where, k is a material characteristic coefficient, and D is the grain size. As multiple strengthening mechanisms contribute to the yield stress enhancement simultaneously, the simplest way to predict the increase of the yield stress might be the linear summation or product[119, 120] of the contributions of different strengthening mechanisms. However, the square root of the summation of the squares prove to be a more appropriate method to produce values that are consistent with the experimental results[125, 121]. Therefore, the yield stress, σ_y, can be calculated as follows:

$$\sigma_y = \sigma_0 + \sqrt{(\Delta\sigma_{Orowan})^2 + (\Delta\sigma_{HP})^2} \tag{5.9}$$

where, σ_0 is the intrinsic yield strength of the material.

All three major nanoparticle-dislocation interaction mechanisms were observed in the *in-situ* TEM deformation tests. shearing requires extremely small nanoparticle sizes and large spacings between nanoparticles, which are

just barely satisfied because the average nanopaticle size is around 10 nm and the nanoparticle density is fairly high. Meanwhile, the Hirsch mechanism is difficult to quantify, but holds a CRSS close to that of the Orowan looping mechanism. Therefore, Orowan looping should be the dominant nanoparticle-dislocation interaction mechanism. Assuming the statement is true, the theoretical improvement in the yield strength can be estimated using Equations 5.7 through 5.9. The nanoparticle size $d = 9.4$ nm was measured by the manufacturer, and confirmed by TEM observation in a previous study, while the spacial density of the nanoparticles $N = 6.6 \times 10^{21}$ m^{-3} was provided by the manufacturer, and also confirmed by synchrotron X-ray wide-angle scattering (WAXS)[40]. G and ν_m were chosen to be 78.8 GPa[112] and 0.294[113], respectively. The intrinsic material yield strength, σ_0 and Hall-Petch coefficiant, k, were selected to be 180 MPa and 164 MPa$\cdot\mu$m$^{-1/2}$[126]. The calculated $\Delta\sigma_{Orowan}$ is 296 MPa, whereas $\Delta\sigma_{HP}$ is 189 MPa, giving a predicted yield strength as 531 MPa. At this temperature, the yield strength of the ODS 316 steel has been measured to be 501 MPa. The consistence between the calculation and the experimental measurement implies that the Orowan looping is the dominant nanoparticle-dislocation interaction mechanism, and that the grain size reduction also plays an important role in the strengthening of the ODS 316 steel.

CHAPTER 6

IN-SITU SYNCHROTRON TENSILE INVESTIGATIONS

The elemental composition, morphology, and orientation relationship of the nanoparticles, along with their interaction mechanisms with the dislocations have been investigated in the previous chapters. Based on these results, the tensile property as well as the precipitate-strengthening effect of austenitic ODS steels are discussed in this chapter by means of the *in-situ* synchrotron tensile technique. Hence, the responses of each precipitate and matrix phase within the austenitic ODS steels to the externally applied stress can be clarified.

6.1 Room Temperature Tensile Investigations on ODS 304 Steel

6.1.1 Load-Partitioning Phenomenon

The strain-stress diagram of the ODS 304 specimen was measured during *in-situ* synchrotron tensile tests, and is shown in Fig. 6.1. The strain rate was 2×10^{-3} s^{-1}. Each point represents a set of synchrotron measurements. The yield strength (YS) and the ultimate tensile strength (UTS) are 852 MPa and 946 MPa, respectively. Both values are far higher than those of non-ODS austenitic steels[127, 128] as shown in Fig. 6.2. The elongation of ODS 304 steel is around 42%, showing that this steels maintains excellent ductility but with a significant improvement in mechanical strength.

The d-spacing evolutions of all distinguishable phases were analyzed. Due to the anisotropic moduli, the lattice strains vary among the different diffraction conditions. Some specific diffractions yield lattice strains similar to the

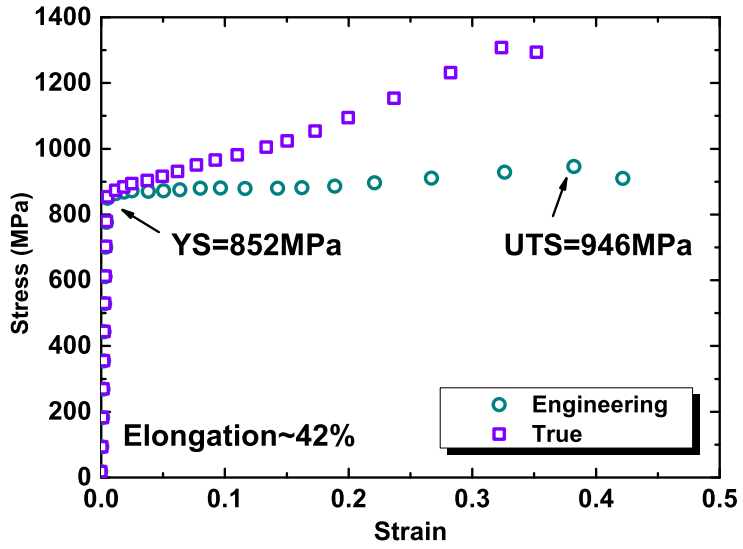

Figure 6.1: Strain-stress diagram of the *in-situ* synchrotron tensile test: the yield strength and ultimate tensile strength of ODS 304 are significantly enhanced compared to ordinary 304 steel, with little compromise in ductility

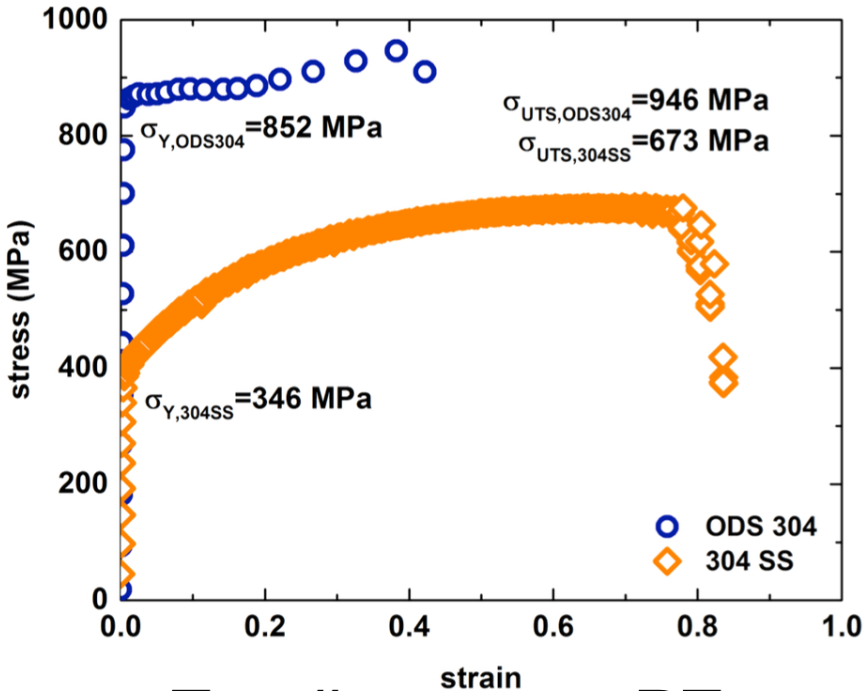

Figure 6.2: Tensile curve comparison between 304 SS and ODS 304.

macroscopic strain. The d-spacing evolution of all distinguishable phases were analyzed. For a specific phase, different reflections can behave diversely with applied stresses, not only due to the anisotropic elastic moduli, but also as a result of the microstructural development (e.g. dislocation structure evolution) during the deformations. Previous studies confirm that the $\{311\}$ reflection is a suitable representation for characterization of macroscopic stresses and strains for face-centered cubic (FCC) metals[129, 20]. From a recent study in a ferritic/martensitic ODS steel, the loading behavior of different reflections show little difference during the entire tensile test[13]. Among all reflections of the martensitic matrix, the elastic constant of $\{321\}$ reflection was found to approach the value of the bulk material[130]. Therefore, the $\{311\}$ reflection of the austenitic matrix and the $\{321\}$ reflection of the martensitic matrix were selected to represent the matrix phases. For the precipitate phases, there exist a limited number of distinguishable diffraction peaks. Thus, $\{111\}$ of TiN and $\{22\bar{1}\}$ of YAM were chosen to represent the lattice strain of precipitates. The behavior of the lattice strain alteration in response to an increasing macroscopic stress is illustrated in Fig. 6.3. It is obvious that all the phases have very similar lattice strains in the elastic deformation regime. However, the lattice strain of YAM experiences a slight rise as the specimen approaches yielding. Once yielded, a prominent load partitioning phenomenon can be observed: the lattice strains of YAM and TiN become much higher than those of the matrices. Comparing macroscopic strain with lattice strains (see Fig. 6.4) provides a different insight into the load partitioning phenomenon: within the elastic regime, lattice strains of all the phases are comparable to the macroscopic strain. As the specimen yields, lattice strains become lower than the macroscopic strain since dislocation gliding, namely, plasticity, begins to account for a significant share of deformation. The Young's moduli of the four distinguishable phases with specific orientations can be derived from the stiffness tensors of these phases: $E_a(311)$=201 GPa[109], $E_m(321)$=279 GPa[131], $E_t(111)$=337 GPa[132], and $E_y(22\bar{1})$=199 GPa[133] ($_t$ for TiN, and $_y$ for YAM). Based on these moduli, the lattice stresses of all the four distinguishable phases were calculated. The lattice stress vs. true strain diagram, as shown in Fig. 6.5, indicates the load partitioning phenomenon more clearly by directly providing the load situation of each phase.

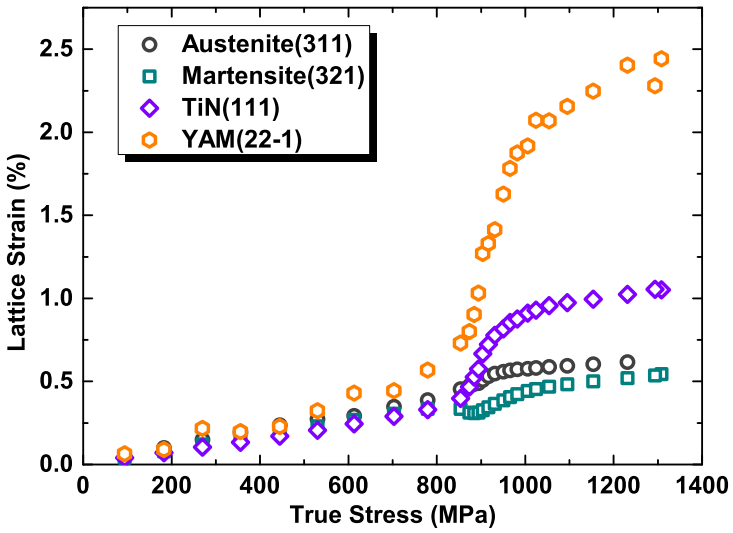

Figure 6.3: Lattice strain vs. true stress for all the distinguishable phases within ODS 304 steel

Since there are two different synchrotron recognizable precipitate phases existing in the ODS 304 steel, it is interesting to compare the behaviors of TiN and YAM. In the STEM images, TiN particles were observed to be much larger and sparser than YAM ones. Also, the YAM phase take more stress after yielding compared with TiN. Here, a very strong size effect on the load partitioning phenomenon is revealed. This size effect is due to the different interaction mechanisms of particles of different sizes with dislocations[134]. This size effect also implies that those Y-Ti-O nanoclusters, which have smaller size and are indistinguishable in synchrotron XRD, are supposed to take even more stress than the YAM particles. In fact, the ultra-fine $Y_2Ti_2O_7$ has been reported to take higher load compared to TiN in a strained 9Cr ferrite ODS steel[13], in which YAM precipitates are absent.

The SEM image of the fracture surface taken from the post-tensile specimen, Fig. 6.6, illustrates the formation of dense distributions of submicron-scale voids that cause the failure. It is worth mentioning that large and medium oxygen-enriched nanoparticles can be identified in some of these voids.

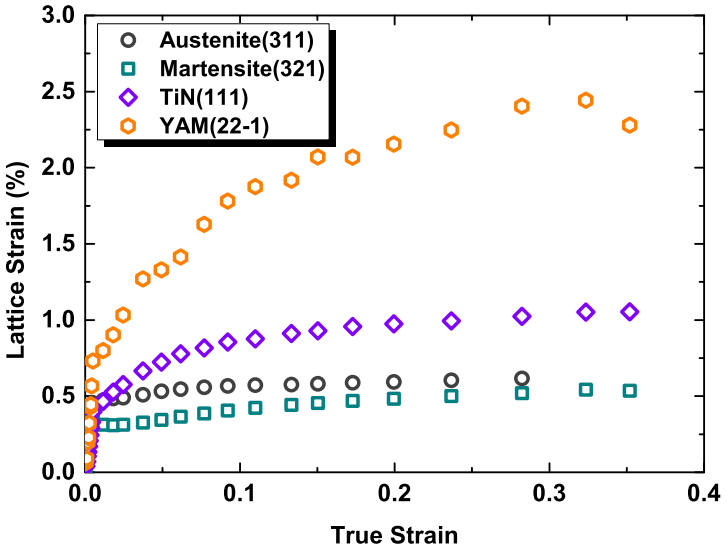

Figure 6.4: Lattice strain vs. true strain for all the distinguishable phases within ODS 304 steel

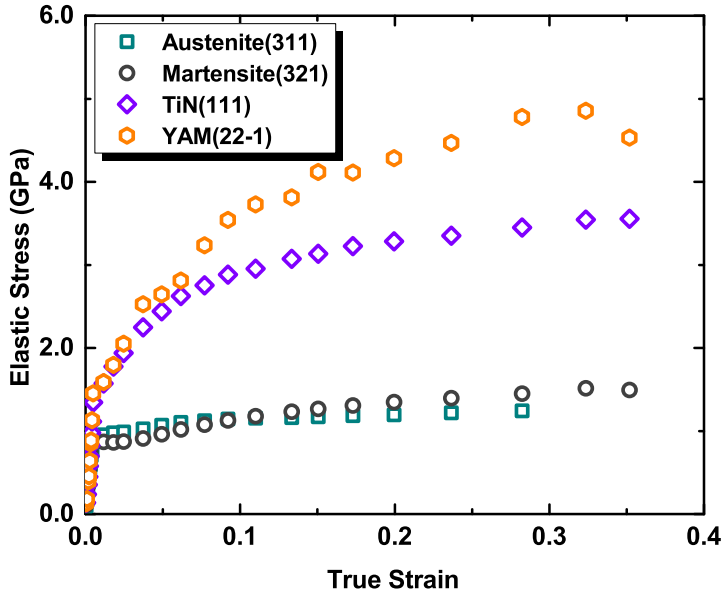

Figure 6.5: Lattice stress vs. true strain for all the distinguishable phases within ODS 304 steel

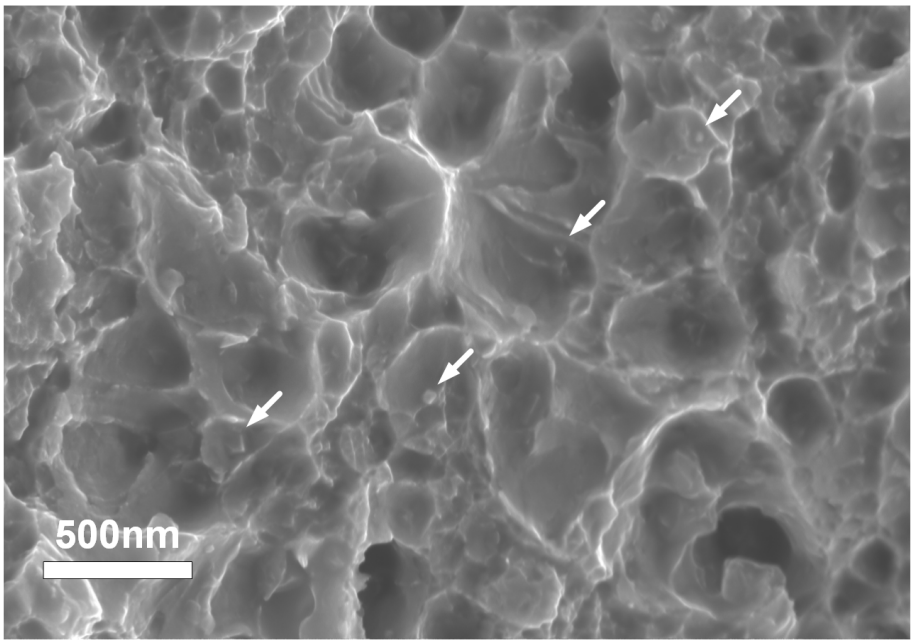

Figure 6.6: SEM image of the fracture surface: some large and medium oxygen-enriched nanoparticles (marked by arrows) are distinguishable on the fracture surface

6.1.2 Deformation-induced Martensitic Transformation

In the presence of oxygen-enriched nanoparticles, the deformation-induced martensitic transformation of the austenitic matrix is prominent. By comparing the TEM bright field images of both pre-tensile and post-tensile specimens, shown in Figs. 6.7 and 6.8, it is obvious that the dominant phase of the pre-tensile specimen is austenite, the majority of which transforms into martensite at failure. These TEM images also indicate that the grain sizes of both initial austenite grains and final martensite grains are around hundreds of nanometers.

The deformation-induced martensitic transformation was monitored by calculating the volume fractions of both austenitic and martensitic phases at each measurement point. The strain-induced martensitic transformation begins during the elastic regime. However, the phase transition is quite marginal before yielding. Once the plastic deformation starts, the transformation becomes significant. In fact, as the specimen begins necking, over 90% of the austenitic matrix has turned into martensite in the specimen strained at 2×10^{-3} s^{-1}(see Fig. 6.9). All the martensite observed in this study is

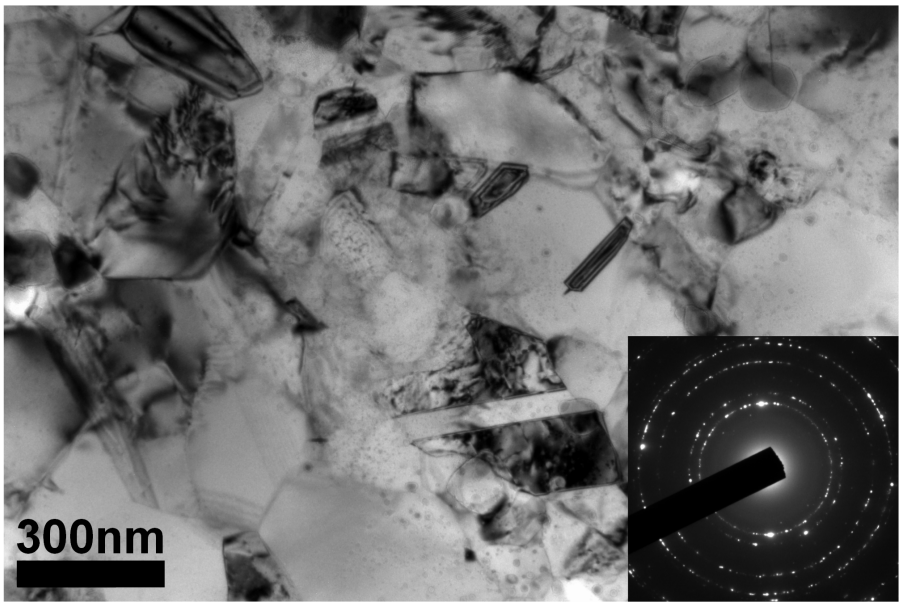

Figure 6.7: TEM bright field image of the pre-tensile specimen. The average grain size is around several hundred nanometers. Dense dispersive oxide nanoparticles are observable, and the dislocation density is low.

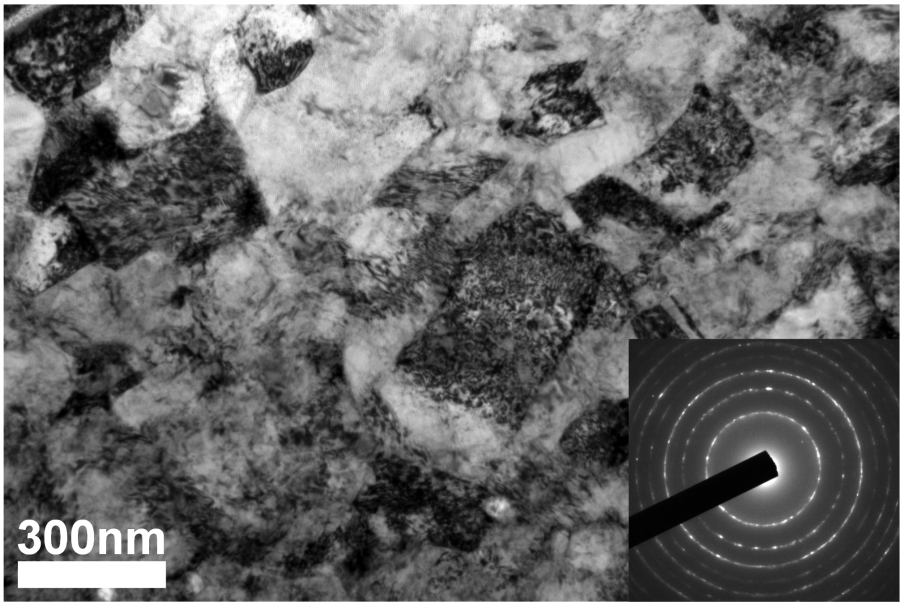

Figure 6.8: TEM bright field image of the post-tensile specimen. The average grain size is around several hundred nanometers, and the dislocation density is high

α'-martensite. No ϵ-martensite was ever distinguished in the synchrotron XRD data, implying that the direct γ-α' phase transformation mechanism is dominant throughout the tensile test.

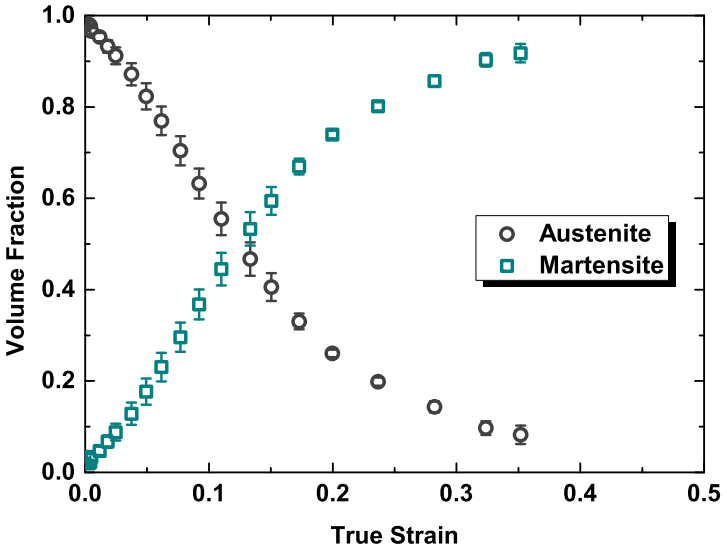

Figure 6.9: Volume fraction evolution of austenitic and martensitic matrices (2×10^{-3} s^{-1}). The initial martensite percentage is around 2% and the final martensite percentage is over 90%

The influence of strain rate was also examined in this study. Aside from the 2×10^{-3} s^{-1} strain rate, which was used for the majority of the analyses, three lower strain rates were also adopted. It is obvious that faster strain rate enhances the deformation-induced martensitic deformation, as shown in Fig. 6.10. The origin of this stain rate effect will be discussed later in this chapter.

6.1.3 The Modified William-Hall Analysis

The changes in grain sizes of both austenite and martensite matrices are shown in Fig. 6.11. The grain size measured by a modified W-H method is only meaningful when it is smaller than several hundred nanometers. In addition, this measurement is only accurate within an order of magnitude and for a correct trend of evolution. The initial austenite grain size is around hun-

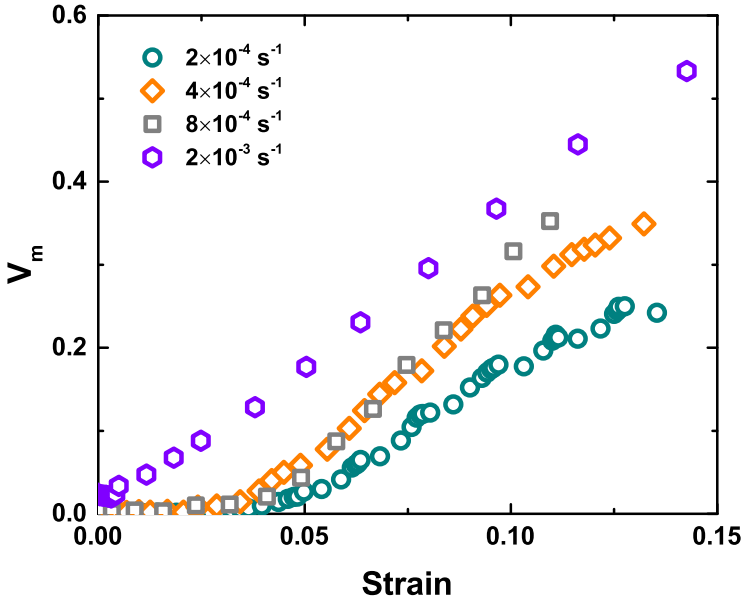

Figure 6.10: Volume fraction evolution of martensite at different strain rates showing a prominent strain rate effect.

dreds of nanometers, which is consistent with the TEM observation, shown in Fig. 6.7. This value begins to decrease even during the elastic regime. This phenomenon is consistent with the fact that the martensitic transformation begins during elastic deformation (as shown in Fig. 6.9). At the end of the tensile tests, the average grain size of austenite is approximately 10 nm, and the grains exist as small residual austenite grains. On the other hand, the initial grain size of martensite is around 20 nm. The martensite grains continue to grow throughout the tensile test. At failure, the martensite grains are as large as several hundreds of nanometers, also consistent with the TEM observation, shown in Fig. 6.8.

The modified W-H method also provided information on the portion of stacking faults and twinning faults in austenite matrix (Fig. 6.12). There existed some stacking and/or twinning faults in the original specimens, but these faults vanish during elastic deformation. As the deformation-induced martensitic transformation is initiated by stacking and twinning faults, this phenomenon may explain the martensitic transformation during the elastic regime. The stacking and twinning faults then decrease to an indistinguish-

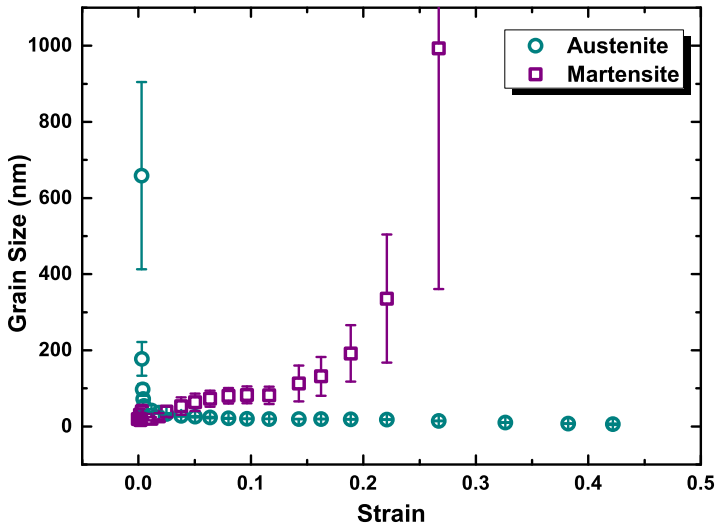

Figure 6.11: Grain size evolution in matrix phases

able level in the early stages of plastic deformation. Meanwhile, the martensitic transformation continues, indicating that the newly formed stacking and twinning faults can rapidly turn into α'-martensite. In the late stages of plastic deformation, the portion of stacking and twinning faults finally rises and then decreases again as the austenite phase is depleted, which is consistent with Shen et al.'s findings in non-ODS 304 steel[135].

Lastly, the evolution of dislocation densities is illustrated in Fig. 6.13. In austenite, the dislocation density has a peak value of 1.4×10^{15} m^{-2}, and then decreases to a marginal value as the austenite phase becomes a minor matrix phase. On the other hand, the dislocation density in martensite continues to increase throughout the entire plastic deformation regime. The maximum dislocation density, 3.0×10^{15} m^{-2}, is comparable to the measurement of the TEM image, 1.6×10^{15} m^{-2}, validating the selection of the fitting parameters. The dislocation density in martensite displays a trough-like behavior in the early stages of plastic deformation. This trough also corresponds to the fastest martensitic transformation rate shown in Fig. 6.9. A fast martensitic transformation creates a great number of martensitic grains with few dislocations, which significantly decreases the average dislocation density significantly. It is noticeable that the prominent increase of stacking and twinning

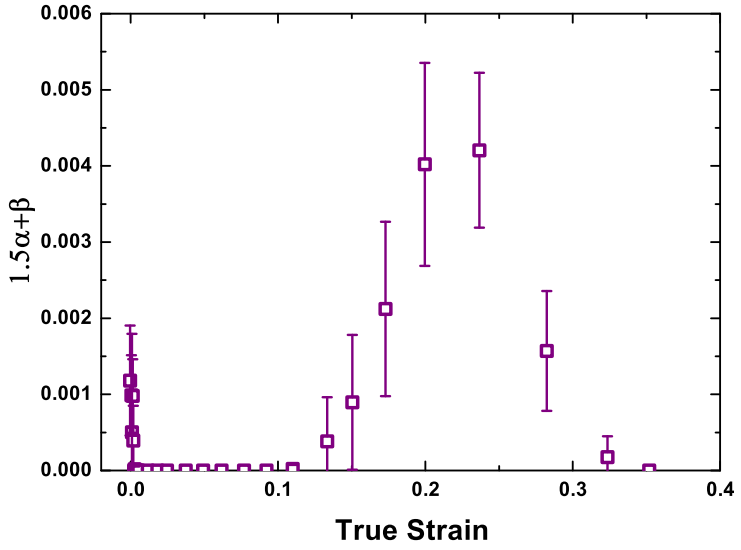

Figure 6.12: Stacking fault and twinning fault evolution in matrix phases

faults only happens while the dislocation density in austenite is beyond a value of 7.6×10^{14} m^{-2}, showing an almost proportional relation between the dislocation behaviors and stacking/twinning fault formation.

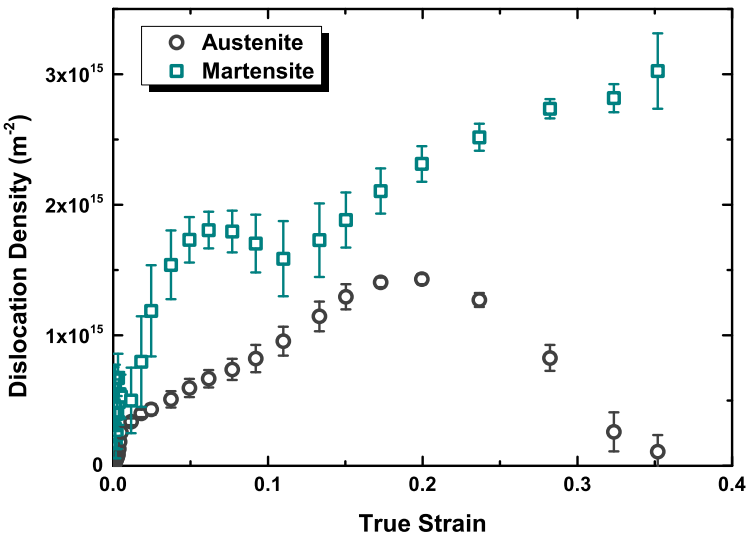

Figure 6.13: Dislocation density evolution in matrix phases

Previous room temperature and sub-0°C temperature tensile tests of or-

dinary 304 steels show the existence of both direct γ-α' and indirect γ-ε-α' mechanisms[89, 135]. However, in this room temperature tensile test of the ODS 304 steel, even the ultra-sensitive synchrotron XRD technique did not detect the formation of any ε-martensite. The absence of one martensitic transformation mechanism implies the effect of the oxygen-enriched nanoparticles. The ε-martensite nucleation always takes place in the regions that contain irregularly spaced stacking faults, whereas the direct nucleation of α'-martensite is usually related to the pile-ups of dislocations[136, 137, 138]. Therefore, in the ordinary 304 steel, the dislocation density is low in the early stages of plastic deformation. Due to the low stacking fault energy (SFE) of 304 steel at room temperature, the sparse dislocations can easily evolve into spaced stacking faults, which is the precursor of ε-martensite nucleation. On the contrary, the accumulation of dislocations leads to the formation of dense dislocation pile-ups in the late stages of plastic deformation, resulting in the dominance of direction nucleation of α'-martensite. This explanation is consistent with Shen et al.'s experimental observations[135]. However, in the presence of dense and dispersive distributions of nano-scale precipitates with excellent mechanical strength, as in ODS steels, the dislocation gliding is significantly suppressed. As a result, dislocation pile-ups are common even in the early stages of plastic deformation. Therefore, the γ-α' mechanism is dominant immediately following yielding. This theory can be further supported by comparing the volume fraction of martensite and dislocation evolution in austenite at different strain rates. Dislocation density in the austenitic matrix is independent on the strain rate as shown in Fig. 6.14, while the martensitic transformation ratio is positively correlated to the strain rate. Therefore, higher strain rate localizes the dislocations without raising the average dislocation density, accelerating the formation of dislocation pileups and the direct γ-α' transformation.

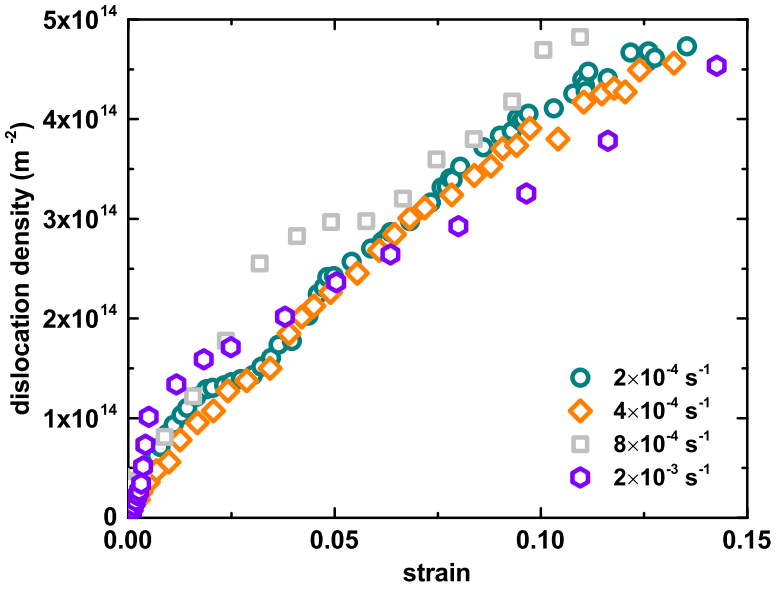

Figure 6.14: Comparison of dislocation density evolution in austenitic matrix at various strain rates

6.2 High Temperature Tensile Investigations on ODS 316 Steel

6.2.1 Load-Partitioning Phenomenon

The *in-situ* tensile investigations were conducted on the ODS 316 miniature tensile specimens at room temperature (RT) and two elevated temperatures. The tensile curves of these three testing conditions are shown in Fig. 6.15. At RT, the yield strength (YS) and ultimate tensile strength (UTS) of the ODS 316 steel are 477 MPa and 729 MPa, respectively. Both values are significantly higher than those of the ordinary 316 steel. The elongation is around 39% at RT. With an increase in temperature, the YS drops to 367 MPa at 350°C and 328 MPa at 550°C. The ductility also worsens at elevated temperatures, but the fracture strain still exceeds 20%. However, even at high temperatures, the ODS 316 steel still maintains adequate tensile strength and ductility.

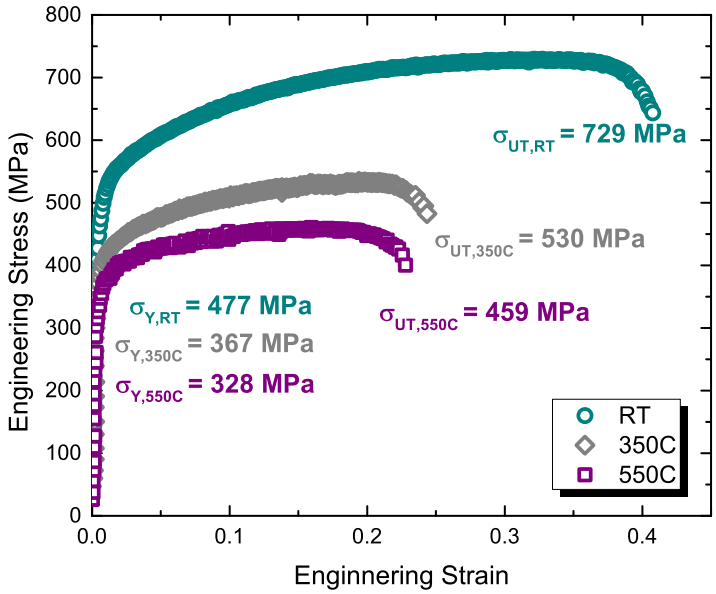

Figure 6.15: Strain-stress curve of the ODS 316 steel at three temperatures

The lattice responses of various precipitate phases and the austenite matrix to the uniaxial tensile stress at RT are illustrated in Fig. 6.16. During elastic deformation, the lattice strains of all three distinguishable and analyzable precipitate phases are close to that of the austenite matrix, showing that the deformation of the precipitates is mainly due to the continuity condition at the interfaces. After the specimen yields, the lattice strain of the austenite matrix becomes much lower than that of the three precipitate phases. This difference in lattice strain implies that the particle-dislocation interactions transfer significant amounts of the stress to the precipitates. Therefore, the nanoparticles sustain higher loads than the austenite matrix. This load partitioning phenomenon, which originates from the particle-dislocation interaction mechanism, accounts for the outstanding tensile strength of the ODS 316 steel.

To better understand the load partitioning mechanism, especially its dependence on the precipitates, it is necessary to determine the actual lattice stress of each precipitates phase and then compare the precipitate stress with the stress of the matrix. Because limited reflections of the precipitates phases are analyzable, only the lattice strains of the precipitates with specific ori-

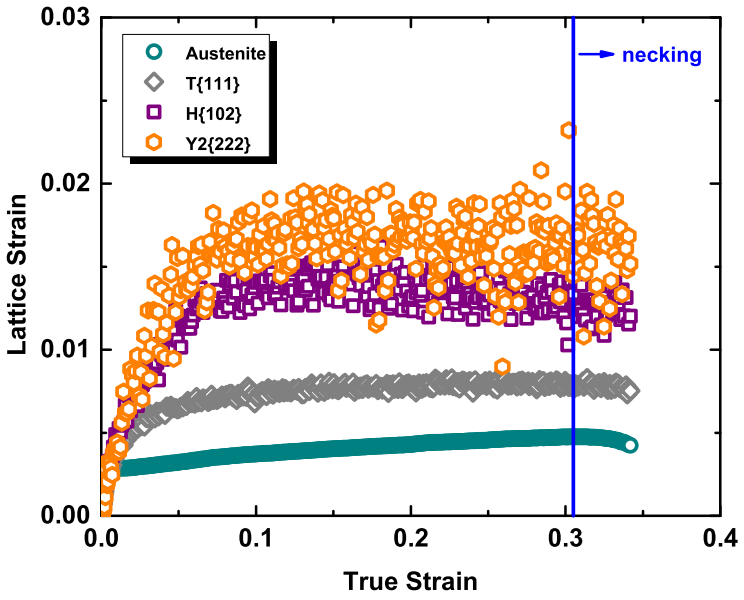

Figure 6.16: Lattice strain evolution of different phases in ODS 316 steel at RT

entations are available. Unfortunately, the three precipitates investigated in this study have anisotropic elasticity. Therefore, only the lattice stresses of these specifically-orientated precipitates were measured and taken to be representative of the phase. At RT, the elastic moduli of the precipitates were derived from the elastic stiffness tensors and were found to be: E_a=193 GPa[92], $E_t(111)$=337 GPa[132], $E_h(102)$=242 GPa, $E_{y_2}(222)$=245 GPa[139] (subscripts $_t$ for TiN, $_h$ for YAH, and $_{y_2}$ for $Y_2Ti_2O_7$). Here, the elastic constant of YAH was calculated using the first principle method due to a lack of existing references. With these Young's moduli, the lattice stresses of different precipitates and the austenite matrix can be calculated. The results are shown in Fig. 6.17.

The lattice stress data provides more useful information on the load partitioning phenomenon in ODS 316 steel than the elastic strain. First, as ceramics generally have higher stiffness than metallic phases, the difference in lattice stress between the austenite matrix and the precipitates is significant. Second, the load partitioning phenomenon has a strong dependence on particle size. The particle phase of the largest size, TiN, has the lowest lattice

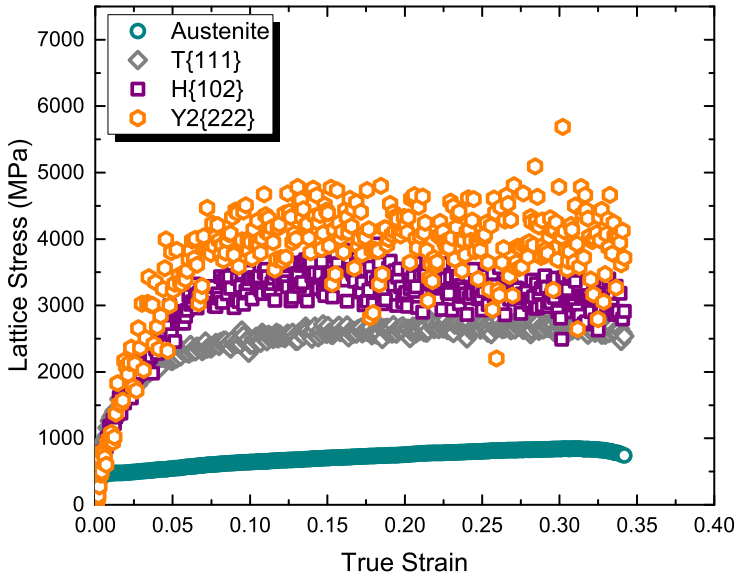

Figure 6.17: Lattice stress evolution of different phases in ODS 316 steel at RT

stress among the three analyzable precipitate phases. On the contrary, the finest precipitates, $Y_2Ti_2O_7$ were found to sustain highest load. In previous observations in ferritic[13] and austenitic[40] ODS steels, where two types of precipitates with different sizes were found, a similar size effect was reported. In this case, three precipitates of different sizes exist, the results undoubtedly indicate that the finer the nanoparticles, the greater their contribution to the strengthening of the material.

At higher temperatures, characteristics of the load partitioning phenomenon change. Figs. 6.18 and 6.19 illustrate the lattice responses of all distinguishable phases to the uniaxial tensile stress at 350°C and 550°C, respectively. As there exist few credible stiffness tensors of the precipitate phases at elevated temperatures, it is more reliable to make comparisons using just lattice strain values rather than lattice stresses. At 350°C, the difference in the lattice strain between TiN and the matrix is already marginal. When the temperature rises to 550°C, the elastic deformation of TiN becomes nearly the same as that of austenite. Despite the fact that TiN still bears higher lattice stress than the matrix due to its larger Young's modulus, the inter-

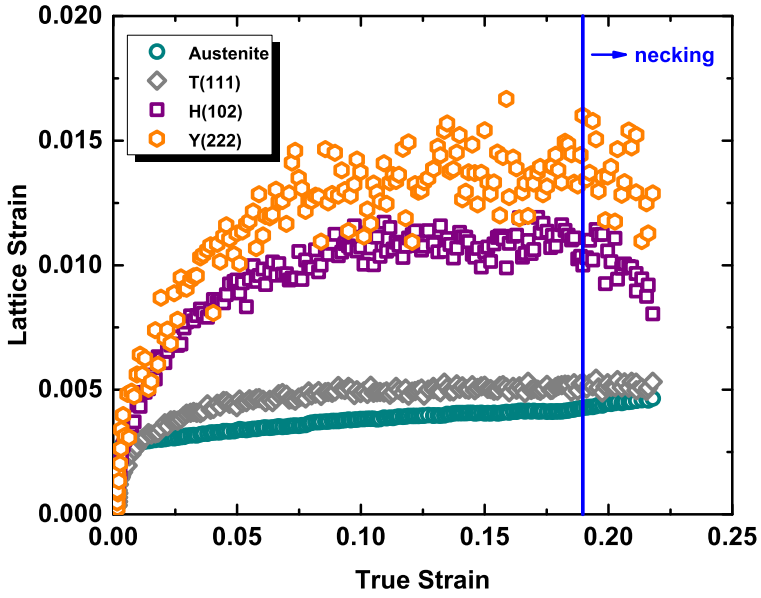

Figure 6.18: Lattice strain evolution of different phases in ODS 316 steel, 350°C

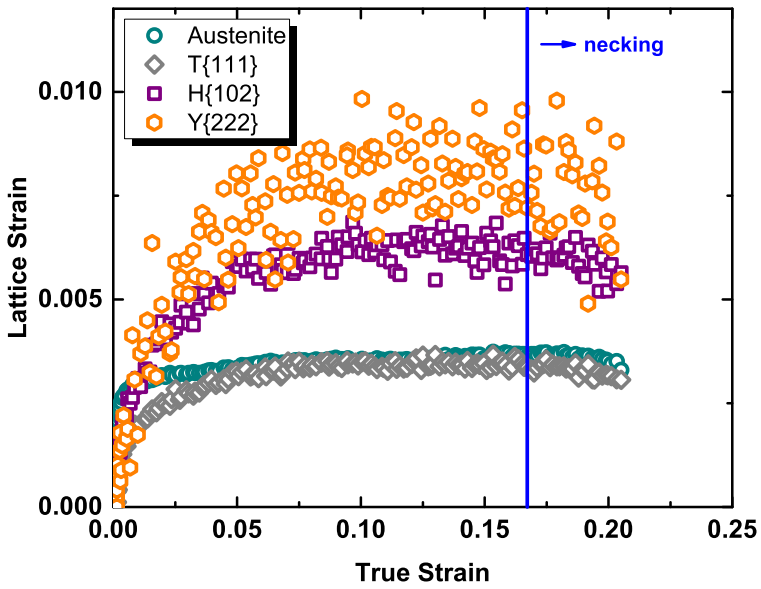

Figure 6.19: Lattice strain evolution of different phases in ODS 316 steel at 550°C

actions between dislocations and TiN particles are suppressed at elevated temperatures. On the other hand, oxide precipitate phases still remain, and have lattice strains much larger than that of the matrix at 550°C. Therefore, the precipitate-strengthening mechanism due to the oxide nanoparticles accounts for, almost the entire enhancement of mechanical strength at elevated temperatures. This phenomenon implies the significance of fine oxide nanoparticles in pinning dislocations at high temperature, validating the rationale of developing ODS steels for high temperature applications, as only the ultra-fine oxide nanoparticles make significant contributions to pinning dislocations at elevated temperatures.

6.2.2 Dislocation Density Evolution

Examination of the lattice responses reveals the temperature and size effects on the load partitioning phenomenon. Further fundamental investigations of these behaviors require information about the dislocation propagation in strained specimens. The modified W-H method is capable of not only assessing the dislocation density, but also distinguishing the edge and screw dislocations (see Fig. 6.20 for fitting examples)). At all three testing temperatures, no stacking fault or twinning portions were observed by the modified W-H analysis. For higher temperature tests, the high value of SFE prevents the extensive formation of stacking faults and twinning faults. At RT, twinning deformations play an important role once the strain rate is high or the irradiation-induced defects preexist[140, 141]. However, when the strain rate is as low as 1×10^{-4} s^{-1}, dislocation glide accounts for the plasticity, even at RT. In this case, the relationship between the dislocation density ρ and the true stress σ_T can be described as follows:

$$\sigma_T = \sigma_0 + \alpha G b \rho^{1/2}, \tag{6.1}$$

where σ_0 is the stress needed for a dislocation to glide in the absence of other dislocations, G is the shear modulus, b is the length of the Burgers vector, α is a fitting constant. For all the three testing temperatures, Equation 6.1 was used to fit the dislocation density vs. true stress profiles shown in Figs. 6.21, 6.22, and 6.23). The good linearity shown in these figures validates

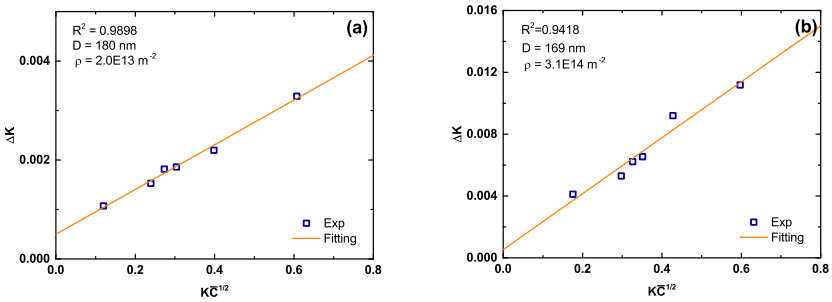

Figure 6.20: Two typical examples of the modified W-H fitting: (a) RT, the pre-strained ODS 316 specimen; (b) RT, the post-strained ODS 316 specimen.

the dominance of dislocation glide in the plastic deformation of ODS 316 specimens tested in this study.

At RT, as shown in Fig. 6.21, edge dislocations dominate the plasticity of the ODS 316 steel. In the pre-strained sample, the intrinsic dislocations, which are predominately geometrically necessary dislocations (GNDs) due to the strain gradient formed during the manufacturing process, are screw-type. Both edge and screw dislocation densities increases in the beginning of plastic deformation. However, the screw dislocation density begins to decrease once the strain reaches about 0.1 and finally drops to nearly zero as the specimen is about to neck. Meanwhile, the edge dislocation density continues to increase until it reaches at its maximum at the necking point.

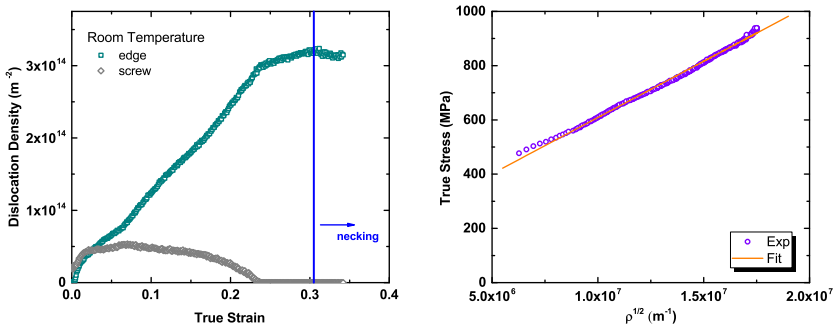

Figure 6.21: Dislocation density evolution in the matrix at RT

The situation changes, however, when the temperature is raised, as illustrated by Fig. 6.22. At 350°C, both screw and edge dislocation densities continue to increase until failure. During this period, the screw dislocation

density is always about twice the magnitude of the edge dislocation density. The faster dislocation density increase during the necking indicates that the synchrotron beam was hitting the necking area.

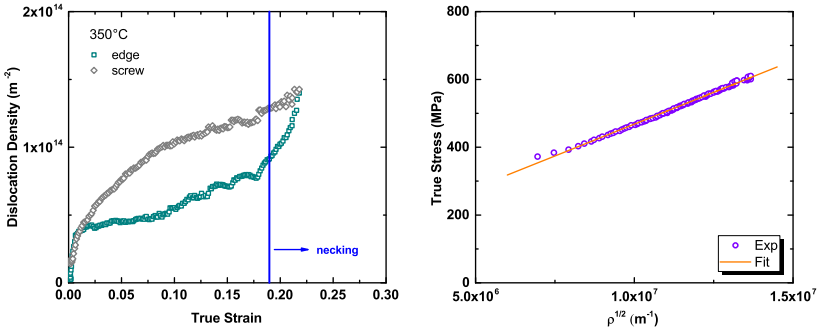

Figure 6.22: Dislocation density evolution in the matrix at 350°C

As shown in Fig. 6.23, when the temperature rises to 550°C, the edge dislocation density reaches its maximum at around 3×10^{13} m^{-2}, and then remains constant, while the screw dislocation density continues to increase until it becomes nearly five times as the edge dislocation density at necking.

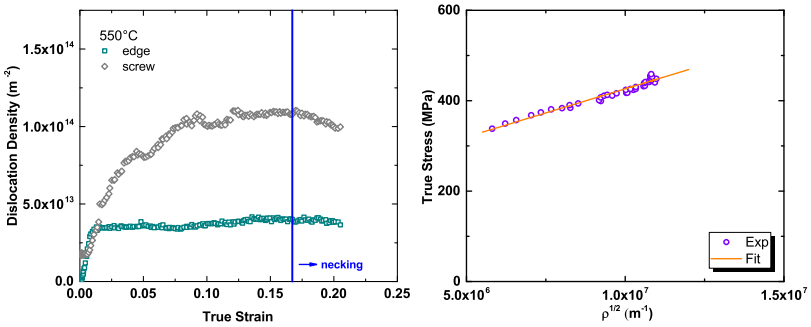

Figure 6.23: Dislocation density evolution in matrix, 550°C

These strong temperature effects are interesting, and may play an important role in the nanoparticle-dislocation interaction, namely, the precipitate-strengthening mechanism. At elevated temperatures, the cross-slip (Q_{CS}) and self diffusion (Q_{SD}) energy barriers both become easier to overcome, resulting in the activation of two parallel mechanisms: the cross-slip of screw dislocations and the climb of edge dislocations. If the difference between Q_{CS} and Q_{SD} is sufficiently large, the mechanism with the lower barrier

will be activated first with increase in temperature. In addition, the SFE increases at high temperatures[111], suppressing the dissociation of dislocations and then enhancing the cross-slip of screw dislocations. The rise of the screw dislocation portion implies the dominance of the cross-slip. Therefore, in this ODS 316 steel, Q_{CS} is much lower than Q_{SD} so that the cross-slip is activated at 550°C, while the climb is still somewhat negligible. This also explains the degradation in the strengthening due to TiN. Because TiN precipitates are large and sparse, screw dislocations can bypass them easily by cross-slip. For finer and denser oxide nanoparticles, simple cross-slip cannot prevent the dislocation from being pinned by other nanoparticles. Instead, the Hirsch mechanism, a particle-dislocation interaction mechanism involving cross-slips, requires a similar magnitude of critical resolved shear stress[60, 64, 65, 66] and therefore does not reduce the strengthening effect. As a result, finer and denser oxide particles strengthen the material up to 550°C.

6.2.3 Electron microscopy investigations of post-strained specimens

TEM was used to examine the foils lifted out from the tensile specimens after failure using FIB. The regions of interest were selected in gauge areas but away from the necking regions. Therefore, these specimens represents conditions near the onset of necking, namely, around the UTS. At all tested temperatures, multiple subgrains formed inside the original grains. More importantly, the dislocation densities were measured according to the bright field TEM images, as shown in Fig. 6.24. The values are consistent with those obtained from the modified W-H method, validating the reliability of both methods.

The fracture surface of the strained specimens were examined by SEM. For all temperatures, nanoparticles within dimples were the major features on the fracture surfaces, as shown in Fig. 6.25. Cracks were initiated by the voids formed on the nanoparticle interfaces. As temperature increases, the cleavage portion of that fracture surface increases, explaining the decrease in elongation. The features on the fracture surface of the 550°C-strained specimen

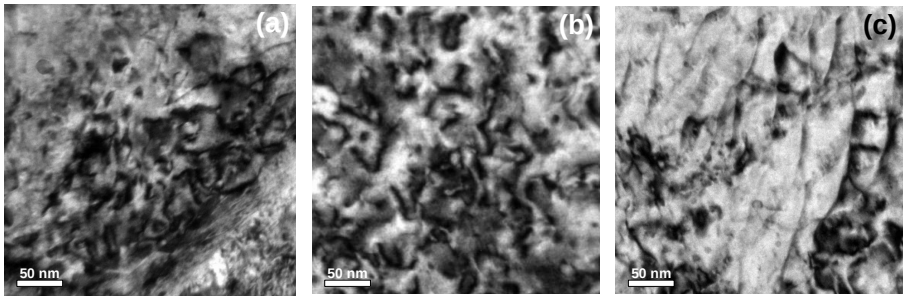

Figure 6.24: TEM bight field images of the gauge areas of the post strained specimens showing different dislocation densities: (a)RT, 3.8×10^{14} m^{-2}; (b) 350°C, 2.2×10^{14} m^{-2}; and (c) 550°C, 1.7×10^{14} m^{-2}. These TEM measured dislocation densities are comparable with those estimated by the modified W-H analyses: 3.15×10^{14} m^{-2} (RT), 1.98×10^{14} m^{-2} (350°C), and 1.49×10^{14} m^{-2} (550°C).

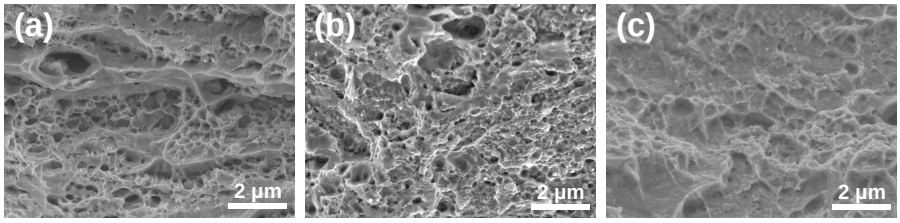

Figure 6.25: SEM images of fracture surfaces of the specimens strained at different temperatures: (a) RT; (b) 350°C; and (c) 550°C.

look blurry, which is mainly due to oxidation at high temperatures.

CHAPTER 7

CONCLUSIONS

In this dissertation, a comprehensive and systematic combination of advanced characterization techniques were performed upon a series of austenitic ODS stainless steels in order to reveal the properties of embedded oxide nanoparticles as well as their interactions with dislocations that propagate during plastic deformation. In addition, state-of-the-art high-energy synchrotron X-ray experiments were conducted to examine the responses of multiple phases embedded within the steel matrices so that the strengthening mechanism of the austenitic ODS can be clarified.

7.1 Characteristics of Oxide Nanoparticles

The elemental compositions as well as the crystal structures of the oxygen-enriched nanoparticles in different austenitic ODS stainless steels vary significantly, depending on the types of powders added during ball-milling and the conditions of thermal processing and heat treatment.

In all the austenitic ODS steels investigated in this study, polyhedral TiC or TiN is the precipitate phase of the largest size (around 100 nm), accounting for the largest particles within the systems.

In the hafnium-containing ODS 316 steel, three groups of oxide nanoparticle phases, including bixbyite structure Y_2O_3, fluorite structure Y_2O_3-HfO_2 solid solution, and pyrochlore (or fluorite) structure $Y_2(Ti,Hf)_{2-x}O_{7-2x}$, were found to coexist. The average particle size is around 10 nm, showing that Ti and Hf do help reduce the size of precipitates. As all those three groups of phases have the similar structures, they contribute to the same peaks in the synchrotron XRD investigation.

In the ODS 304 steel, as a marginal amount of Al exists as impurity, two groups of oxygen-enriched precipitate phases coexist. YAM accounts for the intermediate-sized precipitates, whereas pyrochlore structure $Y_2Ti_{2-x}O_{7-2x}$ composes the finest precipitates. In the ODS 316 steel, which also contains Al impurity, YAP and YAH contribute to the intermediate-sized precipitates while pyrochlore structure $Y_2Ti_2O_7$ and orthorhombic structure Y_2TiO_5 form the finest nanoparticles. In both ODS 304 and 316 steels, smallest nanoparticles, or called nanofeatures, are Y-Ti-O enriched without a well-define stoichiometry. All Y-Ti-O enriched phases also contain marginal but non-negligible Al.

Generally speaking, in the absence of Al, Y-Ti(Hf)-O precipitates account for all the intermediate-sized and small-sized nanoparticles within the austenitic ODS steel systems. When Al exists as impurity, on the other hand, intermediate-sized precipitates are Y-Al-O enriched while the small-sized precipitates are still Y-Ti-O but with a low but non-negligible Al content.

For particles smaller than 10 nm, the nanoparticles are likely to have some specific orientation relationships with the matrices, including two coherent and one axis-parallel (especially cubic-on-cubic) orientation relationships.

7.2 Nanoparticle-dislocation Interactions

In-situ TEM deformation investigations have been performed to study the nanoparticle-dislocation interactions in the hafnium-containing ODS 316 stainless steel. All three major nanoparticle-dislocation interaction mechanisms were observed to exist in the hafnium-containing ODS 316 steel. The following conclusions were drawn:

1. Orowan looping occurs in areas of sparse large nanoparticles or dense intermediate nanoparticles. The source shortening effect coupled with the Orowan mechanism results in the deactivation of dislocations on the original slip planes. New dislocations on parallel slip planes are then activated by the grain boundary source.

2. Shearing was confirmed to exist in ODS steels using indirect obser-

vation methods. shearing occurs in regions with sparse intermediate nanoparticles or small nanoparticles. It also requires alignment between the particle and matrix, which is only found for smaller particle sizes. The CRSS of the nanoparticles continues to decrease as dislocations cut through them. Therefore, the strengthening effect of the shearing mechanism continues to decrease.

3. The Hirsch mechanism was also observed in the ODS 316 steel though there may be an interference of the surface of thin foils in the *in-situ* TEM deformation investigations.

4. The yield strength estimated based on the Orowan strengthening, which appears to be the dominant strengthening mechanism, is consistent with the mechanical measurement, indicating that the Orowan looping is the dominant nanoparticle-dislocation interaction mechanism in the ODS 316 steel.

7.3 Strengthening Mechanism

In-situ Synchrotron X-ray scattering tensile experiments were performed on ODS 304 and ODS 316 steels at room and elevated temperatures, the following conclusions can be drawn:

1. Prominent load partitioning phenomenon was observed in both steels and at all the investigated temperatures. Precipitates bear magnificently more load compared to the matrices do.

2. The particle size effect on the load partitioning phenomenon is significant, and the smaller the particle size, the greater the stress that can be taken. The finest Y-Ti-O nanoparticles sustain the highest load, whereas the coarsest TiN precipitates bear the lowest stress.

3. As the temperature rises, the lattice strain of TiN falls to the same level of the matrix. However, the lattice strains of the oxide phases remain much higher than those of the matrix. The dense and dispersed distribution of oxide precipitates is the key to maintaining excellent mechanical strength at elevated temperatures.

4. The existence of the densely and dispersedly distributed nanoparticles significantly alter the particle-dislocation interaction mechanism during plastic deformation. During deformation-induced martensitic transformation, they accelerate the buildup of dislocation pileups and therefore promote the direct γ-α' mechanism. Consequently, martensitic transformation is a serious issue in metastable austenitic ODS steels such as the ODS 304 steel. Increasing nickel content to further stabilize austenite (ODS 310 and ODS 316, e.g.) may help relieve this problem.

REFERENCES

[1] S. J. Zinkle and G. Was, "Materials challenges in nuclear energy," *Acta Mater.*, vol. 61, no. 3, pp. 735–758, 2013.

[2] "IAEA power reactor information system," 2015. [Online]. Available: www.iaea.org/pris/

[3] "Nuclear energy review," 2014, U.S. Energy Information Administration. [Online]. Available: http://www.eia.gov/totalenergy/data/annual/index.cfm

[4] M. Ashby and M. Smidman, "Materials for nuclear power systems," Granta Design, Tech. Rep., 2010.

[5] F. Goldner, "Development strategy for advanced lwr fuels with enhanced accident tolerance," in *Presentation to Enhanced Accident Tolerant LWR Fuels National Metrics Workshop, October*, vol. 10, no. 20, 2012, p. l.

[6] L. Snead, Y. Katoh, and K. Terrani, "An overview of SiC-based fuel and cladding technologies in support of accident tolerant fuel development," *EHPG13*, 2013.

[7] "Light water reactor sustainability program: Integrated program plan," INL/EXT-11-23452. Office of Nuclear Energy. US Department of Energy, Tech. Rep., 2012.

[8] "A technology roadmap for generation IV nuclear energy systems," Generation IV International, Forum, Tech. Rep., 2002.

[9] "Gif R&D outlook for generation iv nuclear energy systems," Generation IV International, Forum, Tech. Rep., 2009.

[10] T. Maki, "Stainless steel: progress in thermomechanical treatment," *Curr. Opin. Solid. St. M.*, vol. 2, no. 3, pp. 290–295, 1997.

[11] Y. Ma, J.-E. Jin, and Y.-K. Lee, "A repetitive thermomechanical process to produce nano-crystalline in a metastable austenitic steel," *Scr. Mater.*, vol. 52, no. 12, pp. 1311–1315, 2005.

[12] S. Ukai, S. Mizuta, M. Fujiwara, T. Okuda, and T. Kobayashi, "Development of 9Cr-ODS martensitic steel claddings for fuel pins by means of ferrite to austenite phase transformation," *J. Nucl. Sci. Technol.*, vol. 39, no. 7, pp. 778–788, 2002.

[13] K. Mo, Z. Zhou, Y. Miao, D. Yun, H.-M. Tung, G. Zhang, W. Chen, J. Almer, and J. F. Stubbins, "Synchrotron study on load partitioning between ferrite/martensite and nanoparticles of a 9Cr ODS steel," *J. Nucl. Mater.*, vol. 455, no. 1, pp. 376–381, 2014.

[14] G. S. Was and P. L. Andresen, "Irradiation-assisted stress-corrosion cracking in austenitic alloys," *J. Mater.*, vol. 44, no. 4, pp. 8–13, 1992.

[15] E. West and G. Was, "IGSCC of grain boundary engineered 316L and 690 in supercritical water," *J. Nucl. Mater.*, vol. 392, no. 2, pp. 264–271, 2009.

[16] M. Del Giacco, A. Weisenburger, A. Jianu, F. Lang, and G. Mueller, "Influence of composition and microstructure on the corrosion behavior of different Fe–Cr–Al alloys in molten LBE," *J. Nucl. Mater.*, vol. 421, no. 1, pp. 39–46, 2012.

[17] K. Murty and I. Charit, "Structural materials for Gen-IV nuclear reactors: challenges and opportunities," *J. Nucl. Mater.*, vol. 383, no. 1, pp. 189–195, 2008.

[18] X. Pan, X. Wu, K. Mo, X. Chen, J. Almer, J. Ilavsky, D. R. Haeffner, and J. F. Stubbins, "Lattice strain and damage evolution of 9–12% Cr ferritic/martensitic steel during *in situ* tensile test by X-ray diffraction and small angle scattering," *J. Nucl. Mater.*, vol. 407, no. 1, pp. 10–15, 2010.

[19] X. Pan, X. Wu, X. Chen, K. Mo, J. Almer, D. R. Haeffner, and J. F. Stubbins, "Temperature and particle size effects on flow localization of 9–12% Cr ferritic/martensitic steel by *in situ* X-ray diffraction and small angle scattering," *J. Nucl. Mater.*, vol. 398, no. 1, pp. 220–226, 2010.

[20] K. Mo, H.-M. Tung, J. Almer, M. Li, X. Chen, W. Chen, J. B. Hansen, and J. F. Stubbins, "Synchrotron radiation study on Alloy 617 and Alloy 230 for VHTR application," *J. Press. Vess. Technol.*, vol. 135, no. 2, p. 021502, 2013.

[21] A. Popovich, "Preparation of nitride-dispersion-strengthened iron by mechanical alloying," *J. Alloys Compd.*, vol. 215, pp. 169–173, 1994.

[22] Y. Etoh and S. Shimada, "Neutron irradiation effects on intermetallic precipitates in zircaloy as a function of fluence," *J. Nucl. Mater.*, vol. 200, no. 1, pp. 59–69, 1993.

[23] M. S. El-Genk and J.-M. Tournier, "A review of refractory metal alloys and mechanically alloyed-oxide dispersion strengthened steels for space nuclear power systems," *J. Nucl. Mater.*, vol. 340, no. 1, pp. 93–112, 2005.

[24] M. Miller, D. Hoelzer, E. Kenik, and K. Russell, "Stability of ferritic MA/ODS alloys at high temperatures," *Intermetallics*, vol. 13, no. 3, pp. 387–392, 2005.

[25] G. Odette, M. Alinger, and B. Wirth, "Recent developments in irradiation-resistant steels," *Annu. Rev. Mater. Res.*, vol. 38, pp. 471–503, 2008.

[26] M. Wang, Z. Zhou, H. Sun, H. Hu, and S. Li, "Microstructural observation and tensile properties of ODS-304 austenitic steel," *Mater. Sci. Eng. A*, vol. 559, pp. 287–292, 2013.

[27] K. Yutani, H. Kishimoto, R. Kasada, and A. Kimura, "Evaluation of helium effects on swelling behavior of oxide dispersion strengthened ferritic steels under ion irradiation," *J. Nucl. Mater.*, vol. 367, pp. 423–427, 2007.

[28] J. Chen, P. Jung, W. Hoffelner, and H. Ullmaier, "Dislocation loops and bubbles in oxide dispersion strengthened ferritic steel after helium implantation under stress," *Acta Mater.*, vol. 56, no. 2, pp. 250–258, 2008.

[29] Q. Li, C. Parish, K. Powers, and M. Miller, "Helium solubility and bubble formation in a nanostructured ferritic alloy," *J. Nucl. Mater.*, vol. 445, no. 1, pp. 165–174, 2014.

[30] P. Edmondson, C. Parish, Q. Li, and M. Miller, "Thermal stability of nanoscale helium bubbles in a 14YWT nanostructured ferritic alloy," *J. Nucl. Mater.*, vol. 445, no. 1, pp. 84–90, 2014.

[31] S. Ukai and M. Fujiwara, "Perspective of ODS alloys application in nuclear environments," *J. Nucl. Mater.*, vol. 307 - 311, Part 1, no. 0, pp. 749 – 757, 2002.

[32] G. M. Ault and H. Burte, "Technical applications for oxide-dispersion strengthened materials," NASA Lewis Research Center, Tech. Rep., 1966.

[33] S. Ukai, M. Harada, H. Okada, M. Inoue, S. Nomura, S. Shikakura, K. Asabe, T. Nishida, and M. Fujiwara, "Alloying design of oxide dispersion strengthened ferritic steel for long life FBRs core materials," *J. Nucl. Mater.*, vol. 204, pp. 65–73, 1993.

[34] M. Bachhav, G. Robert Odette, and E. A. Marquis, "α' precipitation in neutron-irradiated Fe–Cr alloys," *Scr. Mater.*, vol. 74, pp. 48–51, 2014.

[35] P. Marshall, *Austenitic stainless steels: microstructure and mechanical properties*. Springer, 1984.

[36] F. Garner, M. Toloczko, and B. Sencer, "Comparison of swelling and irradiation creep behavior of fcc-austenitic and bcc-ferritic/martensitic alloys at high neutron exposure," *J. Nucl. Mater.*, vol. 276, no. 1, pp. 123–142, 2000.

[37] H. Oka, Y. Yamazaki, H. Kinoshita, N. Hashimoto, S. Ohnuki, S. Yamashita, and S. Ohtsuka, "Characterization of oxide particles in ODS austenitic stainless steel after heavy ion irradiation up to high doses," in *MRS Proceedings*, vol. 1298. Cambridge Univ Press, 2011, pp. mrsf10–1298.

[38] H. Oka, M. Watanabe, H. Kinoshita, T. Shibayama, N. Hashimoto, S. Ohnuki, S. Yamashita, and S. Ohtsuka, "*In situ* observation of damage structure in ODS austenitic steel during electron irradiation," *J. Nucl. Mater.*, vol. 417, no. 1, pp. 279–282, 2011.

[39] H. Oka, M. Watanabe, N. Hashimoto, S. Ohnuki, S. Yamashita, and S. Ohtsuka, "Morphology of oxide particles in ODS austenitic stainless steel," *J. Nucl. Mater.*, vol. 442, pp. S164–S168, 2013.

[40] Y. Miao, K. Mo, B. Cui, W.-Y. Chen, M. Miller, K. Powers, M. V., G. D., J. Almer, I. Robertson, and J. F. Stubbins, "The interfacial orientation relarelation of oxide nanoparticles in a hafnium-containing oxide dispersion-strengthened austenitic stainless steel," *Mater. Charact.*, vol. 101, pp. 136 – 143, 2015.

[41] Y. Miao, K. Mo, Z. Zhou, X. Liu, K.-C. Lan, G. Zhang, M. K. Miller, K. A. Powers, Z.-G. Mei, J.-S. Park, J. Almer, and J. F. Stubbins, "On the microstructure and strengthening mechanism in oxide dispersion-strengthened 316 steel: A coordinated electron microscopy, atom probe tomography and in situ synchrotron tensile investigation," *Mater. Sci. Eng. A*, vol. 639, no. 0, pp. 585 – 596, 2015.

[42] L. L. Hsiung, M. J. Fluss, S. J. Tumey, B. W. Choi, Y. Serruys, F. Willaime, and A. Kimura, "Formation mechanism and the role of nanoparticles in Fe-Cr ODS steels developed for radiation tolerance," *Phys. Rev. B*, vol. 82, no. 18, p. 184103, 2010.

[43] M. Brocq, B. Radiguet, S. Poissonnet, F. Cuvilly, P. Pareige, and F. Legendre, "Nanoscale characterization and formation mechanism of nanoclusters in an ODS steel elaborated by reactive-inspired ball-

milling and annealing," *J. Nucl. Mater.*, vol. 409, no. 2, pp. 80–85, 2011.

[44] M. Alinger, G. Odette, and D. Hoelzer, "On the role of alloy composition and processing parameters in nanocluster formation and dispersion strengthening in nanostuctured ferritic alloys," *Acta Mater.*, vol. 57, no. 2, pp. 392–406, 2009.

[45] S. Yamashita, S. Ohtsuka, N. Akasaka, S. Ukai, and S. Ohnuki, "Formation of nanoscale complex oxide particles in mechanically alloyed ferritic steel," *Philos. Mag. Lett.*, vol. 84, no. 8, pp. 525–529, 2004.

[46] G. Zhang, K. Mo, Y. Miao, X. Liu, J. Almer, Z. Zhou, and J. F. Stubbins, "Load partitioning between ferrite/martensite and dispersed nanoparticles of a 9cr ferritic/martensitic (f/m) {ODS} steel at high temperatures," *Mater. Sci. Eng. A*, vol. 637, no. 0, pp. 75 – 81, 2015.

[47] Y. Miao, K. Mo, Z. Zhou, X. Liu, K.-C. Lan, G. Zhang, M. K. Miller, K. A. Powers, J. Almer, and J. F. Stubbins, "In situ synchrotron tensile investigations on the phase responses within an oxide dispersion-strengthened (ODS) 304 steel," *Mater. Sci. Eng. A*, vol. 625, no. 0, pp. 146 – 152, 2015.

[48] Y. Uchidi, S. Ohnuki, N. Hashimoto, T. Suda, T. Nagai, T. Shibayama, K. Hamada, N. Akasaka, S. Yamashita, S. Ohstuka et al., "Effect of minor alloying element on dispersing nano-particles in ODS steel," in *MRS Proceedings*, vol. 981. Cambridge Univ Press, 2006, pp. 0981–JJ07.

[49] M. Miller, K. Russell, and D. Hoelzer, "Characterization of precipitates in MA/ODS ferritic alloys," *J. Nucl. Mater.*, vol. 351, no. 1, pp. 261–268, 2006.

[50] H. Zhao, C. L. Fu, M. Krcmar, and M. K. Miller, "Effect of strain on the stabilization of oxygen-enriched nanoclusters in Fe-based alloys," *Phys. Rev. B*, vol. 84, no. 14, p. 144115, 2011.

[51] W. Wolfer and M. Ashkin, "Stress- induced diffusion of point defects to spherical sinks," *J. Appl. Phys.*, vol. 46, no. 2, pp. 547–557, 1975.

[52] J. Dundurs and T. Mura, "Interaction between an edge dislocation and a circular inclusion," *J. Mech. Phys. Solid.*, vol. 12, no. 3, pp. 177–189, 1964.

[53] S. Campos, H. J. Kestenbach, and E. Morales, "On strengthening mechanisms in commercial Nb-Ti hot strip steels," *Metall. Mater. Trans. A*, vol. 32, no. 5, pp. 1245–1248, 2001.

[54] D. A. Porter and K. E. Easterling, *Phase transformations in metals and alloys*. CRC PressI Llc, 1992.

[55] E. Orowan, *Symposium on Internal Stresses in Metals and Alloys.* London: the Institute of Metals, 1948.

[56] D. J. Bacon, U. F. Kocks, and R. O. Scattergood, "The effect of dislocation self-interaction on the Orowan stress," *Philos. Mag.*, vol. 28, pp. 1241–1263, 1973.

[57] L. Proville and B. Bakó, "Dislocation depinning from ordered nanophases in a model fcc crystal: From cutting mechanism to Orowan looping," *Acta Mater.*, vol. 58, pp. 5565–5571, 2010.

[58] Y. Xiang, D. J. Srolovitz, L.-T. Cheng, and E. Weinan, "Level set simulations of dislocation-particle bypass mechanisms," *Acta Mater.*, vol. 52, no. 7, pp. 1745–1760, 2004.

[59] P. Hirsch, "The interpretation of the slip pattern in terms of dislocation movements," *J. Inst. Met.*, vol. 86, 1957.

[60] M. Ashby, *On the Orowan Stess.* MIT Press, 1969.

[61] P. Hirsch and F. Humphreys, "The deformation of single crystals of copper and copper-zinc alloys containing alumina particles. I. macroscopic properties and workhardening theory," *P. Roy. Soc. Lond. A Mat.*, vol. 318, no. 1532, pp. 45–72, 1970.

[62] A. Foreman and M. Makin, "Dislocation movement through random arrays of obstacles," *Can. J. Phys.*, vol. 45, no. 2, pp. 511–517, 1967.

[63] L. Brown and G. Woolhouse, "The loss of coherency of precipitates and the generation of dislocations," *Philos. Mag.*, vol. 21, no. 170, pp. 329–345, 1970.

[64] F. Humphreys and P. Hirsch, "The deformation of single crystals of copper and copper-zinc alloys containing alumina particles. II. microstructure and dislocation-particle interactions," *P. Roy. Soc. Lond. A Mat.*, pp. 73–92, 1970.

[65] F. Humphreys and A. Stewart, "Dislocation generation at SiO_2 particles in an α-brass matrix on plastic deformation," *Surf. Sci.*, vol. 31, pp. 389–421, 1972.

[66] F. Humphreys, *Dislocation-particle interactions, dislocations and properties of real materials.* Inst. Metals, London,, 1984.

[67] Y. Xiang and D. Srolovitz, "Dislocation climb effects on particle bypass mechanisms," *Philos. Mag.*, vol. 86, no. 25-26, pp. 3937–3957, 2006.

[68] V. C. Nardone and J. K. Tien, "Pinning of dislocations on the departure side of strengthening dispersoids," *Scr. Metall.*, vol. 17, no. 4, pp. 467–470, 1983.

[69] D. Srolovitz, R. Petkovic-Luton, and M. Luton, "Straight dislocation-sphericle inclusion interactions: high and low temperature solutions," *Scr. Metall.*, vol. 18, no. 10, pp. 1063–1068, 1984.

[70] B. Clark, I. Robertson, L. Dougherty, D. Ahn, and P. Sofronis, "High-temperature dislocation-precipitate interactions in Al alloys: an *in situ* transmission electron microscopy deformation study," *J. Mater. Res.*, vol. 20, no. 07, pp. 1792–1801, 2005.

[71] R. Behr, J. Mayer, and E. Arzt, "TEM investigations of the superdislocations and their interaction with particles in dispersion strengthened intermetallics," *Intermetallics*, vol. 7, no. 3, pp. 423–436, 1999.

[72] S. Deshmukh, R. Mishra, and I. Robertson, "Investigation of creep threshold stresses using *in situ* TEM straining experiment in an Al–$5Y_2O_3$–10SiC composite," *Mater. Sci. Eng. A*, vol. 527, no. 9, pp. 2390–2397, 2010.

[73] D. Häussler, M. Bartsch, U. Messerschmidt, and B. Reppich, "Hvtem *in situ* observations of dislocation motion in the oxide dispersion strengthened superalloy MA 754," *Acta Mater.*, vol. 49, no. 18, pp. 3647–3657, 2001.

[74] D. Häussler, B. Reppich, M. Bartsch, and U. Messerschmidt, "Interaction processes between dislocations and particles in the ODS nickel-base superalloy INCONEL MA 754 studied by means of *in situ* straining in an HVEM," *Mater. Sci. Eng. A*, vol. 309, pp. 500–504, 2001.

[75] M. Li, L. Wang, and J. D. Almer, "Dislocation evolution during tensile deformation in ferritic/martensitic steels revealed by high-energy X-rays," *Acta Mater.*, vol. 76, no. 0, pp. 381 – 393, 2014.

[76] L. Wang, M. Li, and J. Almer, "Investigation of deformation and microstructural evolution in Grade 91 ferritic–martensitic steel by in situ high-energy X-rays," *Acta Mater.*, vol. 62, pp. 239–249, 2014.

[77] M. Wang, Z. Zhou, Z. Yan, P. Yu, and H. Sun, "TEM characterization of dispersoids and microstructure of ODS -316 austenitic steel," *Acta. Metall. Sinica.*, vol. 49, no. 2, pp. 153–158, 2013.

[78] G. Mahon, J. Howe, and S. Mahajan, "Hrtem study of the {252} γ austenite–martensite interface in an fe8cr–1c alloy," *Philos. Mag. Lett.*, vol. 59, no. 6, pp. 273–279, 1989.

[79] D. A. Muller, "Structure and bonding at the atomic scale by scanning transmission electron microscopy," *Nat. Mater.*, vol. 8, no. 4, pp. 263–270, 2009.

[80] T. F. Kelly and M. K. Miller, "Atom probe tomography," *Rev. Sci. Instrum.*, vol. 78, no. 3, p. 031101, 2007.

[81] M. K. Miller and R. Forbes, "Atom probe tomography," *Mater. Charact.*, vol. 60, no. 6, pp. 461–469, 2009.

[82] L. Yao, M. Moody, J. Cairney, D. Haley, A. Ceguerra, C. Zhu, and S. Ringer, "Crystallographic structural analysis in atom probe microscopy via 3D Hough transformation," *Ultramicroscopy*, vol. 111, no. 6, pp. 458–463, 2011.

[83] M. Miller, C. Parish, and H. Bei, "Controlling diffusion for a self-healing radiation tolerant nanostructured ferritic alloy," *J. Nucl. Mater.*, 2014.

[84] M. K. Miller, *Atom probe tomography: analysis at the atomic level*. Springer, New York, NY, 2000.

[85] M. K. Miller, K. F. Russell, K. Thompson, R. Alvis, and D. J. Larson, "Review of atom probe FIB-based specimen preparation methods," *Microsc. Microanal.*, vol. 13, no. 06, pp. 428–436, 2007.

[86] O. C. Hellman, J. A. Vandenbroucke, J. Rüsing, D. Isheim, and D. N. Seidman, "Analysis of three-dimensional atom-probe data by the proximity histogram," *Microsc. Microanal.*, vol. 6, no. 05, pp. 437–444, 2000.

[87] M. R. Daymond, "The determination of a continuum mechanics equivalent elastic strain from the analysis of multiple diffraction peaks," *J. Appl. Phys.*, vol. 96, no. 8, pp. 4263–4272, 2004.

[88] V. Valvoda and M. Järvinen, "On the Harris texture index," *Powder Diffr.*, vol. 5, no. 04, pp. 200–203, 1990.

[89] A. K. De, D. C. Murdock, M. C. Mataya, J. G. Speer, and D. K. Matlock, "Quantitative measurement of deformation-induced martensite in 304 stainless steel by X-ray diffraction," *Scr. Mater.*, vol. 50, no. 12, pp. 1445–1449, 2004.

[90] T. Ungár, "Strain broadening caused by dislocations," in *Materials Science Forum*, vol. 278. Trans Tech Publ, 1998, pp. 151–157.

[91] T. Ungár, I. Dragomir, Á. Révész, and A. Borbély, "The contrast factors of dislocations in cubic crystals: the dislocation model of strain anisotropy in practice," *J. Appl. Crystallogr.*, vol. 32, no. 5, pp. 992–1002, 1999.

[92] M. Daymond and P. Bouchard, "Elastoplastic deformation of 316 stainless steel under tensile loading at elevated temperatures," *Metall. Mater. Trans. A*, vol. 37, no. 6, pp. 1863–1873, 2006.

[93] J. Ilavsky and P. R. Jemian, "Irena: tool suite for modeling and analysis of small-angle scattering," *J. Appl. Crystallogr.*, vol. 42, no. 2, pp. 347–353, 2009.

[94] G. Beaucage, "Approximations leading to a unified exponential/power-law approach to small-angle scattering," *J. Appl. Crystallogr.*, vol. 28, no. 6, pp. 717–728, 1995.

[95] J. Potton, G. Daniell, and B. Rainford, "Particle size distributions from sans data using the maximum entropy method," *J. Appl. Crystallogr.*, vol. 21, no. 6, pp. 663–668, 1988.

[96] P. Jemian, G. Long, F. Lofaj, and S. Wiederhorn, "Anomalous ultra-small-angle X-ray scattering from evolving microstructures during tensile creep," in *MRS Proceedings*, vol. 590. Cambridge Univ Press, 1999, p. 131.

[97] E. Rauwel, C. Dubourdieu, B. Holländer, N. Rochat, F. Ducroquet, M. D. Rossell, G. Van Tendeloo, and B. Pelissier, "Stabilization of the cubic phase of Hfo by Y addition in films grown by metal organic chemical vapor deposition," *Appl. Phys. Lett.*, vol. 89, p. 012902, 2006.

[98] T. A. Lee and A. Navrotsky, "Enthalpy of formation of cubic yttria-stabilized hafnia," *J. Mater. Res.*, vol. 19, no. 6, pp. 1855–1861, 2004.

[99] M. Robinson, N. Marks, M. Qin, S. Middleburgh, G. Thorogood, G. Lumpkin, and D. Carter, "Calculation of threshold displacement energies in $Y_2Ti_2O_7$ and Y_2TiO_5," in *TMS 2014: Annual Meeting*, 2014.

[100] K. R. Whittle, M. G. Blackford, R. D. Aughterson, G. R. Lumpkin, and N. J. Zaluzec, "Ion irradiation of novel yttrium/ytterbium-based pyrochlores: The effect of disorder," *Acta Mater.*, vol. 59, no. 20, pp. 7530–7537, 2011.

[101] R. Shannon, "Revised effective ionic radii and systematic studies of interatomic distances in halides and chalcogenides," *Acta Cryst. Sect. A*, vol. 32, no. 5, pp. 751–767, 1976.

[102] H. Sakasegawa, F. Legendre, L. Boulanger, M. Brocq, L. Chaffron, T. Cozzika, J. Malaplate, J. Henry, and Y. De Carlan, "Stability of non-stoichiometric clusters in the MA957 ODS ferrtic alloy," *J. Nucl. Mater.*, vol. 417, no. 1, pp. 229–232, 2011.

[103] M. Tamura, H. Sakasegawa, K. Shiba, H. Tanigawa, K. Shinozuka, and H. Esaka, "Decomposition of $Y_2Ti_2O_7$ particles in 8 pct Cr oxide-dispersion-strengthened martensitic steel during tempering," *Metall. Mater. Trans. A*, vol. 42, no. 8, pp. 2176–2188, 2011.

[104] P. Dou, A. Kimura, T. Okuda, M. Inoue, S. Ukai, S. Ohnuki, T. Fujisawa, and F. Abe, "Polymorphic and coherency transition of Y–Al complex oxide particles with extrusion temperature in an Al-alloyed high-Cr oxide dispersion strengthened ferritic steel," *Acta Mater.*, vol. 59, no. 3, pp. 992–1002, 2011.

[105] H. Fukumoto, T. Imura, and Y. Osaka, "Heteroepitaxial growth of Y_2O_3 films on silicon," *Appl. Phys. Lett.*, vol. 55, no. 4, pp. 360–361, 1989.

[106] R. R. Manory, T. Mori, I. Shimizu, S. Miyake, and G. Kimmel, "Growth and structure control of HfO_{2-x} films with cubic and tetragonal structures obtained by ion beam assisted deposition," *J. Vac. Sci. Technol. A*, vol. 20, no. 2, pp. 549–554, 2002.

[107] M. K. Miller, C. M. Parish, and Q. Li, "Advanced oxide dispersion strengthened and nanostructured ferritic alloys," *Mater. Sci. Technol.*, vol. 29, no. 10, pp. 1174–1178, 2013.

[108] J. Pruneda and E. Artacho, "First-principles study of structural, elastic, and bonding properties of pyrochlores," *Phys. Rev. B*, vol. 72, no. 8, p. 085107, 2005.

[109] L. Vitos, P. A. Korzhavyi, and B. Johansson, "Stainless steel optimization from quantum mechanical calculations," *Nat. Mater.*, vol. 2, no. 1, pp. 25–28, 2003.

[110] G. Bonny, D. Terentyev, R. Pasianot, S. Poncé, and A. Bakaev, "Interatomic potential to study plasticity in stainless steels: the FeNiCr model alloy," *Model. Simul. Mater. Sc.*, vol. 19, no. 8, p. 085008, 2011.

[111] T. Byun, "On the stress dependence of partial dislocation separation and deformation microstructure in austenitic stainless steels," *Acta Mater.*, vol. 51, no. 11, pp. 3063–3071, 2003.

[112] D. Michel, J. Moteff, and A. Lovell, "Substructure of Type 316 stainless steel deformed in slow tension at temperatures between 21 and 816 C," *Acta Metall.*, vol. 21, no. 9, pp. 1269–1277, 1973.

[113] H. Ledbetter, "Stainless-steel elastic constants at low temperatures," *J. Appl. Phys.*, vol. 52, no. 3, pp. 1587–1589, 1981.

[114] R. Stoller and S. Zinkle, "On the relationship between uniaxial yield strength and resolved shear stress in polycrystalline materials," *J. Nucl. Mater.*, vol. 283, pp. 349–352, 2000.

[115] P. C. Yashar, S. A. Barnett, L. Hultman, and W. D. Sproul, "Deposition and mechanical properties of polycrystalline Y_2O_3/ZrO_2 superlattices," *J. Mater. Res.*, vol. 14, no. 09, pp. 3614–3622, 1999.

[116] A. Takahashi and N. M. Ghoniem, "A computational method for dislocationprecipitate interaction," *J. Mech. Phys. Solid.*, vol. 56, pp. 1534–1553, 2008.

[117] J. W. Christian, "The stress dependence of dislocation velocity, and its relation to the strain rate sensitivity," *Acta Metall.*, vol. 12, no. 1, pp. 99–102, 1964.

[118] J. D. Atkinson, L. M. Brown, and W. M. Stobbs, "The work-hardening of copper-silica: IV. the Bauschinger effect and plastic relaxation," *Philos. Mag.*, vol. 30, pp. 1247–1280, 1974.

[119] Z. Zhang and D. Chen, "Consideration of orowan strengthening effect in particulate-reinforced metal matrix nanocomposites: A model for predicting their yield strength," *Scr. Mater.*, vol. 54, no. 7, pp. 1321 – 1326, 2006.

[120] Z. Zhang and D. Chen, "Contribution of orowan strengthening effect in particulate-reinforced metal matrix nanocomposites," *Mater. Sci. Eng. A*, vol. 483-484, no. 0, pp. 148 – 152, 2008, 14th International Conference on the Strength of Materials.

[121] M. K. Habibi, S. P. Joshi, and M. Gupta, "Hierarchical magnesium nano-composites for enhanced mechanical response," *Acta Mater.*, vol. 58, no. 18, pp. 6104–6114, 2010.

[122] P. Kelly, *Int. Metals. Rev.*, vol. 18, p. 31, 1973.

[123] E. Hall, "The deformation and ageing of mild steel: III discussion of results," *P. Phys. Soc. B*, vol. 64, no. 9, p. 747, 1951.

[124] N. Petch, "The cleavage strength of polycrystals," *J. Iron Steel Inst.*, vol. 174, pp. 25–28, 1953.

[125] B. Han and D. Dunand, "Microstructure and mechanical properties of magnesium containing high volume fractions of yttria dispersoids," *Mater. Sci. Eng. A*, vol. 277, no. 1, pp. 297–304, 2000.

[126] N. Hirota, F. Yin, T. Azuma, and T. Inoue, "Yield stress of duplex stainless steel specimens estimated using a compound Hall–Petch equation," *Sci. Technol. Adv. Mat.*, vol. 11, no. 2, p. 025004, 2010.

[127] P. L. Mangonon and G. Thomas, "Structure and properties of thermal-mechanically treated 304 stainless steel," *Metall. Trans.*, vol. 1, no. 6, pp. 1587–1594, 1970.

[128] P. L. Mangonon and G. Thomas, "The martensite phases in 304 stainless steel," *Metall. Trans.*, vol. 1, no. 6, pp. 1577–1586, 1970.

[129] B. Clausen, T. Lorentzen, and T. Leffers, "Self-consistent modelling of the plastic deformation of fcc polycrystals and its implications for

diffraction measurements of internal stresses," *Acta Mater.*, vol. 46, no. 9, pp. 3087–3098, 1998.

[130] K. Mo, A. Oaks, Y. Miao, and J. F. Stubbins, "Web calculator of bulk elastic response of polycrystalline aggregate," *http://materials.npre.illinois.edu/calculator/website.html*, 2013.

[131] H. Zhang, B. Johansson, and L. Vitos, "*Ab initio* calculations of elastic properties of bcc Fe-Mg and Fe-Cr random alloys," *Phys. Rev. B*, vol. 79, no. 22, p. 224201, 2009.

[132] M. Zhang and J. He, "*Ab-initio* calculation of elastic constants of TiN," *Surf. Coat. Technol.*, vol. 142, pp. 125–131, 2001.

[133] X. Zhan, Z. Li, B. Liu, J. Wang, Y. Zhou, and Z. Hu, "Theoretical prediction of elastic stiffness and minimum lattice thermal conductivity of $Y_3Al_5O_{12}$, $YAlO_3$ and $Y_4Al_2O_9$," *J. Am. Ceram. Soc.*, vol. 95, no. 4, pp. 1429–1434, 2012.

[134] D. Chrzan, J. Morris, Y. N. Osetsky, R. Stoller, and S. Zinkle, "What is the limit of nanoparticle strengthening?" *MRS Bull.*, vol. 34, no. 03, pp. 173–177, 2009.

[135] Y. Shen, X. Li, X. Sun, Y. Wang, and L. Zuo, "Twinning and martensite in a 304 austenitic stainless steel," *Mater. Sci. Eng. A*, vol. 552, pp. 514–522, 2012.

[136] T. Suzuki, H. Kojima, K. Suzuki, T. Hashimoto, and M. Ichihara, "An experimental study of the martensite nucleation and growth in 18/8 stainless steel," *Acta Metall.*, vol. 25, no. 10, pp. 1151–1162, 1977.

[137] J. Brooks, M. Loretto, and R. Smallman, "*In situ* observations of the formation of martensite in stainless steel," *Acta Metall.*, vol. 27, no. 12, pp. 1829–1838, 1979.

[138] J. Brooks, M. Loretto, and R. Smallman, "Direct observations of martensite nuclei in stainless steel," *Acta Metall.*, vol. 27, no. 12, pp. 1839–1847, 1979.

[139] Y. Luan, "Elastic properties of complex transition metal oxides studied by resonant ultrasound spectroscopy," 2011.

[140] X. Wu, X. Pan, J. C. Mabon, M. Li, and J. F. Stubbins, "The role of deformation mechanisms in flow localization of 316l stainless steel," *J. Nucl. Mater.*, vol. 356, no. 1, pp. 70–77, 2006.

[141] E. Lee, M. Yoo, T. Byun, J. Hunn, K. Farrell, and L. Mansur, "On the origin of deformation microstructures in austenitic stainless steel: part II–mechanisms," *Acta Mater.*, vol. 49, no. 16, pp. 3277–3287, 2001.